

Dissertation
submitted to the
Combined Faculties for the Natural Sciences and for Mathematics
of the Ruperto-Carola University of Heidelberg, Germany
for the degree of
Doctor of Natural Sciences

Put forward by
Diplom-Physicist: Kristina Irsch
Born in: Merzig, Germany
Oral examination: December 17, 2008

**Polarization Modulation Using Wave Plates
to Enhance Foveal Fixation Detection in
Retinal Birefringence Scanning for Pediatric
Vision Screening Purposes**

Referees: Prof. Dr. Josef Bille
Prof. Dr. Christoph Cremer

To

My Teachers

For Showing Me the Excitement and Joy of Ophthalmic Optics

My Parents

For Their Love and Abundant Support

Zusammenfassung

Um die beidäugige foveale Fixationserkennung mit Hilfe der binokularen „Retinal Birefringence Scanning“ (RBS)-Methode zu Seh-Screening Zwecken von Kleinkindern zu verbessern, wurde ein neues Verfahren entwickelt, welches auf der Verwendung eines rotierenden $\lambda/2$ -Plättchens und eines festen Wellenplättchens beruht. Das rotierende $\lambda/2$ -Plättchen ermöglicht differenzielle polarisationsempfindliche Detektion des Fixationssignals mit nur einem Detektor und überwindet damit Grenzen des vorherigen optisch-elektronischen Aufbaus mit zwei Photodetektoren. Mit Hilfe der festen Verzögerungsplatte kann dieses durch die doppelbrechende Eigenschaft der Henle-Faserschicht verursachte Fixationssignal quasi unabhängig von der störenden kornealen Doppelbrechung, welche von einem Auge zum anderen variiert, erfasst werden. Unter Zuhilfenahme gemessener Doppelbrechungswerte der Hornhaut von 300 repräsentativen menschlichen Augen wurde unter MATLAB ein Algorithmus und eine damit verbundene Computersoftware zur Optimierung der Eigenschaften beider Wellenplättchen entwickelt. Das Optimierungsverfahren bestand in der Maximierung des Fixationssignals bei gleichzeitiger Minimierung der inter- und intra-individuellen Variabilität aufgrund verschiedener Hornhautwerte. Rotiert man das $\lambda/2$ -Plättchen mit $9/16$ der Scan-Frequenz und verwendet man ein Wellenplättchen mit einer Verzögerung von 45° und einer Orientierung von 90° , so wird das Fixationssignal optimiert. Kombiniert mit der „Bull’s-Eye“-Methode zur Erkennung von Defokus eignet sich dieses computeroptimierte RBS-basierte Verfahren als gerätegestützte objektive Methode zur automatischen Erkennung eines Amblyopierisikos bei Kleinkindern, die Hauptursache des Sehverlustes im Kindesalter.

Abstract

To enhance foveal fixation detection while bypassing the deleterious effects of corneal birefringence in binocular retinal birefringence scanning (RBS) for pediatric vision screening purposes, a new RBS design was developed incorporating a double-pass spinning half wave plate (HWP) combined with a fixed double-pass retarder into the optical system. The spinning HWP enables essential differential polarization detection with only one detector, easing constraints on optical alignment and electronic balancing, and together with a fixed wave plate, this differential RBS signal can be detected essentially independent of various corneal retardances and azimuths. Utilizing the measured corneal birefringence from a dataset of 300 human eyes, an algorithm was developed in MATLAB for optimizing the properties of both wave plates to statistically maximize the RBS signal, while having the greatest independence from left and right eye corneal birefringence. Foveal fixation detection was optimized with the HWP spun $9/16$ as fast as the circular scan, with the fixed retarder having a retardance of 45 degrees and fast axis at 90 degrees. Combined with bull’s-eye focus detection, this computer-optimized RBS design promises to provide an effective screening instrument for automatic identification of infants at risk for amblyopia, the leading cause of vision loss in childhood.

*“Life is like riding a bicycle.
To keep your balance you must keep moving.”*

Albert Einstein

Contents

1 Introduction.....	1
2 Vision Screening.....	4
2.1 Amblyopia	4
2.2 Traditional Screening Methods.....	5
2.3 Newer Screening Modalities.....	8
3 Polarization and the Eye	11
3.1 Polarization of Light	11
3.1.1 Linearly Polarized Light	13
3.1.2 Circularly Polarized Light.....	13
3.1.3 Elliptically Polarized Light	14
3.2 Birefringence	15
3.2.1 Wave Plates.....	17
3.2.2 Form Birefringence	18
3.3 Müller- Stokes Matrix Calculus.....	19
3.3.1 Stokes Vector Representation	19
3.3.2 Müller Matrix Formalism.....	23
3.3.3 Poincaré Sphere.....	23
3.4 Ocular Birefringence.....	25
3.4.1 Lenticular Birefringence	26
3.4.2 Corneal Birefringence	27
3.4.3 Retinal Birefringence	29
4 Retinal Birefringence Scanning (RBS).....	32
4.1 Assessment of Foveal Fixation	32
4.2 Pediatric Vision Screening Using Binocular RBS.....	34
4.2.1 Optical Design of RBS System.....	35
4.2.2 Limitations and Problems	36
4.2.3 Hypotheses and Objectives	39

5 Spinning Half Wave Plate Design for RBS	40
5.1 Phase-Shift Subtraction Technique.....	41
5.2 Modeling of RBS Using Wave Plates.....	43
5.2.1 Model of Ocular Birefringence	43
5.2.2 Assessing the Influence of Corneal Birefringence on the RBS Signal	53
5.2.3 Determination of Optimum Spinning Frequency of Double-Pass HWP	56
5.2.4 Finding the Optimum Fixed Double-Pass Wave Plate	63
5.2.5 Differential Polarization Subtraction with Optimized Spinning-HWP RBS Design	75
6 Validation of RBS Computer Model	78
6.1 Experimental Setup.....	78
6.1.1 Intermediate Eye Fixation Monitor.....	78
6.1.2 Method of Determining the Retardance and Fast Axis Orientation of a Wave Plate.....	82
6.1.3 Method of Determining Corneal Birefringence	84
6.2 Model Predictions with the Intermediate Eye Fixation Monitor	86
6.2.1 Influence of Varying Corneal Birefringence on the RBS Signal.....	86
6.2.2 Optimizing Foveal Fixation Detection with the Intermediate Eye Fixation Monitor	87
6.3 Verification with Human Subjects.....	94
6.3.1 Model Predictions for Studied Eyes.....	94
6.3.2 Measured Data from Studied Eyes.....	97
6.3.3 Comparison of Measured Data and Predicted Results.....	99
7 Pediatric Vision Screener – Mark V: Spinning PVS Design and Operation.....	101
7.1 Optical Design	101
7.1.1 Alignment Detection.....	103
7.1.2 Focus Detection.....	104
7.1.3 Optical Components.....	104
7.2 Mechanical Realization.....	105
7.2.1 Mechanical Components.....	106
7.3 Device Operation – Outlook	109
8 Discussion.....	112
Appendix.....	115
References.....	119
Publications	127
Acknowledgements	129

Chapter 1

Introduction

Amblyopia (“lazy eye”) is the leading cause of vision loss in childhood, caused by ocular misalignment (strabismus) or defocus. If treated early in life, especially during infancy, there is an excellent response to therapy, yet over half of all children with amblyopia under age 5 escape detection. With a prevalence as high as 5%, potentially millions of children suffer from this readily treated cause of vision loss, due to the simple lack of detection.

Early mandatory vision screening by eye care specialists has been shown to reduce the prevalence of amblyopia remarkably, however such mass screening approaches are not cost effective in most health care systems if administration by pediatric ophthalmologists or optometrists is required. Despite ongoing efforts to supply the demand for an automated screening device that can easily be administered by lay personnel, none of the already commercially available instruments has the performance to merit universal application for pediatric vision screening. Autorefractors have demonstrated high sensitivity and specificity in detecting poor focus, but they cannot detect strabismus. Currently available photoscreeners on the market detect strabismus only crudely via apparent displacement of the corneal light reflexes.

Our laboratory within the Division of Pediatric Ophthalmology and Adult Strabismus at the Wilmer Ophthalmological Institute, The Johns Hopkins University School of Medicine, has been developing a “Pediatric Vision Screener” (PVS) that can simultaneously detect proper alignment as well as proper focus of infants’ eyes. The latter is determined by assessing the size of the double-pass blur image produced from a point source of light. Eye alignment is assessed by means of binocular retinal birefringence scanning (RBS), in which polarized near-infrared light is directed onto the retina in an annular scan. The retinal nerve fibers are birefringent, and the polarization-related changes in light retro-reflected from the ocular fundus are analyzed by means of differential polarization detection.

The previous PVS design, finished in our lab in 2002, has shown promise as a reliable screening device for the primary causes of amblyopia. However, relatively low signals and high noise limited its overall performance. Major problems are the opto-electronic complexity of the prototype design, requiring precise alignment and balancing of two photodetectors for differential detection. In addition, the overall RBS signal level varied from one individual to the next, caused by variability and non-uniformity of corneal birefringence across individuals, occasionally masking the desired signal component generated from retinal birefringence.

With the primary objective being to increase the signal-to-noise ratio while bypassing the deleterious effects of corneal birefringence in binocular retinal birefringence scanning for pediatric vision screening purposes, the new design presented in this thesis incorporates a double-pass spinning half wave plate (HWP) in combination with a fixed double-pass retarder. The incorporation of the spinning HWP enables essential differential polarization detection with only one detector, easing constraints on alignment and balancing, and together with a fixed double-pass wave plate, the differential polarization signal can be detected essentially independently of various amounts and orientations of corneal birefringence that occur in the population.

The thesis is structured as follows: Chapter 2 provides a general background on the clinical condition known as amblyopia to establish the basis for understanding the rationale or need for pediatric vision screening. Traditional vision screening methods are then described, followed by newer screening modalities commonly referred to as photoscreeners.

The theoretical foundation of this thesis is laid in Chapter 3 to provide the reader with specific terms that are essential for the understanding of the following chapters. Chapter 3 is divided in two major parts, beginning with general physical theory regarding the polarization of light, followed by specific polarization-related features of the human eye. First, the polarization of light is explored in more detail, explaining the concept of polarization as well as its mathematical formulation, with the presentation of different representations of polarized light. Special attention is given to the description of birefringence, along with the use of the Müller-Stokes calculus, proving to be of major importance for the further course of this work. The portions on ocular birefringence deal primarily with corneal and retinal birefringence.

Chapter 4 explains the method of retinal birefringence scanning (RBS), beginning with a description of how it is used for the assessment of foveal fixation. The advantage of this method over other techniques for estimating the direction of eye fixation is pointed out, and potential applications using RBS-based eye fixation sensing are introduced,

forming the transition to a more detailed description of its major application for the detection of ocular misalignment in pediatric vision screening. The optical design of the binocular RBS system as implemented into the prototype Pediatric Vision Screener is explained, along with its major problems and limitations. Addressing these problems and limitations leads to the hypotheses and objectives of this thesis.

The core chapter of this thesis is Chapter 5, in which the new spinning wave plate design for RBS, incorporating a spinning double-pass half wave plate combined with a fixed double-pass retarder, is derived. The chapter begins with an explanation of the principle of differential polarization detection with the spinning half wave plate and single detector, and demonstrates how the differential polarization signal is calculated by means of 360° -phase-shift subtraction. The RBS computer model used to optimize the properties of both wave plates is explored in detail, starting with a general description of how the human eye, in other words, ocular birefringence, was modeled. The reader will be guided through the optimization process step by step, and the chapter is concluded with the presentation of the predicted outcome with the optimized spinning RBS design.

The RBS computer model was verified with experimental human data using an intermediate monocular RBS-based eye fixation monitor. This model validation is the subject of Chapter 6. The RBS design of the monocular fixation monitor is described in detail, to which the optimization algorithm from the previous chapter was applied to assess the model's performance in finding the optimum design that enhances foveal fixation detection. Model predictions with the monocular eye fixation monitor are compared with actual measurements on human eyes.

In Chapter 7 the optimized spinning-wave-plate RBS design from Chapter 5 is implemented and combined with bull's-eye focus detection, forming the Mark V Pediatric Vision Screener. The opto-mechanical design is detailed, and the principle of binocular foveal fixation and focus detection with the refined PVS is explained. The chapter ends with a prediction regarding the operation of the vision screener, designed for easy administration to infants and young children by lay personnel.

To conclude, in Chapter 8, the presented work is reviewed and discussed. Advantages and limitations are discussed, and future directions are outlined.

Chapter 2

Vision Screening

2.1 Amblyopia

Amblyopia, commonly known as “lazy eye,” is poor vision in an otherwise normal eye. Other than correctable refractive errors, amblyopia is the leading cause of poor vision in childhood, affecting approximately 2-5% of the population [Sjö90]. The etiology of amblyopia is believed to be improper visual input to the brain during the developmentally critical period, resulting in abnormal development of the visual system.

There are two primary causes of amblyopia, referred to as amblyogenic risk factors. By far the most common risk factor is misalignment of the eyes, that is, the clinical abnormality termed strabismus. If the two eyes are misaligned in childhood, the brain may learn to actively suppress the input from one eye to avoid double vision or visual confusion.

The other major amblyogenic risk factor is defocus. When an eye lacks proper focus in childhood, for example when there is unbalanced refractive error between the two eyes, a condition clinically known as anisometropia, the brain may fail to receive proper input from one eye. Other than anisometropia, defocus may also result from isometropic refractive error such as bilateral high hyperopia, ocular media opacities such as cataract, or from drooping of the upper eyelid (ptosis). Both suppression and deprivation interfere with normal visual development and may cause irreversible poor vision extending into adulthood.

Early detection and treatment of amblyopia is the key to promoting proper development of binocular function, thereby preventing permanent loss of vision. If detected at an early stage of childhood development, especially during infancy, there is an excellent response to therapy that is usually done by patching or blurring the good (sound)

eye in order to force the child to use the amblyopic eye. Delayed treatment, on the other hand, can result in lifelong visual impairment.

Unfortunately, amblyopia is difficult to detect in infants and young children. Poor cooperation by infants, and often the inability to communicate, is the major problem, making their examination in general more difficult. Traditional clinical tests can be effective, however untrained professionals, such as health care practitioners who do not specialize in eye care, often fail to detect amblyogenic risk factors in children before age 5 [Köh73]. Due to the simple lack of detection, many children suffering from readily preventable causes of vision loss go undetected and untreated.

The usefulness of early screening has been demonstrated in many studies. Countries that have instituted early vision screening for amblyopia and amblyogenic risk factors have illustrated that such an approach results in better outcomes [Eib00, Will02]. In Scandinavia, for instance, mass screening of young children by eye care specialists has reduced the prevalence of amblyopia remarkably [Kva01]. However, such screening on a wide scale is not economically feasible in most health care systems if administration by a trained professional is required.

This has led to the development of a variety of new automated screening devices, geared towards operation by lay personnel. However, despite ongoing efforts to supply the demand for a reliable and effective technique that can easily be administered by lay personnel, none of the already commercially available automated screeners has sufficient sensitivity, specificity, and low cost to merit universal application for pediatric vision screening.

Traditional vision screening, as well as newer photorefractive and photostereopsis modalities, are described in the following section.

2.2 Traditional Screening Methods

Visual acuity testing, non-cycloplegic retinoscopy, stereoacuity testing, and cover testing are well-established, traditional screening methods that have been recommended by the pediatric ophthalmology community for pre-school vision screening [The04].

The most widely used approach to pre-school vision screening is visual acuity testing, normally performed in the course of measuring the refractive error in a clinical setting. Acuteness of vision is a measure of the angle subtended at the eye by the smallest detail that can be perceived. It is usually determined by means of optotypes, which are

letters or pictures presented on a chart to be read or identified. While the Snellen chart is the gold standard in measuring visual acuity in adults, it is less suitable in young children, as the patient is required to read a series of presented letter optotypes. More suitable for visual acuity testing in children is the so-called HOTV test, in which recognition is required but no literacy. Single letters, *H*, *O*, *T*, and *V*, surrounded by “confusion bars,” are presented in a random sequence on a computer screen, and the child has to match the letter being displayed to one on a handheld card. Picture optotypes facilitate visual acuity assessment in even younger children.

Retinoscopy (skiascopy), as opposed to subjective refraction, requires no decision or response from the patient and thus provides a more objective measurement of a patient’s refractive error. It is therefore ideal for refracting children. During retinoscopy, the examiner observes the movement of the eye’s red reflex through the peephole of the retinoscope while sweeping a band of diverging light (intercept) across the patient’s pupil. The movement of the retinoscopic reflex indicates the location of the “far point” of the eye, when the eye is in its relaxed position, that is, in the absence of accommodation. When the far point is beyond the peephole, for example, the portion of the returning light that passes through the peephole causes the red reflex to move in the same direction that the intercept is swept (“with” movement). When refracting children, the examiner manually places lenses over the examined eye to “neutralize” the reflex. Neutralization occurs when the eye’s far point is moved to the peephole of the retinoscope. If the patient’s eye is focused at the peephole, the portion of the returning light that passes through the peephole suddenly appears to the examiner to fill the patient’s whole pupil, with no apparent movement of the red reflex.

Non-cycloplegic retinoscopy, in particular, means that retinoscopy is performed without applying cycloplegic agents to paralyze accommodation. This is advantageous because it avoids optical aberrations uncovered by dilating the pupil that can cause confusing reflexes and thus yield a different refractive finding. Some practitioners, however, prefer to use cycloplegic agents both to inhibit accommodation, yielding a more stable measurement, and to dilate the pupil, because with a dilated pupil the primary reflexes are observed more readily.

Testing for stereoacuity or stereopsis is checking the child’s ability to perceive depth, that is, the ability for the brain to discriminate objects in depth via horizontal disparity between their images. As both eyes have to work together to have stereoscopic vision, the measurement of stereoacuity assesses the binocular status and is thus frequently used to screen for binocular vision disorders including anisometropia and strabismus. Stereoscopic perception may be tested using two-dimensional figures by presenting each eye with similar images having horizontally offset portions to produce retinal image

disparities. The “Random Dot” test, for instance, is a commonly used clinical test to measure stereopsis. Random Dot stereograms consist of two fields of randomly scattered dots, projected to each eye separately, for instance via a haploscopic device. The dots are identical, except for a group of dots that is displaced horizontally, which produces the perception that this group of dots is coming towards the observer.

Cover tests, such as the alternating cover test or the cover-uncover test, are reliable measures of eye alignment. The latter, for instance, is designed to detect a tropia (manifest deviation of one eye when both eyes are open) in patients who appear to have straight eyes and may be fusing. The examiner briefly occludes one eye and observes the fellow eye for a shift as the occluder is introduced. Any refixation movement is an indication of manifest esotropia, exotropia, or hypertropia depending on the direction of the shift. The amount of deviation can be quantified with the help of prisms, by neutralizing the observed movement.

There are simple but effective methods for assessing ocular alignment that use reflected light, such as the Hirschberg and the Brückner tests. During the Hirschberg test, the examiner holds a hand light close to the patient, with an “accommodative” (fine detail) fixation target usually placed just above or below the light to control accommodation. Eye alignment is assessed based upon the location of the first Purkinje image, which is the virtual image of the hand light reflected from the front surface of the cornea, formed about 4 mm behind the cornea. This first Purkinje image is commonly referred to as the corneal light reflex. Corneal light reflexes that are slightly decentered nasally but symmetric indicate normal ocular alignment. In a patient with strabismus, the corneal light reflexes are asymmetric, with the corneal light reflex in the deviating eye shifting eccentrically.

The Brückner reflex test also uses the positions of the corneal light reflexes to screen for strabismus, but in addition it can identify anisometropia and ocular media opacities. The Brückner test is performed by illuminating both eyes simultaneously with a broad light beam from a direct ophthalmoscope, through which the eyes are viewed from about a meter away. This results in red fundus reflexes in addition to the corneal light reflexes. As with the Hirschberg test, the key sign of a normal exam is symmetry. In a strabismic patient, the deviated eye often has a brighter red reflex as well as a decentered corneal light reflex. Unequal reflexes are also observed in patients with anisometropia, and the red reflex will appear abnormal in an eye with media opacities, with discrete media opacities visible directly.

2.3 Newer Screening Modalities

A major innovation in screening technology appeared to be the introduction of automated vision screening modalities in the late 1970s [Pfe06], commonly known as photoscreening or photorefractive devices. Numerous instruments have been described in the literature since then, attempting to quickly, easily, and objectively assess eye alignment, refractive error, media opacities, and other ocular abnormalities.

Based on their optical design, most photoscreeners can be grouped into three categories, which have been implemented in a variety of photographic and computer- and video-based formats: the on-axis (coaxial) designs, both “orthogonal” and “isotropic,” and the off-axis design (“eccentric”) [Sim96].

On-axis systems involve a coaxial camera and flash. In orthogonal on-axis photorefraction, in particular, sectors of cylindrical lenses are employed, concentrating the returning light from the eye through each sector into the “leg” of a star pattern. From variations in the resultant star pattern, defocus and astigmatism can be assessed.

Isotropic on-axis photorefraction requires several images to be taken, while the camera is focused in different planes from one picture to the next. The first photograph is usually taken with the camera focused on the plane of the child’s pupils, to measure pupil sizes and assess alignment via the Hirschberg test using the corneal light reflexes. Two more pictures are taken out-of-focus, with the camera focusing behind and in front of the child’s pupils respectively. Refractive error is then calculated from the lengths of the blur radii.

Even though on-axis photorefraction may be more sensitive to astigmatism than off-axis system, in which the flash or light source is eccentric to the camera aperture, it cannot be used for an adequate Brückner test, and it is difficult to confirm accurate fixation from its out-of-focus images [Sim96].

Three reflections are observed during off-axis photorefraction, the red-orange fundus reflex (Brückner reflex), the corneal light reflex (Hirschberg reflex), and an orange-yellow reflex extending in from one side of the pupil resulting from the eccentricity of the flash source. The latter is called a crescent, from whose size and location refractive error can be estimated, in addition to the assessment of eye alignment and ocular media clarity from the corneal light reflex and the red-orange fundus reflex respectively.

Most commercially available photoscreeners are based on the principle of eccentric photorefraction and are therefore off-axis systems. Photographic-based examples of such systems are the MTI PhotoScreener and the Visiscreen 100 (or Visiscreen OSS-C). The

latter (Vision Research Corporation; Birmingham, AL) obtains a single exposure with an electronic flash placed just eccentric to the aperture of a 35 mm camera with a telescopic lens, with the camera mounted about 2.5 m away from the child [Pfe06]. Although this system is easy to administer, a major disadvantage is the time delay of interpretation of the results. The undeveloped 35 mm film used for the photographs has to be shipped to the company first for processing, where the resultant photographs are later analyzed by five full-time technicians for refractive error, media opacities, and strabismus [Pfe06]. Another drawback of the Visiscreen system is that it requires the child to place his or her head against a headrest while the photograph is taken.

The MTI PhotoScreener (Photoscreener, Inc. (formally MTI); West Palm Beach, FL) uses instant film instead, and the child is screened remotely from a distance of about 1 m. Two photographs are taken, with the employed eccentric flash rotating 90 degrees in between, thus allowing measurement along 2 orthogonal meridians. The horizontal and vertical photographs are captured on the same Polaroid film for later interpretation by eye care specialists or by the Vanderbilt Ophthalmic Imaging Center. The MTI PhotoScreener has demonstrated high sensitivity and specificity rates in several studies [Ott95], [Don00], [Don02], [Rog08]. However, several drawbacks of the system should be mentioned. First of all, camera maintenance is an issue, common to all current analog cameras. Not only has discontinuation of the originally used Polaroid 337 film resulted in expensive upgrades of older MTI PhotoScreeners so that it functions with the newer Polaroid 667 film [Pfe06], but also Polaroid film itself is expensive. The need for skilled and sometimes costly interpretation of the photographs, along with the inherent delay while photographs are collected and interpreted, are further disadvantages of the MTI PhotoScreener [Rog08].

Newer off-axis systems are based on digital imaging technology, such as the iScreen and the Power Refractor (now PlusOptiX S04). The iScreen (iScreen, LLC; Memphis, TN), for example, is a digital off-axis photorefractor with a fixed focal length, connected to a laptop computer [Ken00], [Pfe06]. Digital color images are captured binocularly, with the child sitting approximately 0.68 m in front of the camera unit. However, the child is still required to place his or her head against a head rest, and the captured images have to be electronically transmitted to the iScreen scoring center in Memphis for off-site analysis, thus creating a time delay and expense for every interpretation.

The Power Refractor (now PlusOptiX S04) (PlusOptix GmbH; Nürnberg, Germany) is a video-based photoscreener that uses infrared light instead of a xenon flash tube. More precisely, it consists of six infrared LED segments that are arranged eccentrically around a digital video camera lens [Sch02], [Abr03]. The child is screened remotely, from a distance of about 1 m. A major advantage of this video-based off-axis

system is that analysis is automated. The computer system itself analyzes the captured binocular image and generates a report of both refractive error and eye alignment.

A head-to-head comparison of different vision screening methods has been published by the Vision in Preschoolers (VIP) Study Group [Sch04], [Sch05]. The comparison included traditional methods and the above-mentioned photoscreening devices (except for the Visiscreen), as well as two autorefractors (the Nikon Retinomax [Right Medical Products; Virginia Beach, VA] and the SureSight Vision Screener [Welch Allyn, Inc., Skaneateles Falls, NY]). The Vision in Preschoolers Study was a multi-phased, multi-center, clinical study to evaluate preschool vision screening tests. In Phase I of the VIP Study, all tests were administered by highly skilled, licensed eye care professionals (optometrists and pediatric ophthalmologists) [Sch04], while Phase II compared the performance of trained nurses and lay personnel in administering preschool vision screening tests [Sch05]. The results of both phases of the VIP Study have shown that the two autorefractors belonged to the best performing screening methods, with higher sensitivities and specificities than the other instruments based on photoscreening technology. However, a major disadvantage of autorefractors as screening tools for amblyopia is that they are incapable of detecting strabismus, a primary cause of amblyopia.

Chapter 3

Polarization and the Eye

3.1 Polarization of Light

Historically there have been different theories on the nature of light, such as light's being composed of particles (corpuscles) or waves. To describe the various phenomena demonstrated by light, we have to accept the wave-particle duality. The present-day view of light as an electromagnetic wave began with Maxwell's mathematical theory of the propagation of electromagnetic waves, which was experimentally confirmed by Hertz. Maxwell's equations form the foundation of electromagnetic theory. All macroscopic phenomena of light, such as interference, reflection, refraction, diffraction, polarization, etc., can be completely explained by this theory.

In this context, light may therefore be described as a transverse electromagnetic wave, whose oscillating electric and magnetic fields are both perpendicular to the direction of propagation. Due to its orthogonality and proportionality to the electric field, the magnetic field is conventionally ignored when considering polarization, and only the electric field vector is described instead, which always oscillates perpendicular to the direction that the wave advances. The magnetic field would serve just as well, but it has become customary to use the electric field in order to specify the polarization properties of electromagnetic waves. The electric field vector \vec{E} can be resolved into horizontal and vertical components, \vec{E}_x and \vec{E}_y , respectively. The relationship between these two electric field components defines the “state of polarization” of the light. Considering a wave traveling in the positive direction along the z axis as a function of time, the electric field vector can be written as:

$$\vec{E}(z, t) = \vec{E}_x(z, t) + \vec{E}_y(z, t) \quad (3.1)$$

with

$$\begin{aligned}\vec{E}_x(z, t) &= E_{0x} \cos(\omega t - kz) \vec{e}_x \\ \vec{E}_y(z, t) &= E_{0y} \cos(\omega t - kz + \delta) \vec{e}_y\end{aligned}\tag{3.2}$$

where E_{0x} and E_{0y} are the peak amplitudes of the orthogonal components, \vec{e}_x and \vec{e}_y the unit vectors in the x and y directions, t is the time, ω the angular frequency, k the wave number magnitude, and δ the relative phase difference between the constituent waves. The term $\omega t - kz$ is called the propagator.

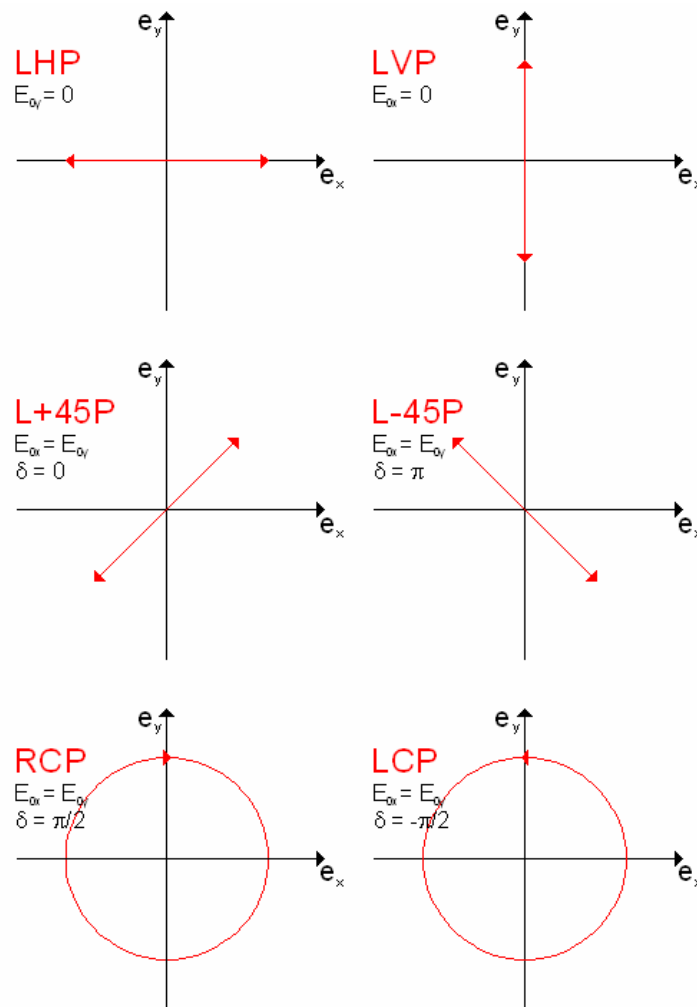


Figure 3.1: Pictorial representation of polarization (Lissajous figures). From top to bottom: linearly horizontal/vertical polarized light (LHP/LVP), linear $\pm 45^\circ$ polarized light (L+45P/L-45P), and right/left circularly polarized light (RCP/LCP).

Pictorially, the polarization state can be represented by the path that the tip of the electric field vector traces with time as viewed along the propagation axis looking toward the source (Lissajous figures). In general, the pattern mapped out by the tip of \vec{E} is an ellipse, but there are several combinations of phase and amplitude that are especially important.

3.1.1 Linearly Polarized Light

In the case of linear polarization, a single line is mapped out by the tip of the electric field vector. Consequently the orientation of the electric field is constant. The direction of the traced line depends on the relative amplitudes of the two orthogonal field components. Light is linearly polarized if the relative phase difference δ is zero or an integer multiple of $\pm\pi$, i.e. both electric field components are in phase. This leads to the simplified equation for the electric field vector:

$$\vec{E}(z,t) = (E_{0x}\vec{e}_x + E_{0y}\vec{e}_y)\cos(\omega t - kz) \quad (3.3)$$

There are two special cases of linear polarization, namely linearly horizontal and vertical polarized light. Light is horizontally polarized (LHP) if E_{0y} is zero, whereas if E_{0x} equals zero, the light is said to be vertically polarized (LVP).

3.1.2 Circularly Polarized Light

If light is composed of equal amounts of horizontally and vertically polarized light, or in other words if both orthogonal waves have the same magnitude ($E_{0x} = E_{0y} = E_0$) but their phase difference is $-\pi/2 + 2m\pi$, where m is any integer, the electric field can be represented as:

$$\vec{E}(z,t) = E_0[\cos(\omega t - kz)\vec{e}_x \pm \sin(\omega t - kz)\vec{e}_y] \quad (3.4)$$

This wave is called circularly polarized. Instead of having a constant orientation as with linear polarization, the direction of the electric field vector rotates over time, but its amplitude remains constant. In this special case, the tip of the electric field vector traces a circle (see Figure 3.1). The electric field vector makes one complete revolution as the light advances through one wavelength. The direction of rotation as seen from an observer

toward whom the wave is propagating defines the handedness of circularly polarized light. This depends on which of the orthogonal constituent waves lags behind. For right circularly polarized light (plus sign in equation (3.4)) the electric field vector appears to be rotating clockwise, whereas the rotation is counterclockwise for left circularly polarized light (minus sign).

3.1.3 Elliptically Polarized Light

The most general form of polarization occurs when the constituent waves are neither equal in amplitude nor possess a phase difference of 0 or $\pi/2$. Both the magnitude and the direction of the electric field change over time. Such light is called elliptically polarized, as an ellipse is traced by the tip of the electric field vector instead of a line or a circle. The equation of an ellipse can be obtained from equations (3.2) by eliminating the time-space propagator $\omega t - kz$ [Col98]:

$$\left(\frac{\vec{E}_x(z,t)}{E_{0x}}\right)^2 + \left(\frac{\vec{E}_y(z,t)}{E_{0y}}\right)^2 - 2\left(\frac{\vec{E}_x(z,t)}{E_{0x}}\right)\left(\frac{\vec{E}_y(z,t)}{E_{0y}}\right)\cos\delta = \sin^2\delta \quad (3.5)$$

The equation is called a polarization ellipse. It describes an ellipse, whose semi-major axis b forms an angle α with the E_x axis, where

$$\tan 2\alpha = \frac{2E_{0x}E_{0y}\cos\delta}{E_{0x}^2 - E_{0y}^2} \quad (3.6)$$

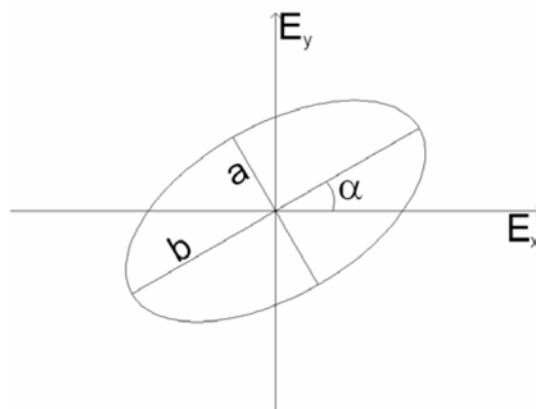


Figure 3.2: Polarization ellipse.

The ellipse is further characterized by its ellipticity ε , a function of the relative lengths of the semi-axes of the polarization ellipse. ε is defined as $\arctan(b/a)$, which ranges between 0° and $\pm 45^\circ$.

The polarization azimuth α , ellipticity, and handedness of the polarization ellipse are sufficient to entirely describe any polarization state of light. Elliptically polarized light may be thought of in terms of combinations of linearly or circularly polarized light, which are both considered to be special cases of elliptical polarization. In circularly polarized light, for instance, the ellipticity is 45° .

As opposed to polarized light, where the electric field oscillates in a preferential direction, in “natural” or non-polarized light the electric field oscillates in random directions perpendicular to the axis of propagation.

3.2 Birefringence

Many crystalline materials are optically anisotropic, that is their optical properties are not constant in all directions. Anisotropy in the refractive index, for example, causes retardation or phase lag of one of the two orthogonal electric field components with respect to the other, which leads to a change in the polarization state of the light. A material that causes an anisotropic retardation of light is said to have birefringence [Bro98].

Light propagates through a transparent medium by exciting the electrons within the material, with consequent formation of secondary wavelets. The oscillating frequencies of the electrons depend on the binding forces in corresponding directions in the material. These binding forces play an important role with regard to the velocity of the light wave and with it the refractive index, as the velocity of the light wave is determined by the difference of the frequencies of the electric field and the natural frequency of the electrons. Anisotropy in the binding force therefore is directly correlated with anisotropy of the refractive index. Figure 3.3 shows a mechanical model of a charged shell bound to a positive nucleus by a set of springs to emphasize this correlation.

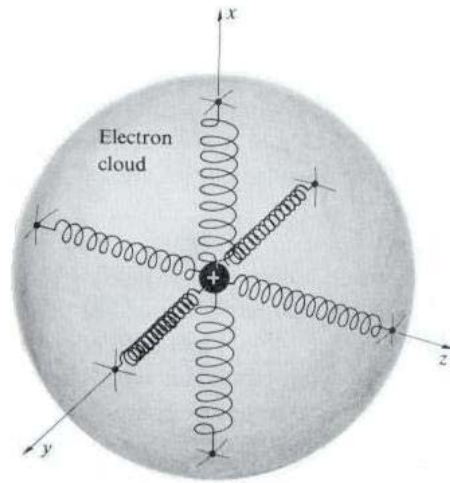


Figure 3.3: Mechanical spring model [Hec02].

Three different springs of different stiffness represent the anisotropy in the binding force of the electron. An electron that is displaced from equilibrium along a direction parallel to one of these springs will oscillate with a different characteristic frequency than if it were displaced in some other direction.

The refractive indices in all different directions within the crystal can be described by an index ellipsoid (Figure 3.4), where the index of refraction for every direction of polarization is represented by the distance from the origin of the index ellipsoid to the surface, on a plane of intersection that is determined by the angle of incidence, normal to the direction of propagation.

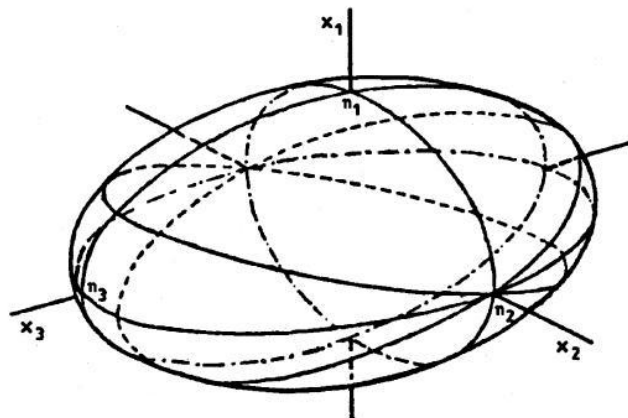


Figure 3.4: Refractive index ellipsoid [Mül00].

Birefringent crystals that display two principal indices of refraction are called uniaxial, with calcite being the most prominent example. Unpolarized light traveling through a uniaxial crystal generally bifurcates into two rays. This phenomenon was first observed in 1669 by Bartholinus, which he called double refraction. In accord with a suggestion made by Bartholinus, the two rays, produced by respective indices of refraction n_o and n_e , are named the ordinary ray and the extraordinary ray, because the ordinary ray obeys the ordinary law of refraction, i.e. Snell's law, while the extraordinary ray does not.

The numerical difference $n_e - n_o$ is a measure of birefringence. By definition, a birefringent material where $n_e \geq n_o$, and as a result $v_e \leq v_o$, is called positive, whereas in the opposite case the material is said to be negative. Calcite is an example of a negative uniaxial crystal.

In contrast to uniaxial crystals with two principal indices of refraction, crystalline substances having three different principal refractive indices are known as biaxial. The birefringence of biaxial crystals is given by the numerical difference between the largest and smallest of these indices.

3.2.1 Wave Plates

Wave plates are made of birefringent materials, such as quartz, mica, or polymer. They are also known as retarders because they change the polarization state of incident light by introducing a retardance or phase shift between the two orthogonal polarized components. Suppose that linearly polarized light is striking a wave plate at normal incidence, with the optic axis of the retarder being parallel to the front and back surfaces and forming an angle of 45° with the incident plane of polarization. In this configuration, the direction of light propagation is perpendicular to the optic axis, so that the resolved electric field component parallel to the optic axis, i.e. the extraordinary wave, is not deviated, and all the light travels along the same path. Thus, after traversing the birefringent plate, the resultant electromagnetic wave is the superposition of the extraordinary and ordinary waves, which now have a phase shift relative to each other.

Recall that in negative uniaxial materials, such as calcite, the extraordinary ray travels faster, that is, the component polarized parallel to the optic axis. Thus, in a negative uniaxial retarder, the direction of the optic axis is often referred to as the fast axis, whereas the axis perpendicular to it is referred to as the slow axis. These principal axes are reversed in positive uniaxial retarders, such as quartz, with the slow axis corresponding to the optic axis.

A wave plate that introduces a relative phase shift of π radians or 180° between the two orthogonal components of polarized light is known as a half wave plate. Half wave plates are sometimes called polarization rotators, as they have the unique property of flipping the polarization direction of incoming, linearly polarized light by twice the angle between the retarder's fast axis and the input plane of polarization (Figure 3.5), thus flipping the plane of polarization about the fast axis of the retarder. When the angle between the retarder's fast axis and the input plane of polarization is 45° , horizontal polarized light is converted to vertical polarized light, and vice versa.

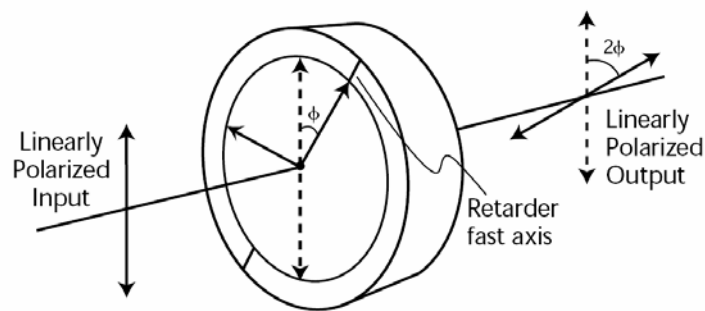


Figure 3.5: A half wave plate rotates the plane of linearly polarized light by twice the angle between the retarder's fast axis and the input plane of polarization, thus flipping the plane of polarization about the fast axis of the retarder. [Mea05].

A quarter wave plate, on the other hand, introduces a phase difference of $\pi/2$ or 90° between the orthogonal components of polarization. It is therefore often used to convert linearly polarized light to circularly polarized light.

3.2.2 Form Birefringence

Form birefringence is a special type of birefringence first described by Wiener [Wie12]. Form birefringence, as opposed to intrinsic birefringence arising from crystalline substances that are optically anisotropic as described above, is due to an ordered arrangement of similar elements, even if each element is optically isotropic, whose size is large compared with the dimensions of molecules, but small compared with the wavelength of the incident light. For elongated structures that obey the aforementioned requirements, the Wiener equation relates the birefringence, given by the difference between the extraordinary and ordinary indices of refractions (n_e, n_o), to the fractional volumes (f_1, f_2)

and refractive indices (n_1, n_2) of long thin parallel cylindrical rods (subscript 1) and the medium in which they are buried (subscript 2):

$$n_e^2 - n_o^2 = \frac{f_1 f_2 (n_1^2 - n_2^2)^2}{(1 + f_1) n_2^2 + f_2 n_1^2} \quad (3.7)$$

3.3 Müller- Stokes Matrix Calculus

3.3.1 Stokes Vector Representation

The polarization of light can be entirely described by the Stokes vector, first introduced by George Stokes in 1852. The Stokes vector is composed of four quantities, the Stokes parameters, which are functions only of observables of the electromagnetic wave. Thus the Stokes parameters can be obtained directly from an experiment. The quantity of the optical field that can be observed or measured is the intensity. In mathematical terms the intensity of a light wave is defined by the time averaged magnitude of the Poynting vector:

$$I \equiv \langle |\vec{S}| \rangle_T = c \varepsilon_0 \langle |\vec{E}|^2 \rangle_T \quad (3.8)$$

where $\langle \rangle_T$ denotes the time averaged value, ε_0 is the permittivity and c the speed of light in vacuum. The Poynting vector \vec{S} itself describes nothing else but the energy flow of the electromagnetic field, i.e. the energy per unit time and unit area. In case of a transverse electromagnetic plane wave, it can be simplified to the above shown form (3.8), so that the intensity is proportional to the square of the electric field vector.

The introduced description of light in terms of the polarization ellipse (3.5) proves to be helpful for the derivation of the Stokes parameters. Based on this equation the four parameters can be obtained after some algebraic transformations. In order to represent the polarization ellipse in terms of the observables of the electric field, the time average has to be taken first:

$$\frac{\langle |\vec{E}_x(z,t)|^2 \rangle_T}{E_{ox}^2} + \frac{\langle |\vec{E}_y(z,t)|^2 \rangle_T}{E_{oy}^2} - \frac{2 \langle \vec{E}_x(z,t) \vec{E}_y(z,t) \rangle_T}{E_{ox} E_{oy}} \cos \delta = \sin^2 \delta \quad (3.9)$$

where

$$\langle \vec{E}_x^2(z, t) \rangle = \frac{1}{2} E_{ox}^2, \quad \langle \vec{E}_y^2(z, t) \rangle = \frac{1}{2} E_{oy}^2, \quad \langle \vec{E}_x(z, t) \vec{E}_y(z, t) \rangle = \frac{1}{2} E_{ox} E_{oy} \cos \delta \quad (3.10)$$

Substituting these time averages in (3.9), multiplying by $4E_{ox}^2 E_{oy}^2$ and then adding and subtracting the quantity $E_{ox}^4 + E_{oy}^4$ to the left side yields the following equation [Col98]:

$$(E_{ox}^2 + E_{oy}^2)^2 - (E_{ox}^2 - E_{oy}^2)^2 - (2E_{ox} E_{oy} \cos \delta)^2 = (2E_{ox} E_{oy} \sin \delta)^2 \quad (3.11)$$

This equation can be rewritten as

$$S_0^2 = S_1^2 + S_2^2 + S_3^2 \quad (3.12)$$

where

$$\begin{aligned} S_0 &= E_{ox}^2 + E_{oy}^2 \\ S_1 &= E_{ox}^2 - E_{oy}^2 \\ S_2 &= 2E_{ox} E_{oy} \cos \delta \\ S_3 &= 2E_{ox} E_{oy} \sin \delta \end{aligned} \quad (3.13)$$

These four quantities are the Stokes parameters. As can be seen, the Poynting vector is directly proportional to the first Stokes parameter S_0 , which is simply the incident irradiance. The latter three parameters provide information on the state of polarization. The second parameter S_1 , for instance, describes the tendency of light to be horizontally polarized. In other words, S_1 will be positive ($S_1 > 0$) when the light wave exhibits a preference for linearly horizontal polarized light, whereas $S_1 < 0$ indicates vertically polarized light. S_2 , the third Stokes parameter, describes the predominance of linear $+45^\circ$ polarized light ($S_2 > 0$) over linear -45° light ($S_2 < 0$). Finally, S_3 describes the preference of the light wave for right circular polarization, i.e. $S_3 > 0$ for right circularly polarized light, and $S_3 < 0$ for left circularly polarized light.

To better understand the significance of the Stokes parameters, one may prefer to think of the Stokes parameters as the differential polarization signal that would be measured by a differential pair of photodetectors [Bor99]. For example, if $I(\theta, \Delta)$

represents the intensity of light captured by a photodetector placed behind a polarizer at θ° from the horizontal and Δ is the phase lag of the \vec{E}_y component with respect to the \vec{E}_x component, then:

$$\begin{aligned} S_0 &= I(0^\circ, 0) + I(90^\circ, 0) \\ S_1 &= I(0^\circ, 0) - I(90^\circ, 0) \\ S_2 &= I(45^\circ, 0) - I(135^\circ, 0) \\ S_3 &= I(45^\circ, \pi/2) - I(135^\circ, \pi/2) \end{aligned} \quad (3.14)$$

(3.12) applies only when dealing with fully polarized light. In order to have a relation that satisfies any state of polarization, we have to write

$$S_0^2 \geq S_1^2 + S_2^2 + S_3^2 \quad (3.15)$$

Completely polarized light will then obey the identity, whereas the inequality sign is valid for partially polarized light (mixture of completely polarized and non-polarized light) or non-polarized light. The degree of polarization, DOP , is determined by

$$DOP = \frac{\sqrt{S_1^2 + S_2^2 + S_3^2}}{S_0} \quad (3.16)$$

which ranges from 0 to 1.

In general, the Stokes parameters are arranged as a column matrix, which is referred to as the Stokes vector \vec{S} :

$$\vec{S} = (S_0, S_1, S_2, S_3)^T \quad (3.17)$$

It is convenient to normalize the Stokes parameters by dividing each entry by S_0 , which means that the incident light has an irradiance of unity. For a non-polarized beam for example, the Stokes vector can then be expressed as $(1, 0, 0, 0)^T$.

State of Polarization	Normalized Stokes Vector
LHP	$\begin{pmatrix} 1 \\ 1 \\ 0 \\ 0 \end{pmatrix}$
LVP	$\begin{pmatrix} 1 \\ -1 \\ 0 \\ 0 \end{pmatrix}$
L+45P	$\begin{pmatrix} 1 \\ 0 \\ 1 \\ 0 \end{pmatrix}$
L-45P	$\begin{pmatrix} 1 \\ 0 \\ -1 \\ 0 \end{pmatrix}$
RCP	$\begin{pmatrix} 1 \\ 0 \\ 0 \\ 1 \end{pmatrix}$
LCP	$\begin{pmatrix} 1 \\ 0 \\ 0 \\ -1 \end{pmatrix}$

Table 3.1: Stokes vectors for some polarization states.

3.3.2 Müller Matrix Formalism

The matrix representation of the Stokes parameters leads to a very powerful mathematical tool for the treatment of the interaction of polarized light with elements which can change its state of polarization. In the Müller matrix formalism, polarization states of light are represented by Stokes vectors and every optical element can be described as a 4x4 matrix. The components of the so-called Müller matrix \mathbf{M} contain information about the change of polarization and retardation for a light beam passing through the optical element. There is a complicated but mathematically describable change of the initial polarization state, in other words the Stokes vector, on passing through polarization-altering media, described by serial multiplication of the Müller matrices of all contributing components.

$$\vec{S}_{out} = \mathbf{M}_n \cdot \dots \cdot \mathbf{M}_3 \cdot \mathbf{M}_2 \cdot \mathbf{M}_1 \cdot \vec{S}_{in} \quad (3.18)$$

where \vec{S}_{in} and \vec{S}_{out} denote the incident and outgoing Stokes vectors, respectively. The Müller matrix formalism is thus based on the assumption that the incident Stokes vector is linearly related to the polarization-changed Stokes vector by the transformation matrix.

A wave plate, for example, can be mathematically described by the following Müller matrix [Col93], where δ and θ denote the retardance and fast axis orientation of the retarder respectively:

$$\mathbf{M}_r = \begin{pmatrix} 1 & 0 & 0 & 0 \\ 0 & \cos^2 2\theta + \cos \delta \sin^2 2\theta & (1 - \cos \delta) \cos 2\theta & \sin \delta \sin 2\theta \\ 0 & (1 - \cos \delta) \sin 2\theta \cos 2\theta & \sin^2 2\theta + \cos \delta \cos^2 2\theta & -\sin \delta \cos 2\theta \\ 0 & -\sin \delta \sin 2\theta & \sin \delta \cos 2\theta & \cos \delta \end{pmatrix} \quad (3.19)$$

The eigenvectors of the Müller matrix define the slow and fast axes of the wave plate. The eigenvector associated with the retarder's lower index of refraction corresponds to the fast axis, whereas the slow axis eigenvector is orthogonal to the latter.

3.3.3 Poincaré Sphere

A very helpful illustration of polarization states and changes in these states can be obtained with the Poincaré sphere. It is a unit sphere with axes given by the Stokes parameters (S_1 , S_2 and S_3). Each possible polarization state can be described, via its "Stokes vector," as a

point on the surface of the Poincaré sphere. The change in polarization state of a polarized light beam passing through a medium that modifies the state of polarization (a retarder) can now be described in a relative simple way by the movement of the end of its Stokes vector across the sphere's surface [Jer54]. The Müller matrix of the retarder determines the direction and amount of rotation of the point representing the polarization state on the surface of the Poincaré sphere. The angle of rotation is equal to the retardation expressed in degrees, and the eigenvector of the Müller matrix represents the 3-dimensional position of the fast axis of the retarder, about which the polarization state rotates.

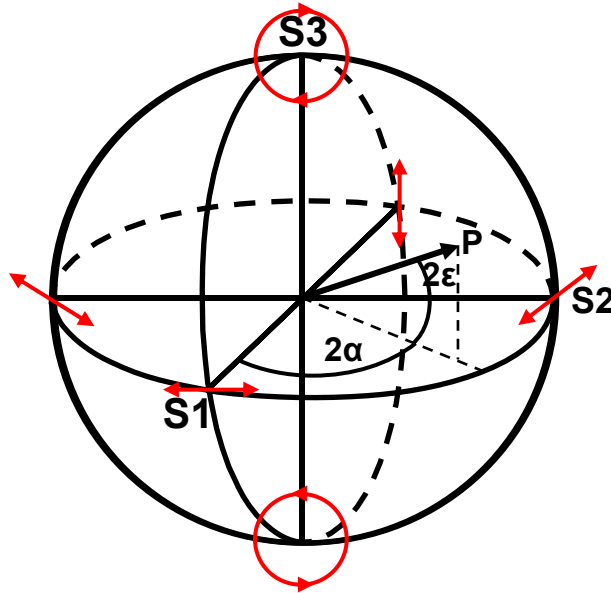


Figure 3.6: Poincaré sphere.

Having understood the significance of the Stokes parameters, in terms of their visualization on the sphere, it is the most convenient to express the Stokes vector related to spherical coordinates, in other words to the orientation (α) and ellipticity (ε) angles of the polarization ellipse. For a unit sphere, i.e. the normalized Stokes parameters are considered, the Stokes vector can be written as [Shu62]:

$$\vec{S} = \begin{pmatrix} 1 \\ \cos(2\varepsilon)\cos(2\alpha) \\ \cos(2\varepsilon)\sin(2\alpha) \\ \sin(2\varepsilon) \end{pmatrix} \quad (3.20)$$

Note that on the Poincaré sphere, the angles are given by twice the orientation (2α) and ellipticity (2ε). Points that lie on the equator indicate linearly polarized light, whereas the north and south poles represent right and left circular polarization, respectively. All other points on the sphere's surface relate to elliptically polarized states. With the exception of the sphere's origin, which represents non-polarized light, all other points positioned inside the Poincaré sphere represent partially polarized light, with the length of the Stokes vector indicating the degree of polarization.

When light passes through a common “linear” wave plate, the modified state of polarization can thus be obtained by rotating the point, mapped by the input Stokes vector, about the proper axis and through the proper angle. The axis of rotation is determined by the eigenvector of the linear retarder, which lies in the equatorial plane emerging from the sphere's origin to a point on the sphere. The eigenvector's orientation is given by twice the azimuth of the retarder's fast axis (2θ), measured from the S1 axis, positive toward S2. The initial polarization state rotates clockwise (looking at the arrowhead) around the eigenvector by an angle equal to the amount of retardance introduced by the retarder (δ).

3.4 Ocular Birefringence

A schematic drawing of the human eye is shown in Figure 3.7, for reference purposes. The eye possesses many highly organized structures that give rise to birefringence, with the cornea and retina being its major sources of birefringence. The crystalline lens exhibits birefringence as well, but its contribution is very little. Although the birefringent properties of the ocular media do not affect the optical function of the eye, in other words image formation on the retina, the cornea and to a much lesser extent the crystalline lens change the polarization state of light before reaching the retina. Thus, knowledge of the birefringent properties of these ocular media is essential if polarization-sensitive technology is used for the assessment of the retina. The birefringent properties and relevant anatomy of the lens and cornea are described first, followed by a detailed discussion of the polarization properties of the retina. As tears, aqueous humor, and vitreous humor do not contribute significantly to the total ocular birefringence, these media are not considered further.

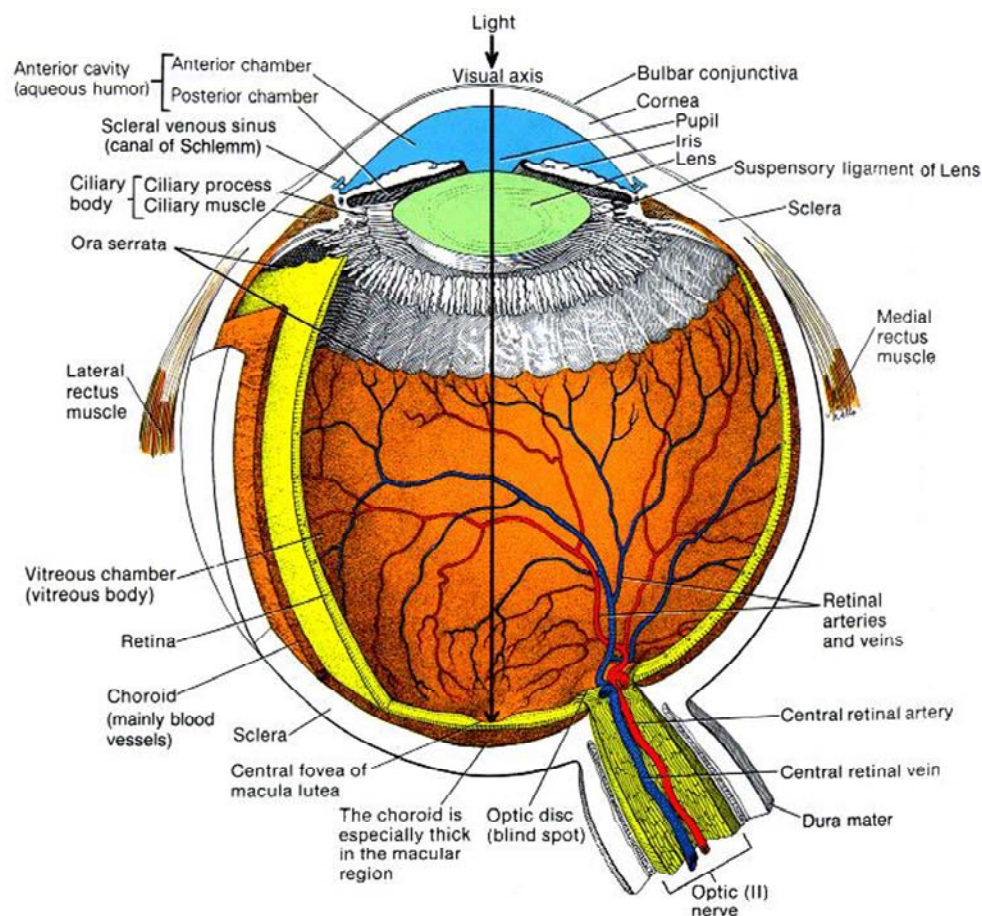


Figure 3.7: Schematic drawing of the human eye [Hic98].

3.4.1 Lenticular Birefringence

Together with the cornea, the biconvex crystalline lens is responsible for formation of the optical image on the retina. The crystalline lens is held in place by suspensory ligaments, or zonules, that are attached to the ciliary muscle. Ciliary muscle actions cause the zonular fibers to relax or tighten and thus provide accommodation, the active function of the crystalline lens.

The human crystalline lens possesses a complex anatomical structure, giving rise to both “intrinsic” and “form” birefringence. It is composed of lenticular cells (fibers), which are continuously formed throughout life. Old fibers are densely packed centrally, forming an increasingly large inelastic nucleus. In the outer part of the lens (cortex), the fibers are organized in an “onion-like” or layered structure. Intrinsic birefringence has its origin in the optical anisotropy of macromolecular aggregates within the fiber cells, whereas form

birefringence results from the regular arrangement of the fiber cells [Bet75]. However, the human crystalline lens does not contribute substantially to the overall birefringence of the eye. According to Bettelheim and Weale, the combined influence of form and intrinsic birefringence is very small, as both are approximately equal in magnitude and orientated perpendicular with respect to each other [Bet75], [Wea79]. This view is corroborated by the findings of Klein Brink, whose studies have shown that form and intrinsic birefringence of the lens are complementary and thereby tend to cancel each other out [kle91].

3.4.2 Corneal Birefringence

The convex transparent cornea is not only the major refractive component of the eye, but also contributes most (~80%) of the overall ocular birefringence. The human cornea is composed of five different layers, starting from posterior to anterior: the epithelium, Bowman's membrane, the stroma, Descemet's membrane, and the endothelium. Its main constituent is the corneal stroma, which makes up 90% of the entire thickness. The corneal stroma is composed of approximately 200 lamellae, lying parallel to the corneal surface [Bou91], [McC90]. Each of the corneal lamellae contains collagen fibrils, closely packed fibers embedded in an optically homogeneous ground substance [Mau57], [Don95]. The collagen fibers within individual lamellae are parallel, but they have different orientations with adjacent lamellae [Mar84], [Far90]. The stromal lamellae are in turn further stacked into layers.

Corneal birefringence is a combination of intrinsic and form birefringence, and is usually attributed to the stromal lamellae [Mau57]. Intrinsic birefringence arises from the optically anisotropic structure of the collagen fibrils themselves, with the axis of birefringence (slow axis) along the fibril length [Cop78]. The ordered arrangement of the fibers within individual lamellae, embedded in an isotropic ground substance of different refractive index, produces corneal form birefringence. Each lamella may be considered as a birefringent plate or linear retarder with its optic (slow) axis lying along the direction of the collagen fibers, leading to the simplified consideration of the corneal stroma as a series of stacked birefringent plates, with their optic axes lying at various angles to one another [Don95].

However, there has not been consensus on the exact order of the lamellae arrangement within the corneal stroma. Two principal models of corneal birefringence have been proposed in the literature. In the first model, which is of historic interest, the cornea is regarded as a uniaxial crystal, in which the lamellae are randomly oriented within the corneal stroma. In the second model, the cornea is regarded as biaxial crystal, based on a non-symmetric arrangement of lamellae that has a preferential orientation angle.

Valentin first postulated that the cornea behaves as a bent uniaxial crystal plate with the optic axis perpendicular to the corneal surface [Val61], based on his discovery that a dark cross-shaped figure (isocytres) with peripheral concentric colored bands (isochromes) was produced when placing the cornea between a polarizer and a crossed analyzer. The uniaxial model was supported by Stanworth and Naylor [Stan50], [Stan53], who interpreted the uniaxiality as an absence of preferential direction of lamellae in the corneal stroma. The random arrangement of lamellae is referred to by several other authors [Mau57], [Pos66].

Cope et al. found that the corneal “polarization cross” rotates as the polarizer and analyzer are rotated together by an equal amount, whereas it is more pronounced in the vertical-horizontal orientation [Cop78]. They claimed that the cross pattern is actually a pair of hyperbolae that join at their apices. When placing a quarter wave plate between the cornea and crossed analyzer, the hyperbolae separated as the system was rotated. Similar observations were mentioned by Cogan [Cog41]. He found that the cross pattern was only observable at a certain orientation of the cornea. At other orientations, the arms of the polarization cross are separate, and the dark figure assumes the appearance of a pair of conjugate hyperbolae, which is typical of the behavior of a biaxial crystal [Bou91].

Van Blokland and Verhelst [van87], using Müller matrix ellipsometry, found that the retardance has a saddleback-like appearance over the pupil, i.e. retardation decreases in the temporal and nasal direction and increases at the superior and inferior parts of the pupil. The orientation of the eigenvector is mainly along the upper-temporal to lower-nasal direction, while at greater eccentricities it tends toward a tangential orientation. Thus, the uniaxial model is a good approximation for the central cornea, but in taking larger eccentricities into account, Van Blokland and Verhelst invoked a biaxial crystal model to be more appropriate to explain the observed birefringence behavior of the human cornea, with its fastest principal axis normal to the corneal surface and its slowest nasally downward. They attributed the biaxiality to a preferred lamellar direction that is, in general, nasally downward. This interpretation was supported by McCally and Farrell who performed small-angle light-scattering experiments on rabbit cornea in vitro [McC82]. The biaxial model of corneal birefringence is supported by most recent studies and is now widely accepted [Don96], [Bon07], [Cav07].

The present state of knowledge on corneal birefringence can thus be summarized as follows: In general, the cornea behaves as a biaxial crystal with anisotropy in three directions. For a light beam approximately perpendicular to the corneal surface, however, the cornea can be approximated as linear retarder with a fixed retardance and with its slow axis parallel to the corneal surface.

Although being relatively constant over the entrance pupil for any given eye, corneal birefringence varies widely among individuals and eyes in both its retardance and azimuth [Kni02], [Wei02].

3.4.3 Retinal Birefringence

The retina is the multilayered sensory tissue of the posterior eyeball onto which light entering the eye is focused, forming a reversed and inverted image. The retina may be considered as being composed of ten different layers, starting from the vitreous to choroid [Dav84], [Bor97]: (i) Internal limiting membrane, formed by both retinal and vitreal elements [Dav84]; (ii) Retinal nerve fiber layer (RNFL), which contains the axons of the ganglion cells. These nerve fibers are bundled together and converge to the optic disc, where they leave the eye as the optic nerve. The cell bodies of the ganglion cells are situated in the (iii) ganglion cell layer. Numerous dendrites extend into the (iv) inner plexiform layer where they form synapses with interconnecting cells, whose cell bodies are located in the (v) inner nuclear layer; (vi) Outer plexiform layer, containing synaptic connections of photoreceptor cells; (vii) Outer nuclear layer, where the cell bodies of the photoreceptors are located; (viii) External limiting membrane, which comprises closely packed junctions between photoreceptors and supporting cells. The rods and cones reside in the (ix) receptor layer. These photoreceptors are capable of converting light into nerve impulses that are conducted and further relayed to the brain via the optic nerve; (x) Retinal pigment epithelium, whose cells supply the photoreceptors with nutrients. The retinal pigment epithelial cells contain granules of melanin pigment that enhance visual acuity by absorbing the light not captured by the photoreceptor cells, thus reducing glare. The most important task of the retinal pigment epithelium is to store and synthesize vitamin A, which is essential for the production of the visual pigment [Bor97]. The pigment epithelium rests on Bruch's membrane, a basement membrane on the inner surface of the choroid.

There are two areas of the human retina that are structurally different from the remainder, namely the fovea and the optic disc. The latter is situated about 3 mm (15 degrees of visual angle) to the nasal side of the macula, which is the central area of the retina [Sne89]. It contains no photoreceptors at all and hence is responsible for the blind spot in the field of vision. The fovea is a small depressed region at the center of the macula. There, the inner retinal layers are shifted aside, allowing light to pass unimpeded to the photoreceptors. The fovea is the region of maximum visual acuity. Only tightly packed cones, and no rods, are present at the foveola, the center of the fovea. The elongated axons of these cone cell bodies are called Henle fibers. The Henle fibers extend

precisely radially within about the central five degrees centered on the fovea, similar to the spokes of a wagon wheel.

The retina is the second-most birefringent medium in the eye. The polarization properties of the retina have been investigated since 1844, when Haidinger first described the bowtie- or propeller-shaped pattern (Haidinger brush phenomenon) that appears to rotate about the point of fixation if a white background is viewed through a rotating polarizer. The retina contains both intrinsic and form birefringent structures. One of these is the Henle fiber layer in the perifoveal region that is known to have form birefringence. Klein Brink and van Blokland argued that the radial arrangement of the Henle fibers surrounded by the cytoplasm of Müller cells with mutually different refractive indices causes uniaxial form birefringence [kle88]. The optic axis, which represents the slow axis, is directed along the fibers, so that the Henle fiber layer acts like a radially symmetric positive birefringent medium.

In addition, intrinsic birefringence is attributed to the lutein pigment particles that are aligned along the Henle fibers and the ends of the nerve fibers closest to the fovea. But their contribution is only small because of the low concentration of preferentially oriented lutein molecules [kle88].

The second source of retinal form birefringence is the RNFL. Bearing Wiener's concept of form birefringence in mind, at first sight the RNFL does not necessarily seem to qualify as a form birefringent medium, as the ganglion cell axons have diameters much greater than the wavelength of light. But these axons contain numerous microtubules, cylindrical intracellular organelles with diameters smaller than the wavelength of the illuminating light. The highly ordered (parallel) structure of the microtubules gives rise to RNFL birefringence [Kni89], [Dre92]. Similar to the Henle fiber layer in the macula, this layer is at least approximately radially symmetric close to the optic disc.

The birefringent property of the retinal nerve fiber layer has been used to determine the thickness of the retinal nerve fiber layer (RNFL) around the optic disc [Wei90]. Dreher et al. developed a scanning laser polarimeter (SLP), which is a confocal scanning laser ophthalmoscope with an integrated ellipsometer to measure retardation [Dre92(2)]. It is available as a commercial instrument, the GDx (Carl Zeiss Meditec AG, Jena, Germany). There is a linear relationship between the thickness of a birefringent medium and its retardation (Wiener's formula). Thus by measuring the total retardation of the human retina point by point in a raster pattern, from the change in polarization state in the light retroreflected from the fundus of the eye, a "topographic map" of the nerve fiber thickness in the eye's retina can be created, providing a quantitative method for detecting evidence of

eye diseases such as glaucoma, which is characterized by loss of nerve fibers in its early state [Dre94], [Wei95].

Chapter 4

Retinal Birefringence Scanning (RBS)

The birefringence of the retina has also been used in retinal birefringence scanning by our group. Retinal birefringence scanning (RBS) is a technique to monitor the changes in the state of polarized light retroreflected from the fundus of the human eye. It was adapted by Guyton and colleagues to detect foveal fixation [Guy00], [Hun99]. In addition, we recently reported the utilization of the RBS technique for biometrics security purposes [Ago08].

4.1 Assessment of Foveal Fixation

In RBS for eye fixation monitoring, polarized near-infrared light is directed in a circular scan onto the retina, with a fixation point in the center. The change in polarization that occurs between the incident and the reflected light, after the double-pass through the ocular birefringence, is detected by means of differential polarization detection. Due to the distinctive radial pattern of the birefringent Henle fibers, a characteristic frequency appears when the scan is exactly centered on the fovea, which is the case with central fixation. Thus, by analyzing the generated frequencies in the obtained electrical signal, foveal fixation of the human eye can reliably be assessed.

Original studies with the so-called Eye Fixation Monitor have shown that when an eye was fixated on a point at the center of the circular scan, a strong frequency occurred in the measured signal that was twice the scanning frequency ($2f$), whereas with paracentral fixation, the periodicity of polarization-related changes was predominantly equal to the scanning frequency (f). The origin of these frequencies can readily be explained intuitively by the radial symmetry of the Henle fiber birefringence about the fovea, which changes the polarization state of traversing light. When an individual fixates on a target, that target is imaged onto the fovea. With the eye fixating properly, the fovea is encircled by the scanned annulus of near-infrared light (Figure 4.1 A). Thus the concentric circle of light

falls entirely on the radial array of birefringent fibers, and therefore, due the radial symmetry of the fibers, each orientation is passed twice during the 360° scan, so that the polarization state changes at twice the scanning frequency. This leads to a strong frequency component that is 2 times the scanning frequency. During paracentral fixation, however, the scan is decentered (Figure 4.1 B). Thus the orientation of the radially arranged nerve fibers changes only once during each single scan, resulting in a frequency component equal to the scanning frequency [Guy00], [Hun99].

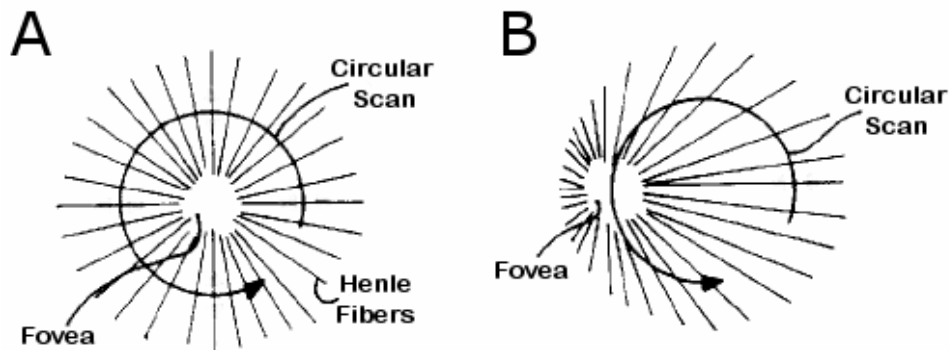


Figure 4.1: Central (A) versus paracentral (B) fixation. Modified from [Guy00].

Various other techniques are available for estimating the direction of eye fixation [You75], including scleral search coils, electro-oculography (EOG), and video-based eye trackers. However, among other limitations, none of these methods detects true foveal fixation, but rather infers it from the orientation of the globe (eye position) through a calibration step. In contrast, by detecting the radial symmetry of foveal architecture, RBS can detect true foveal fixation of the eye, without any need for calibration.

The scleral search coil technique, for example, measures eye movements and eye position based on electromagnetic induction [Rob63], [Col75], utilizing a time-varying magnetic field that induces current in a coil imbedded in a scleral contact lens. The major disadvantage of this method is its invasive nature. EOG uses electrodes placed on the skin near the eyes to measure corneo-retinal potentials that are related to eye position within the orbit [Kna94]. Weak signals, non-linear output, and muscle artifacts are substantial difficulties with electro-oculography. In addition, EOG requires uncomfortable site preparation and is in general frightening to young patients. Video-based eye trackers monitor the horizontal and vertical positions of the pupil, most often relative to corneal

light reflexes (Purkinje images), to estimate eye position. Both head-mounted and remote systems exist [Mor04], however either one is susceptible to head-versus-camera motion, so that either strict control of, or knowledge of, head position is required to accurately determine the position of the eye.

With RBS providing an automated, remote, and noninvasive technique to monitor true foveal fixation, there are numerous potential applications of this technology. For example, RBS could monitor fixation during visual field testing, laser eye surgery, and other forms of diagnostic and therapeutic ophthalmic procedures. Eye fixation monitoring may also be useful for the diagnosis and management of children with attention deficit hyperactivity disorder (ADHD), who are known to have difficulty in maintaining fixation. ADHD is a significant public health problem without validated objective markers to date. In addition, a RBS-based eye fixation sensor coupled to a switch could enable remote control of external devices by eye fixation alone. The quality of life of handicapped individuals could be improved, for instance, as a remote, visual-activated switch could enable them to control their environment just through visual contact. Finally, bilateral, simultaneous RBS (binocular RBS) can be used to screen individuals for eye misalignment.

4.2 Pediatric Vision Screening Using Binocular RBS

The ability to assess foveal fixation directly, without the need for calibration to external features, allows investigation of less cooperative subjects, including infants and young children. Thus by detecting foveal fixation of both eyes simultaneously, binocular RBS has great potential to screen infants and young children for strabismus, the predominant amblyogenic risk factor. Combining such a binocular eye fixation monitor with an ocular focus detection system facilitates screening for both primary causes of amblyopia.

Our laboratory within the Division of Pediatric Ophthalmology and Adult Strabismus at the Wilmer Ophthalmological Institute, The Johns Hopkins University School of Medicine, has been developing a “Pediatric Vision Screener” (PVS) that can simultaneously detect proper alignment as well as proper focus of infants’ eyes. The latter is determined by assessing the size of the double-pass blur image produced from a point source of light by means of a bull’s-eye photodetector. More precisely, a blurred patch of light is formed on the retina, when an eye is looking toward, but is not focused on, a point source of light, so that by measuring the size of that retinal blur patch, the amount of

defocus can be assessed [Wes94], [Kar93]. Guyton and colleagues developed a technique to assess the size of the double-pass blur image automatically [Guy00], [Hun04], with the critical component of the focus detection system being a bull's-eye photodetector consisting of two concentric active surfaces, a circular center area with a surrounding annulus. This center-annulus photodetector is positioned optically conjugate to the light source, so that if the light is in focus on the retina, the double-pass light will come to a focus only within the center area of the photodetector, while defocused light falls on both active areas. Thus, the goodness of focus that an eye is experiencing can be determined by the ratio of the detected center to annulus signals.

The optical design of the RBS system, as implemented binocularly in the prototype of the PVS [Hun04(2)], finished in our lab in 2002, is detailed in the next section.

4.2.1 Optical Design of RBS System

The optical component layout and light paths (purple rays) of the binocular RBS system are diagrammed in Figure 4.2. Linearly polarized light emitted by a near-infrared laser diode passes through a lens, which collimates the originally diverged beam. It is then converted to circularly polarized light by a quarter wave plate (QWP) with fast axis 45° to the original plane of polarization. Half of the collimated circularly polarized light is deflected by a non-polarizing beam splitter (NBS), then re-converged by a lens through a clearance hole in a flat, 45° mirror, to fill a spinning concave mirror. This concave mirror is tilted, thus converting the stationary light source to a scanned point of light, which is then directed towards the eyes by the periphery of the 45° mirror with the clearance hole. While each eye is fixating, or focusing, on a blinking red light in the center of the scanning circle, each retina is scanned by the spot of laser light tracing out an annulus subtending 3° of visual angle. A small portion of light is reflected from each ocular fundus and re-imaged by the auto-conjugacy of the ocular system back along the same path it came, until half of the useful returning light passes through the NBS and enters the detection unit, where first the spatially preserved signals from the right and left eyes are separated by a knife-edge reflecting prism. Differential polarization detection, as described previously, is realized for each eye by a polarizing beam splitter (PBS) in combination with paired photodetectors (PD). The polarizing beam splitters separate the light for each eye into horizontally and vertically polarized components, which are then separately converged onto the pair of photodetectors conjugate to the retina. The vertical polarization component is subtracted from the horizontal polarization component, yielding the differential polarization signal, representing the first Stokes parameter of the polarization state of the returning light. This technique of differential polarization detection is exquisitely sensitive to polarization-

related changes, as non-polarized light is equally distributed to both photodetectors and therefore produces no net signal.

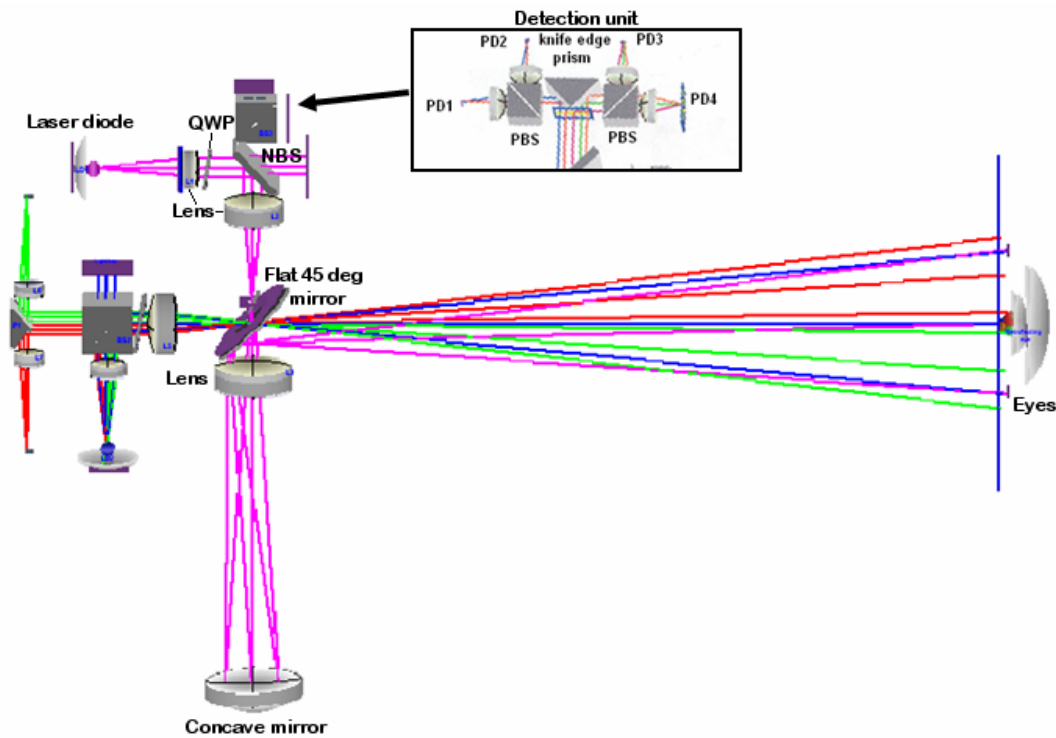


Figure 4.2: Optical component layout with light paths of prototype PVS.

4.2.2 Limitations and Problems

By combining eye fixation and focus technology in a single hand-held device, the prototype of the PVS has shown promise as reliable, automated screening device for the primary causes of amblyopia [Hun04(2)], [Nas04], [Nas07]. However, relatively low signals and high noise limited its overall performance. The main problems with the current design are summarized here.

First, the RBS system for the prototype PVS design used a spinning concave mirror operating off-axis, which introduced astigmatism and distortion into the scanning beam of light, and also added more astigmatism and distortion on the return path, resulting in a double-pass image of the original point of light which was too blurred to be used for reliable focus detection. Second, double-pass lenses created excessive back reflections, thereby significantly contributing to high optical noise.

A major disadvantage of the present design is its opto-electronic complexity. For example, the implemented method of differential polarization detection comprising a polarizing beam splitter in combination with a pair of photodetectors for each eye is sensitive but requires precise alignment and two balanced amplifiers. In addition, the overall RBS signal level varied from one individual to the next, caused by variability and non-uniformity of corneal birefringence across individuals, occasionally masking the desired signal level from retinal birefringence.

Corneal birefringence – the confounding variable

Corneal birefringence is a well-known confounding factor with all polarization-sensitive technology used for retina assessment. Since light must pass through this major birefringent ocular medium before reaching the retina, polarization-related changes caused by the cornea must be dealt with. Separate measurement of corneal birefringence can be made, and then factored out or optically compensated for. The most promising approach involves the application of retarders, because of their ability to influence the polarization state of light and thereby potentially bypass or compensate for different amounts and orientations of corneal birefringence.

Various methods have been proposed in the literature to measure and then optically compensate for corneal birefringence. In the early stages of scanning laser polarimetry/ellipsometry, for instance, contribution of corneal birefringence was extracted from the total retardance measurement by analyzing light coming back from the posterior surface of the crystalline lens. A variable retarder was then set accordingly to cancel out the corneal contribution [Dre94]. Alternatively, light being specularly reflected back from the non-birefringent blood vessels, partially or fully embedded in the retinal nerve fiber layer (RNFL), could be used to determine corneal birefringence [Pel96].

Early commercial scanning laser polarimetry (SLP) systems, such as the GDx NFA and the GDx Access, included a fixed corneal compensator (FCC) with a retardance of 60 nm and a fast axis oriented at 15° nasally downward, based on the corneal properties of an average eye. However, the wide variation of corneal birefringence among individuals, in both its amount and orientation, from the values assumed by the fixed compensator, caused this FCC version of the GDx to fail in a significant portion of the population.

To account for inter- and intra-individual variability, later GDx systems used a variable corneal compensator (VCC), composed of two identical wave plates in rotary mounts, to individually measure and then compensate for eye-specific corneal retardance and azimuth [Zhou02], [Zhou02(2)]. Corneal birefringence is measured with the magnitude of the VCC set to zero, accomplished by simply rotating both retarders such that their fast

axes are perpendicular to each other. Polarimetry images of a normal macula with no pathology obtained in this “crossed” position demonstrates a non-uniform retardation map with a distinct “bow-tie” pattern about the fovea, from whose orientation the corneal azimuth can directly be obtained. Corneal retardance is determined from the retardation profile along a circle centered on the fovea. This “bow-tie” method is described in more detail in 6.1.3. Another method (“screen” method) is incorporated in the GDx-VCC for corneal birefringence measurement of eyes with macular disease or a severely damaged Henle fiber layer [Kni02(2)], based on an averaging procedure over a large square area of the macula centered on the fixation point [Zho06]. Once the individual corneal birefringence is known, eye-specific corneal compensation is achieved by first counter-rotating both retarders so that their combined retardance matches the measured amount of corneal birefringence, and then rotating them together so that the slow axis of the retarder combination is perpendicular to the measured slow axis of corneal birefringence.

Recent studies have shown that in some eyes an atypical retardance pattern is apparent on images obtained with the GDx-VCC, more frequently in eyes with light pigmentation, in myopic eyes, and in eyes of elderly subjects. The source of this aberrant retardance is unknown, but is thought to be caused by an insufficient signal-to-noise ratio [Bow07]. To improve the signal-to-noise ratio, a new software method was recently developed that provides enhanced corneal compensation (ECC) without requiring any hardware modification to the GDx-VCC [Reu06]. Rather than being adjusted to neutralize the corneal birefringence, in the ECC mode the variable corneal compensator is adjusted so that combined with the measured corneal retardance of the specific eye a total retardance of 55 nm is produced with an overall slow axis close to vertical. This “bias” retarder superimposes the RNFL birefringence onto a large known birefringence and thereby shifts the retardation measurement into a more sensitive region, where the measurement is less susceptible to optical and electronic noise, as occurs when the corneal retardance is low. The birefringence introduced by the bias retarder is then determined from the macular region using the “screen” method, and RNFL retardation is then mathematically extracted from the measurement [Zho06].

While effective for its intended purposes, these compensating methods involve a separate measurement and feedback system, an approach that is tedious and not feasible in poorly cooperative children. The advantage of our technique of foveal fixation assessment is the large exit pupil that allows relative freedom of alignment without the need to stabilize the subject’s head, thereby enabling assessment in a freely moving child. However, the azimuth of the corneal birefringence can change constantly during a recording with a moving child, so that a method of bypassing rather than compensating for

the corneal birefringence is desired, especially in an application that is geared towards children.

4.2.3 Hypotheses and Objectives

The hypotheses of this investigation are that **(1)** by adding a spinning double-pass half wave plate (HWP) to the optical system, differential polarization detection of foveal fixation can be realized with only half as many detectors, easing constraints on optical alignment and electronic balancing. The orthogonal polarization states are measured at different points in time, more precisely on alternate scans, rather than simultaneously, and the differential RBS signal is calculated digitally by first shifting the acquired signal by one period and then subtracting it from itself. If spun at a fractional frequency of the scan, the RBS signal can be modulated so that a strong “multiple of half” frequency component is generated, which will double in amplitude whereas repetitive noise at the scanning frequency will be eliminated with differential phase-shift subtraction; **(2)** in combination with a fixed double-pass retarder it may be possible to use only the modulation produced by the spinning half wave plate to detect the needed RBS signals essentially independently of various amounts and orientations of corneal birefringence.

The objectives of this investigation are to develop a computer model based on Müller-Stokes matrix calculus in MATLAB to test these hypotheses theoretically and optimize the properties of both wave plates to statistically maximize RBS signal strength, while having the greatest independence from left and right eye corneal birefringence, thereby improving recognition of foveal fixation by exploiting retinal birefringence. This RBS model will be validated experimentally using an intermediate monocular eye fixation monitor, developed using plane mirrors for the scanning system, avoiding optical degradation of the double-pass image. An improved PVS design will be described, measuring binocular foveal fixation essentially independently of corneal birefringence, with the primary objective to provide effective and appropriate screening instrumentation to automatically identify infants and young children at risk for amblyopia.

Chapter 5

Spinning Half Wave Plate Design for RBS

Recall that a half wave plate rotates the axis of linear polarization by twice the angle between the retarder's fast axis and the input plane of polarization. With its fast axis oriented 45° to the original plane of polarization, the half wave plate allows conversion from one orthogonal polarization state to the other. Due to this interesting property of polarization rotation, a spinning HWP, continuously changing the polarization orientation, enables essential measurement of the two orthogonal polarization states with the same photodetector at different points in time, thereby avoiding errors associated with gain mismatch in the simultaneous measurement with a dual photodetector system.

The usefulness of applying rotating wave plates to measure polarization characteristics with only one detector has been demonstrated in several polarimetric applications [Wil99], [Ach03], [Gol92], with Fourier ellipsometry probably being the most prominent example. The original Fourier ellipsometer, as described by Hauge and Dill [Hau75], [Dil77], uses a rotating quarter wave plate and a fixed analyzer to measure the Stokes parameters with a single detector. Stokes parameters are extracted from the Fourier analysis of the detected periodic signal.

Due to the large exit pupil (typically 40 x 40 mm) overfilling the entire pupil of the eye, our method of foveal fixation assessment allows investigations in a freely moving child. However, at the same time, the large exit pupil allows a considerable amount of light (which upon diffuse reflection is largely depolarized) to be reflected back from sources such as the face, lids, and sclera, significantly contributing to high optical noise. The previously applied differential polarization detector comprising a polarizing beam splitter and two photodetectors had the great advantage of nulling out those sources of optical noise, as depolarized light is equally distributed to both detectors.

We therefore need a method with the spinning wave plate and single polarization detector solution to eliminate optical noise caused by depolarized light that is reflected back into the system from skin, etc. Furthermore, as we are interested in the polarization-related changes, a method of rejecting unchanged polarized light is also required. The latter can be achieved by using a polarizing beam splitter (PBS) to block unchanged polarized light from reaching the detector. A simplified diagram of the spinning-wave-plate RBS design is shown in Figure 5.1.

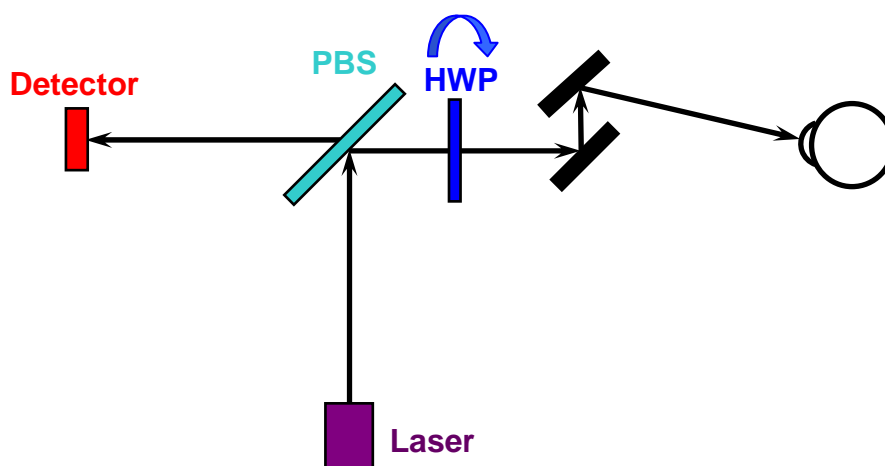


Figure 5.1: Simplified diagram of spinning-half-wave-plate RBS design. Linearly polarized light emitted by a laser diode, with axis of polarization perpendicular to the plane of the diagram, is reflected by a polarizing beam splitter (PBS) towards the eye. After the PBS, the beam passes through the spinning half wave plate (HWP) and enters the scanner, consisting of two plane mirrors that are spun by a motor (not shown), creating a circular scan on the subject's retina. On the return pass, the PBS separates the polarization-altered light into two orthogonally polarized components. The polarization component in the plane of the diagram is transmitted to the detector, whereas the polarization component perpendicular to the plane of the diagram is reflected back to the laser, never making it to the detector.

5.1 Phase-Shift Subtraction Technique

Due to the strict radial symmetry of the Henle fibers about the fovea, retinal birefringence on its own causes the polarization state of stationary polarized light to change at “whole multiples” of the frequency of the circular scan, such as at twice the scanning frequency as

described before. By spinning the HWP at a specific fractional frequency of the scan, however, the axis of polarization of the impinging light can be continuously rotated in order to modulate the polarization-related changes arising from the retina so that they occur at a “multiple of half” frequency of the scan after double-passing through the radial array of Henle fiber birefringence. The light that has been depolarized by reflection from the skin and sclera is not affected by the spinning wave plate, so that the signal from the resulting optical noise still repeats over a single scanning cycle.

If a copy of the acquired signal, that is, the modulated RBS signal repeating at “multiple of half” frequencies of the scan frequency, is digitally shifted by one period and then subtracted from the original signal (360° -phase-shift subtraction), differential polarization detection is achieved with the differential polarization signal being double in amplitude. This is because on alternate scans each “multiple of half” frequency signal is 180° out of phase with itself, and when the two signals are subtracted, a double-amplitude signal is obtained (illustrated in Figure 5.2).

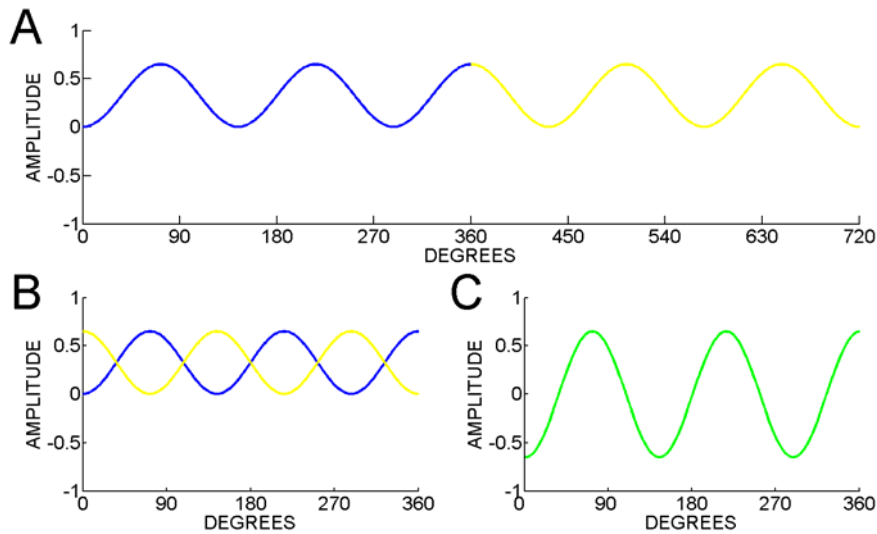


Figure 5.2: General concept of calculating the differential polarization signal. **A.** Example of a “multiple of half” frequency signal, with the blue and yellow trace representing the first and second scan cycles respectively. **B.** The “multiple of half” frequency signal from A is shifted by one period. Note that the two waveforms are π radians, or 180° , out of phase, so that if the second cycle is subtracted from the first (blue tracing minus yellow tracing), the resultant signal will have twice the amplitude. **C.** Differential signal with double amplitude after 360° -phase-shift subtraction.

Any repetitive signal at the scan frequency, such as much of the background noise, or at whole multiples of the scan frequency, will subtract out with 360° -phase-shift subtraction, because each “whole-number” frequency signal will be in phase with itself when shifted 360° on top of itself.

Somewhat similar approaches to noise removal, involving generation of phase-shifted signals, have been suggested in other applications. In U.S. Patent No. 7,266,062 B2, for instance, Kurihara describes a noise removal circuit for the purpose of noise reduction in signal recording and reproduction applications [Kur07]. One suggested method comprises a 180° phase shifting circuit to generate a signal that is phase-shifted from an input signal by an odd multiple of 180 degrees from an input signal. Noise is eliminated by subtracting the 180° -shifted signal from the input signal.

5.2 Modeling of RBS Using Wave Plates

To optimize the settings of the spinning half wave plate RBS design, such as the rotation frequency of the HWP as well as the retardance and fast axis orientation of the fixed double-pass wave plate, an intimate knowledge of corneal interference in retinal birefringence scanning is needed, as the measurement of polarization-related changes induced by the retina in light retroreflected from the ocular fundus is adversely affected by corneal birefringence varying from one eye to the next, thus creating variability in the RBS signal level between eyes and subjects. Because we rely upon the subtle changes caused by the retinal birefringence, a design that makes RBS as immune as possible to different amounts and orientations of corneal birefringence is needed.

To achieve a better understanding of the influence of corneal birefringence on the detected RBS signals, a computer model has been developed in MATLAB based on a previously developed mathematical model [Hun99(2)]. The model mathematically describes retinal birefringence scanning in a double-pass system using Müller-Stokes matrix calculus. With its help, different options for the RBS design can be simulated to find a setting that will allow foveal fixation detection essentially independently of the various amounts and orientations of corneal birefringence that occur in the population.

5.2.1 Model of Ocular Birefringence

In the eye, every component is characterized by its own Müller matrix, with the cornea and retina considered simply as birefringent media that affect the polarization state of the

transmitted light. Because the contribution of the crystalline lens is negligible, it is not included in the model. The double pass into and back out of the eye can thus be described mathematically by multiplying the Stokes vector of the incident light by the respective Müller matrices for each contributing ocular medium in sequence, i.e. the cornea, retina, reflection from the ocular fundus, retina again, and cornea again.

$$\vec{S}_{out} = \mathbf{M}_{cornea(out)} \cdot \mathbf{M}_{retina(out)} \cdot \mathbf{M}_{fundus} \cdot \mathbf{M}_{retina(in)} \cdot \mathbf{M}_{cornea(in)} \cdot \vec{S}_{in} \quad (5.1)$$

The input Stokes vector, \vec{S}_{in} , representing the incident state of polarization is first multiplied by the Müller matrix of the cornea, $\mathbf{M}_{cornea(in)}$. The transmitted Stokes vector is subsequently multiplied by another Müller matrix, $\mathbf{M}_{retina(in)}$, characterizing retinal retardance. The next Müller matrix multiplication represents the reflection from the ocular fundus (\mathbf{M}_{fundus}). As the reflected beam passes both cornea and retina once again, there are two more transformations necessary, representing the second pass through the corneal and retinal birefringence, $\mathbf{M}_{cornea(out)}$ and $\mathbf{M}_{retina(out)}$, respectively. The outgoing Stokes vector, \vec{S}_{out} , determines the final polarization state.

Reflection from the ocular fundus

Reflection from the ocular fundus exhibits a high degree of polarization preservation [Dre92]. The fundus is therefore treated as a complete polarization-preserving ideal reflector in the model.

The Müller matrix of a generalized mirror is as follows:

$$\mathbf{M}_m = \begin{pmatrix} \frac{r+1}{2} & \frac{r-1}{2} & 0 & 0 \\ \frac{r-1}{2} & \frac{r+1}{2} & 0 & 0 \\ 0 & 0 & \sqrt{r} \cos(\delta) & \sqrt{r} \sin(\delta) \\ 0 & 0 & -\sqrt{r} \sin(\delta) & \sqrt{r} \cos(\delta) \end{pmatrix} \quad (5.2)$$

By assuming ideal reflectance from the retina, i.e. $r = 1$, and a retardance $\delta = 180^\circ$ [Sco04], the Müller matrix for the ideal retinal mirror becomes:

$$\mathbf{M}_{fundus} = \begin{pmatrix} 1 & 0 & 0 & 0 \\ 0 & 1 & 0 & 0 \\ 0 & 0 & -1 & 0 \\ 0 & 0 & 0 & -1 \end{pmatrix} \quad (5.3)$$

As can be seen, the reflection from the fundus simply reverses signs of the third and fourth Stokes parameter, S_2 and S_3 , while the second parameter, S_1 , remains unchanged.

It is important to understand that in equation (5.1) the first- and second-pass Müller matrices differ in orientation as a consequence of S_2 and S_3 changing sign with reflection. The azimuth of $\mathbf{M}_{retina(out)}$ thus has the reverse sign with respect to $\mathbf{M}_{retina(in)}$. The same applies to both matrices representing corneal birefringence.

Foveal birefringence

The Henle fiber layer is modeled as a radially symmetric birefringent medium, with every fiber acting as linear retarder, mathematically described by equation (3.19). Each fiber of the radially arrayed Henle fiber layer is assumed to have the same amount of birefringence with its slow axis aligned with the orientation of the fiber. The azimuth of the fast axis, therefore, is perpendicular to the orientation of the fiber. As polarized light is scanned around the fovea in an annular pattern, the azimuth of foveal birefringence depends on the orientation of the fibers at the current scanning position. During simulated central fixation, fiber orientation and scanning angle are identical, thus the azimuth of foveal birefringence is rotating through 360 degrees. During paracentral fixation, however, the orientation of the fiber encountered at the momentary scanning position is a function of the point of fixation:

$$\theta_{fiber} = \tan^{-1} \left(\frac{R \sin(\phi) + y_{ret}}{R \cos(\phi) + x_{ret}} \right) \quad (5.4)$$

where ϕ is the momentary scanning position, advancing through 360°, and x_{ret} and y_{ret} are the horizontal and vertical displacements of the center of the scanning circle from the fovea respectively. A pictorial derivation of equation 5.4 is provided in Figure 5.3 below.

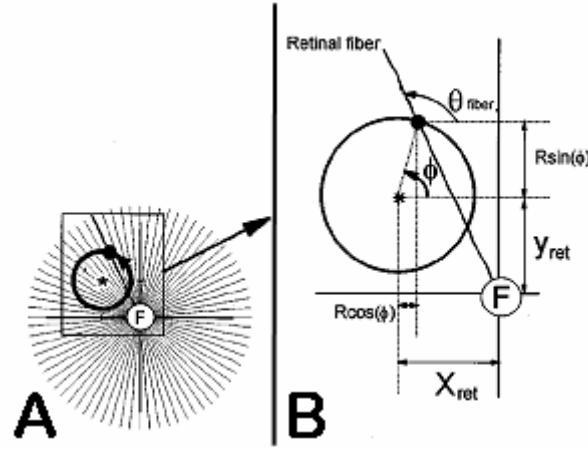


Figure 5.3: Calculation of fiber orientation encountered at the momentary scanning position during paracentral fixation. **A.** With the eye not fixating properly, the scan is decentered from the fovea (F). **B.** The corresponding fiber orientation (θ_{fiber}) at the momentary scanning position (Φ) can be obtained from basic trigonometric relations. Modified from [Hun99(2)].

The fast axis of the foveal birefringence (θ_r), being perpendicular to the fiber orientation, can thus be calculated as follows:

$$\theta_r = \tan^{-1} \left(\frac{R \sin(\phi) + y_{ret}}{R \cos(\phi) + x_{ret}} \right) + 90^\circ \quad (5.5)$$

The amount of retinal retardance (δ_r), on the other hand, depends on the distance from the foveal center. In the RBS computer model, the maximum retardance is considered to be 15 nm [kle88], [Blo85], increasing from zero in the very center to the maximum of 15 nm ~ 1.5 degrees from the center, and then tapering off farther from the center. This attenuation away from the center is described by [Gra06]:

$$\delta_r = \left(\prod_{i=1}^2 e^{-\frac{r}{\tau_i}} \right) \left(\prod_{i=3}^5 \left(1 - e^{-\frac{r}{\tau_i}} \right) \right) \quad (5.6)$$

where $\tau_1 = 3.7$, $\tau_2 = 50$, $\tau_3 = 0.6$, $\tau_4 = 5$, $\tau_5 = 0.8$. These exponents yielded the best fit to the foveal retardance profile, shown in Figure 5.4 which has been derived from previous measurements in our laboratory [Gra06], [Pat95].

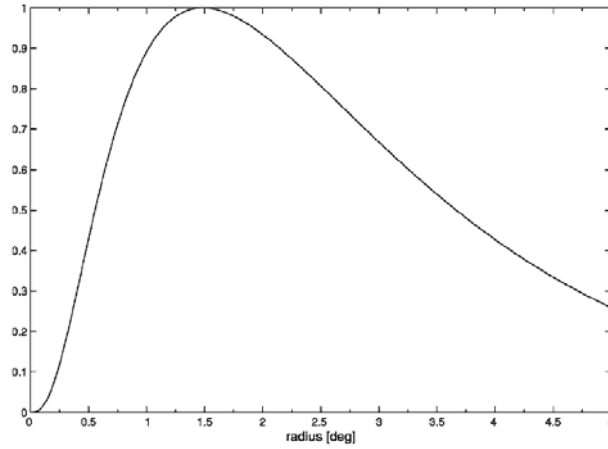


Figure 5.4: Foveal birefringence as a function of the distance from the foveal center [Gra06].

With central fixation, the 3° annulus of light is centered on the radial array of linear retarders, so that the same amount of retinal birefringence, i.e. retinal retardance, is experienced at each scanning position. Thus, given that the eye is fixating properly, the circular scan on the retina can be thought of as a spinning wave plate with a retardance of 15 nm, rotating at the frequency of the scan. For an operating wavelength of 785 nm, as used in our applications, 15 nm corresponds to a phase shift of about 7° . The consideration of the retina as a rotating 7° wave plate provides a simple approach to explain the “whole-number” frequency components in the RBS signal by means of the Müller-Stokes matrix calculus, in addition to the purely intuitive explanation from Chapter 4.

First, the double pass of light through the retinal birefringence can be visually represented with the help of the Poincaré sphere, as follows (Figure 5.5). Assume that LVP light is incident on the retina, represented by the red dot at the back of the sphere. As the spot of light scans a circle around the fovea, the eigenvector of foveal birefringence, situated in the equatorial plane, is spinning twice around the sphere’s origin. If the scan begins at 9 o’clock, when looking at the retina, and progresses in a clockwise direction, the fast axis of retinal birefringence, being perpendicular to the fiber orientation, changes from 90° through 360° to 90° during one revolution of the scan. The state of polarization, rotating around the foveal eigenvector at each fiber orientation by an angle equal to the amount of retinal retardance, that is about 7° in the case of central fixation, consequently varies over time, resulting in a twice-traced path of polarization states instead of a single point. In this particular case of incident linearly polarized light, one complete rotation through 180° , in other words half a rotation of the “ 7° wave plate”, leads to a generated path of polarization states in the form of a figure-of-eight. The subsequent reflection from

the ocular fundus causes each polarization state and each eigenvector to rotate 180° about the S1 axis. The second passage through the retina increases the size of the previously generated figure-of-eight path.

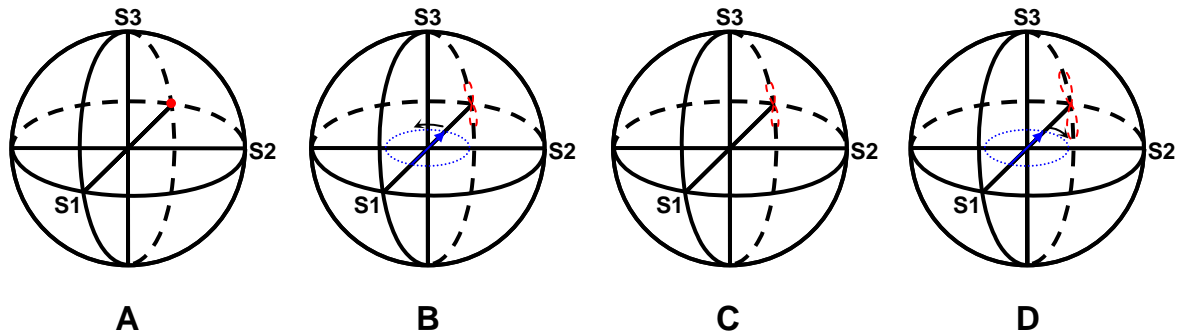


Figure 5.5: Changes in the state of polarization during the double pass of light through foveal birefringence represented with Poincaré analysis (corneal birefringence neglected).

A. Initial polarization state: LVP, i.e. $\vec{S}_{in} = (1, -1, 0, 0)^T$. **B.** First pass through retina. **C.** Reflection from fundus. **D.** Second pass through retina.

The differential polarization signal measured by the pair of photodetectors can be considered identical to the projection of the final path of polarization states onto the S1 axis, which represents Stokes parameter S_1 . As can be understood from the projection of the final polarization state onto the S1-S3 plane (Figure 5.6 A center), the polarization state moves both above and below the equator, twice each during each scan, so that each maximum and minimum measured along S3 (Figure 5.6 B left) becomes a maximum when measured along S1 (Figure 5.6 B center). Thus, the differential polarization signal (S_1) shows a predominant frequency component that is 4 times the scanning frequency ($4f$). The maximum signal levels occur at 45° , 135° , 225° , and 315° , that is, whenever the azimuth of the incident linear polarization is 45 degrees to the nerve fiber orientation (Figure 5.7).

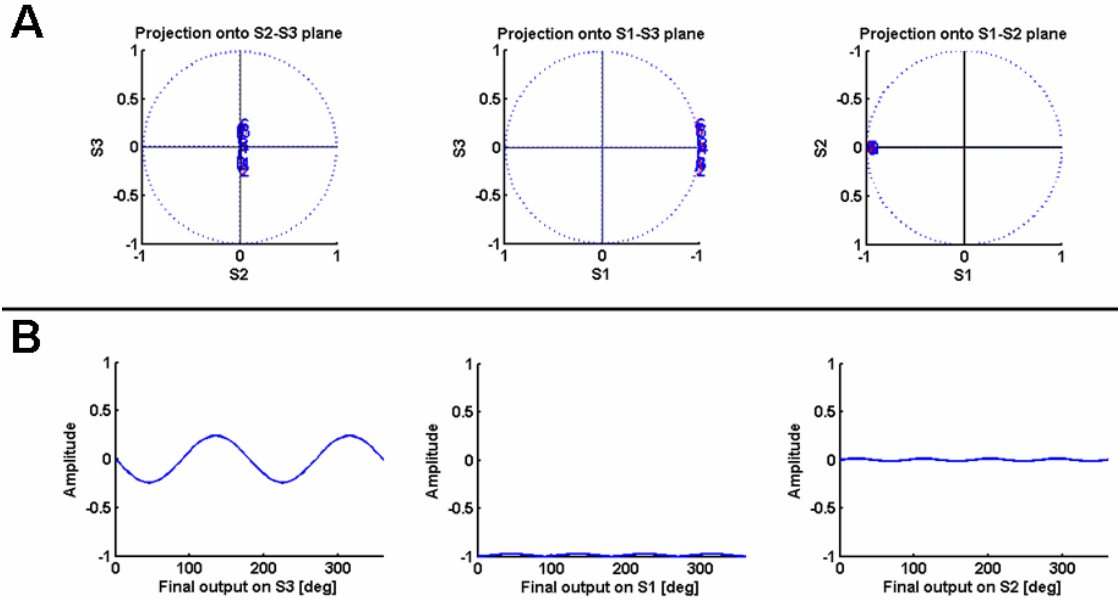


Figure 5.6: **A.** Projection of the final polarization state, after double pass through retinal birefringence, onto the S2-S3, S1-S3, and S1-S2 planes, (corneal birefringence neglected). **B.** Final output projected onto the S3, S1, and S2 axes.

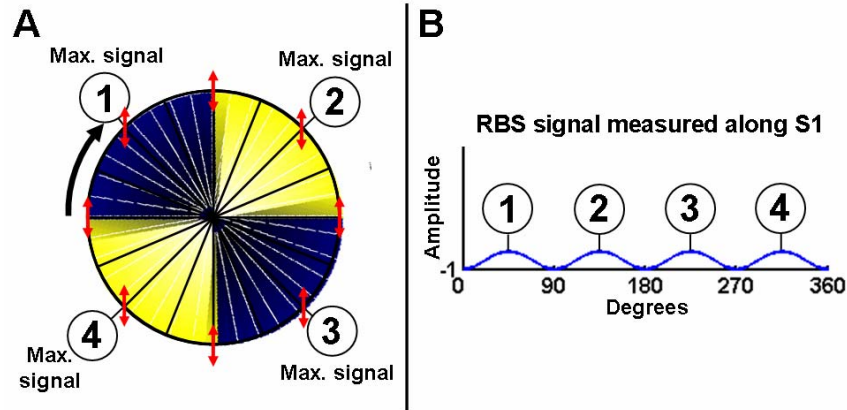


Figure 5.7: **A.** Circular scan on retina with central fixation (corneal birefringence neglected). Maximal signal points occur whenever the azimuth of the linearly polarized light (red double sided arrow) incident on the radially arrayed Henle fibers is 45 degrees to the orientation of the nerve fibers. **B.** RBS signal measured along S1. Henle-fiber-induced changes in light reflected from the ocular fundus repeat 4 times during each 360° scan.

A differential polarization signal that is proportional to the Stokes parameter S_3 , therefore showing a strong double frequency component ($2f$), is obtained if a quarter wave plate is included in the setup. Most of our previous applications employed a quarter wave plate in the RBS design with the fast axis orientated 45° to the original plane of linear polarization, either in the input, producing circularly polarized light incident on the eye [Hun03], [Hun04(2)], or in the output right before the differential polarization detector [Ago08], flipping the generated path of polarization states near the equator onto the north pole of the sphere, so that the circular polarization component in the returning light was measured (as Stokes parameter S_3) along the S_1 axis by the differential polarization detector. Referring to Figures 5.5 and 5.6, it becomes readily visible that a rotation about the S_2 axis, which is the axis of rotation given that the quarter wave plate is oriented 45° away from incident LVP light, exchanges the projection of the final polarization states on S_1 and S_3 , while the final output on S_2 remains unchanged.

Second, considering the retinal scan as a rotating 7° wave plate allows a simplified theoretical derivation of the presence of the quadruple frequency term in the differential polarization S_1 signal. The outgoing Stokes vector, determining the final polarization state after double-passing through retinal birefringence, may therefore be obtained by the following serial multiplication of Müller matrices:

$$\vec{S}_{out} = \mathbf{M}_{7^\circ WP(out)} \cdot \mathbf{M}_{fundus} \cdot \mathbf{M}_{7^\circ WP(in)} \cdot \vec{S}_{in} \quad (5.7)$$

where

$$\mathbf{M}_{7^\circ WP(in)} = \begin{pmatrix} 1 & 0 & 0 & 0 \\ 0 & \cos^2 2\theta + \cos(7^\circ) \sin^2 2\theta & (1 - \cos(7^\circ)) \cos 2\theta & \sin(7^\circ) \sin 2\theta \\ 0 & (1 - \cos(7^\circ)) \sin 2\theta \cos 2\theta & \sin^2 2\theta + \cos(7^\circ) \cos^2 2\theta & -\sin(7^\circ) \cos 2\theta \\ 0 & -\sin(7^\circ) \sin 2\theta & \sin(7^\circ) \cos 2\theta & \cos(7^\circ) \end{pmatrix},$$

$$\mathbf{M}_{7^\circ WP(out)} = \mathbf{M}_{7^\circ WP(in)}(7^\circ, -\theta), \quad \theta = \omega t \quad (5.8)$$

Carrying out the matrix multiplication and solving for the first Stokes parameter results in:

$$\begin{aligned} S_1 = & [(-\cos^2 2\theta + \cos(7^\circ) \sin^2 2\theta) \cdot (\cos^2 2(-\theta) + \cos(7^\circ) \sin^2 2(-\theta))] + \dots \\ & + [((1 - \cos(7^\circ)) \sin 2\theta \cos 2\theta) \cdot ((1 - \cos(7^\circ)) \cos 2(-\theta))] + \dots \\ & + [(\sin(7^\circ) \sin 2\theta) \cdot (\sin(7^\circ) \sin 2(-\theta))] \end{aligned} \quad (5.9)$$

As can be seen

$$S_1 \propto \cos^4 2\theta + \sin^4 2\theta + \dots \quad (5.10)$$

Using the power-reduction formulas

$$\cos^4 \theta = \frac{3 + 4 \cos 2\theta + \cos 4\theta}{8}, \quad \sin^4 \theta = \frac{3 - 4 \cos 2\theta + \cos 4\theta}{8} \quad (5.11)$$

which can be derived from the trigonometric double-angle formulas, the quadruple frequency term becomes readily visible.

In the RBS computer model, the retina is scanned 16 times in total, in incremental steps of 4.5° , thus leading to 1280 calculations. Each of the resulting S_1 , S_2 , and S_3 signals is Fourier analyzed to determine the relevant frequencies of interest. More precisely the Fast Fourier Transform (FFT) is computed on the whole 16-cycle epoch and the power spectrum of the S_1 , S_2 , and S_3 signals in the frequency domain is determined.

Remember that the above consideration was made while neglecting corneal birefringence, the major contributor to ocular birefringence and the major confounding variable in retinal birefringence scanning. The double pass through corneal birefringence in general causes the final path of polarization states to deviate from the equator, such that the the double frequency signal dominates in the differential polarization recording rather than the quadruple frequency signal.

Corneal birefringence

In general, the cornea should be treated as a biaxial crystal with one optic axis perpendicular to the corneal surface and another optic axis parallel to the corneal surface [van87]. In all the applications using retinal birefringence scanning, however, only light passing through the entrance pupil is of interest, where corneal retardance is essentially constant. Therefore the cornea is modeled as a uniform linear retarder (Equation (3.19)), specified by a certain retardance (CR) and azimuth (CA). The latter is simply the orientation of the fast axis. Since the slow axis on average tends to be oriented nasally downward in the population [van87], the fast axis, being perpendicular to the slow axis, is thus nasally inward from vertical.

To provide an example of the effects of corneal birefringence on the generated path of polarization states, let us assume a human eye with a corneal retardance of 30 nm ($\sim 14^\circ$

for an operating wavelength of 785 nm) and an azimuth of 110° , a typical example of a left eye. Referring to the Poincaré sphere presentation from above (Figure 5.5), including this eye-specific corneal birefringence, the double pass of initially vertically oriented polarized light ($S_1 = -1$) through ocular birefringence can be visualized as follows (Figure 5.8). The eigenvector of corneal birefringence is located in the equatorial plane, oriented at 220° , which corresponds to twice the value of CA. The first pass through the cornea, represented by the turquoise curved arrow, thus causes clockwise rotation through 14° (CR) about the corneal eigenvector, away from the equator. Therefore, instead of being in the form of a figure-of-eight, as is the case if the transmitted polarization state of the incident light lies on the equator before encountering the retina, the twice-traced path of polarization states is in form of an ellipse after passing through retinal birefringence. With reflection from the ocular fundus, this ellipse of polarization states is rotated 180° about the S_1 axis, and is enlarged in size as the light proceeds through the retina on its second pass. Finally, the second pass through the cornea causes the entire ellipse to rotate about -220° (CA) through 14° (CR). From the projection of the elliptical path of polarization states on the S_1 , S_2 , and S_3 axes, it becomes obvious that a double frequency term dominates in each signal (Figure 5.9).

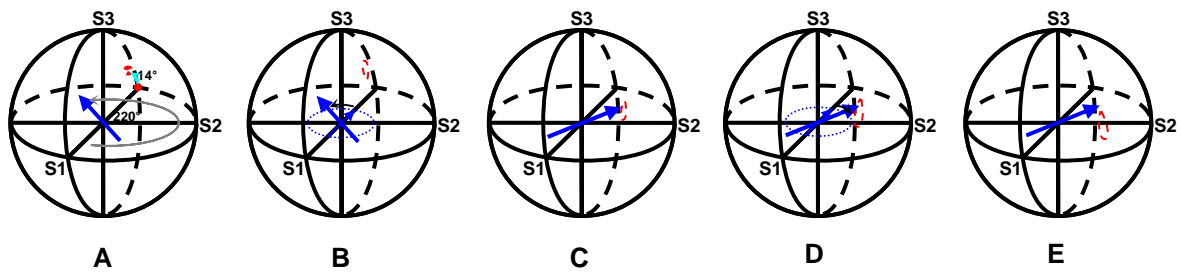


Figure 5.8: Changes in the state of polarization during the double pass of LVP light through ocular birefringence represented with Poincaré analysis. **A.** First pass through cornea. **B.** First pass through retina. **C.** Reflection from fundus. **D.** Second pass through retina. **E.** Second pass through cornea.

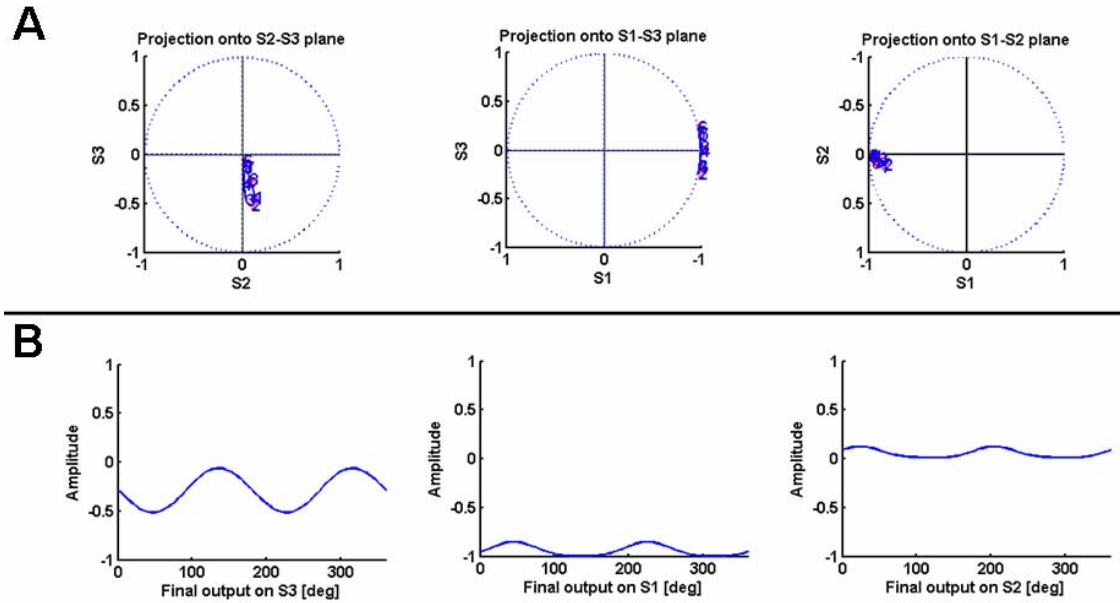


Figure 5.9: **A.** Projection of the final polarization state, after double pass through ocular birefringence, onto the S2-S3, S1-S3, and S1-S2 planes. **B.** Final output on the S3, S1, and S2 axes.

5.2.2 Assessing the Influence of Corneal Birefringence on the RBS Signal

Both corneal retardance and azimuth vary from one eye to the next but are reasonably constant over the entrance pupil for any given eye. To consider the different values for CR and CA that occur in the population, the 70 eyes from the data published by Knighton and Huang have been used as a reference [Kni02]. Within the scope of their studies, normal subjects were measured to determine the birefringence properties of their central corneas. Their measurements led to an average corneal azimuth (CA) of 110 degrees for left eyes and 70 degrees for right eyes respectively. The mean value for corneal retardance (CR) was 30 nm. Five additional pairs of CR and CA were included in the assessment, obtained from measurements in our laboratory [Gra06]. As corneal azimuths are in general well correlated between the two eyes, we included the mirror image of each eye (mirrored about the axis of symmetry, i.e. 90° CA) in the assessment, yielding a total number of 300 representative pairs of CR/CA. In the further course of this work, the data of these 300 eyes is referred to as the Knighton/Gramatikov data set.

We have sought to find an RBS design that yields the largest RBS signal (S_1 signal) practically constant over the population range of corneal retardances and azimuths. In addition to modeling the effects of ocular birefringence as described above, the RBS computer program provides the user with a means to select diverse optical components and to specify their properties in the double-pass scanning system. These manipulations can alter the polarization state of light in various ways before and after passing through the eye in order to optimize the power throughput. For instance, additional wave plates can be optionally placed in the light path, single-pass or double-pass (operating in either the incoming path or in the return path or in both), rotating or fixed, as well as beam splitters, etc. With the help of the Knighton/Gramatikov data set, it was possible to judge if a certain RBS design would fail or excel in a significant proportion of the population (further explained below).

For a given optical arrangement, the MATLAB computer program determines the predominant frequencies in the RBS signal, and then computes the FFT power spectrum values at the frequency of interest for a range of CR and CA combinations (0 to 180 nm CR, and 0 to 180° CA) to cover the variability of corneal birefringence across individuals. These signal strengths (FFT power) at a given frequency are displayed as a function of CR and CA over the entire ranges of these variables (Figure 5.10). Superimposed on the surface of this 3D-plot are the specific pairs of CR and CA of the Knighton/Gramatikov data set, so that it is readily visible how the optical setup would perform in a representative group of people. Right eyes are indicated as circles and left eyes as crosses. In the best case, the surface of the 3D-plot should be flat and high according to the requirements of greatest independence from corneal birefringence. The contour plot, which is generated simultaneously with the 3D-plot, provides another means of judgment about the suitability of a design. This contour plot is simply a flat graph with axes CA and CR, showing in the background the corneal retardance and azimuth of each of the right and left eyes in the Knighton/Gramatikov data set, upon which is composed a contour plot of the signal strength showing where the signal drops down, in other words which eyes are “missed” when the signal falls below the threshold of 0.4, which has been arbitrarily considered as a measurement failure (Figure 5.11).

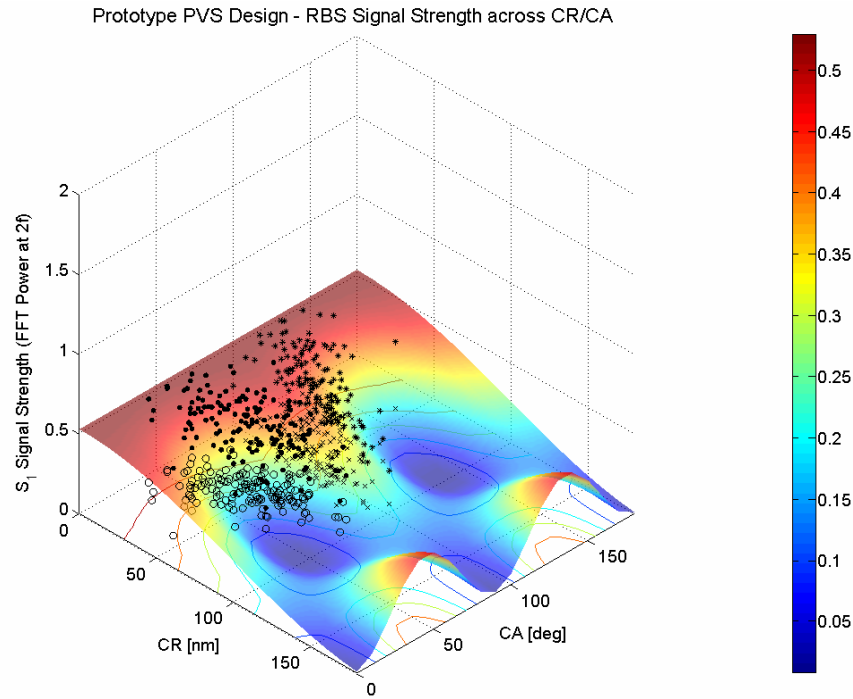


Figure 5.10: RBS signal strength in relative power units as a function of corneal retardance (CR) and corneal azimuth (CA) with model of the prototype PVS.

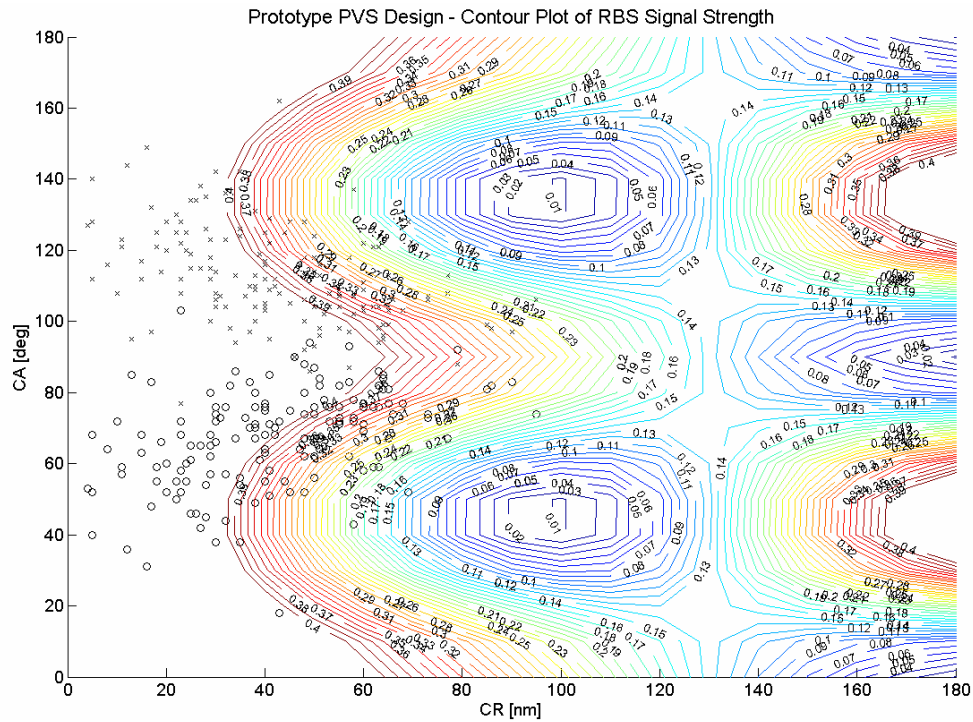


Figure 5.11: Contour plot of RBS signal strength in relative power units as a function of corneal retardance (CR) and corneal azimuth (CA) with model of the prototype PVS.

The representative figures above are the predicted results with the RBS design implemented in the prototype PVS, modeled with a single-pass quarter wave plate and a double-pass 50/50 non-polarizing beam splitter. As can be seen, the RBS signal obtained with this setup is very low and by no means independent of corneal birefringence. As shown in Figure 5.11, 130 of the eyes fall below the “0.4” contour. In other words, with this threshold setting, 43% of the human eyes in the Knighton/Gramatikov data set fail with the prototype PVS design. Only weak signals are measured for eyes in the range where the signal strength drops below this threshold of 0.4.

Initially many different designs were tested geared towards bypassing the deleterious effects of corneal birefringence in retinal birefringence scanning. Eventually a spinning half wave plate was added in the RBS design to enable differential detection of the RBS signal with only one detector, thus avoiding precise alignment requirements and the excessive electronics required by fixed differential polarization detectors. It later became apparent that adding a fixed double-pass wave plate to the scanning system had the most potential for making RBS as immune as possible to the inter- and intra-subject variability of corneal birefringence (further explanation below).

5.2.3 Determination of Optimum Spinning Frequency of Double-Pass HWP

“Multiple of half” frequency signals are needed to calculate the differential polarization signal. To generate “multiple of half” frequency RBS signals that will double in amplitude and even quadruple in FFT power (being the FFT magnitudes squared) with 360°-phase-shift subtraction, the half wave plate has to be spun at a fractional frequency of the scan, more precisely at an odd multiple of 1/16 as fast as the scanning frequency:

$$f_{HWP} = (2n + 1) \cdot \frac{f}{16} \quad (5.12)$$

where $n = 0, 1, 2, \dots$, so that the rotation speed of the HWP will be $f_{HWP} = 1/16 f, 3/16 f, 5/16 f$, etc.

This can be derived intuitively by the following simplified consideration. The key point in understanding is that the HWP rotates the polarization state twice as fast as it spins itself. Recall that if corneal birefringence is neglected, the retinal-nerve-fiber-induced changes in light reflected from the fundus of the eye repeat 4 times during each 360° scan, yielding a strong frequency component in the RBS signal of exactly 4 times the scanning

frequency ($4f$). Maximum signal levels occur whenever the azimuth of the linearly polarized incident light is 45 degrees to the orientation of the nerve fibers, whereas minima occur when the axis of polarization is perpendicular or parallel to the fiber orientation (Figure 5.7). If a HWP spinning $1/16$ as fast as the circular scan is added between the source of linearly vertical polarized light and the retina, the azimuth of linear polarization, beginning at 90° , incident on the Henle fibers is continuously changing in the same direction as the fiber orientation. Suppose when looking at the retina, the scan starts at 9 o'clock and progresses in a clockwise direction (Figure 5.12 A). During one revolution of the scan, the fast axis of the HWP rotates $1/16$ of 360° , from 0° to 22.5° , causing the incident polarization axis to rotate twice the angle of HWP rotation, a total of 45° , that is from azimuth 90° to azimuth 135° (red double-ended arrows). With the HWP spinning, the axis of the incident linear polarization (red double-ended arrows) is continuously changing, but lagging behind the fiber's orientation in case of a $1/16$ rotation speed, the locations at which Henle fibers and polarization orientation are perpendicular, parallel, or aligned 45 degrees occur later (at higher azimuths) compared with the case when there is no rotating HWP in the setup and therefore a constant polarization state striking each fiber orientation (Figure 5.12 B). Consequently, the maximal and minimal signal points have been shifted, changing the frequency of the signal on S_1 , from $4f$ to $3.5f$. After the first scanning cycle, the axis of the incident linear polarization is exactly 45 degrees to the nerve fiber orientation, resulting in a maximal S_1 signal level. This applies to any HWP rotation speed that is an odd multiple of $1/16$ of the scanning frequency. As the axis of linear polarization incident on the Henle fibers rotates twice as much as the HWP during each scan, the angle at the end of the first scanning cycle between the axis of incident linear polarization and the fiber orientation is always an odd multiple of 45 degrees:

$$2 \cdot (2n+1) \cdot \frac{360^\circ}{16} = (2n+1) \cdot \frac{360^\circ}{8} = (2n+1) \cdot 45^\circ \quad (5.13)$$

yielding a maximum in the RBS signal.

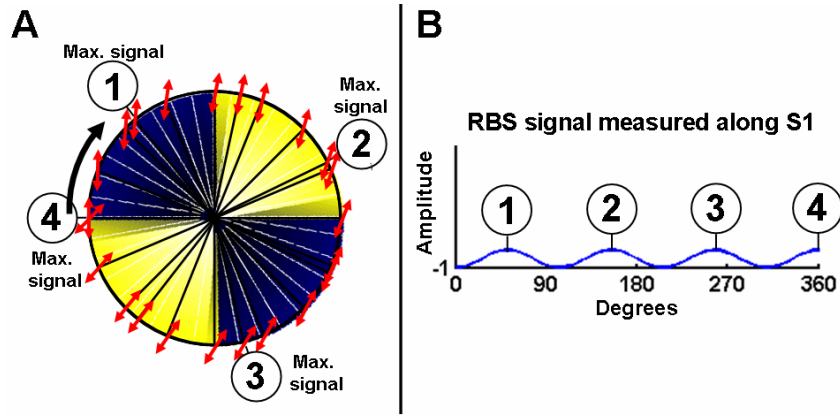


Figure 5.12: Generation of “multiple of half” frequency foveal fixation signals by means of a HWP spinning at odd multiples of 1/16 of the scan frequency. **A.** With the HWP spinning, the azimuth of linear polarization (red double-ended arrows) incident on the radially arrayed Henle fibers changes continuously as the scan progresses. **B.** Spinning-HWP RBS signal measured along S1. By spinning the HWP 1/16 as fast as the scan, the frequency of the S₁ signal changes from 4*f* to 3.5*f*.

Utilizing the measured corneal birefringence from the Knighton/Gramatikov data set of 300 human eyes, an algorithm was developed to find the HWP rotation speed, more precisely the specific odd multiple of 1/16 of the scanning frequency, that would statistically maximize the power throughput for this representative group of people.

In the RBS computer model, the spinning half wave plate was modelled by the Müller matrix of a retarder (Equation 3.19) with retardance $\delta_{HWP} = 180^\circ$, and fast axis orientation, θ_{HWP} . The latter is continuously changing with time, at an odd multiple of 1/16 of the scanning frequency or angular rotation of the 7° wave plate ($\delta_r = 7^\circ$), with θ_r , representing the circular scan of 3° in subtended diameter on the retina in the case of central fixation:

$$\theta_{HWP} = (2n + 1) \cdot \frac{\theta_r}{16} \quad \left[= (2n + 1) \cdot \frac{\omega_r t}{16} = (2n + 1) \cdot \frac{2\pi f t}{16} \right] \quad (5.14)$$

During simulated central fixation, a beam of initially vertically polarized light ($\vec{S}_{in} = (1, -1, 0, 0)^T$), was scanned on the retina, continuously changing in the orientation of its linear polarization after passing through the spinning HWP (actually continuously changing elliptically polarized light being scanned on the retina, because passage through the cornea in general produces elliptically polarized light). The HWP was added to the optical system operating on both the incoming and the returning path (double-pass):

$$\begin{aligned} \vec{S}_{out} = & \mathbf{M}_{HWP(out)}(\delta_{HWP}, -\theta_{HWP}) \cdot \mathbf{M}_{cornea(out)}(CR, -CA) \cdot \mathbf{M}_{retina(out)}(\delta_r, -\theta_r) \cdot \mathbf{M}_{fundus} \cdot \dots \\ & \cdot \mathbf{M}_{retina(in)}(\delta_r, \theta_r) \cdot \mathbf{M}_{cornea(in)}(CR, CA) \cdot \mathbf{M}_{HWP(in)}(\delta_{HWP}, \theta_{HWP}) \cdot \vec{S}_{in} \end{aligned} \quad (5.15)$$

Optimization was achieved by varying n from 0 to 7. For each HWP rotation frequency, $f_{HWP} = 1/16, 3/16, 5/16, \dots, 15/16$ times f , the relevant “multiple of half” frequency component in the RBS signal was determined, at which the FFT power was then computed for each of the representative corneal retardance and azimuth combinations in the Knighton/Gramatikov data set. The sum of these RBS signal strengths of the Knighton/Gramatikov eyes was calculated for a given frequency, representing a particular HWP rotation speed, and the HWP rotation frequency with the highest number (maximum sum) was chosen to be the best rotation speed. The results are shown in a histogram in Figure 5.13.

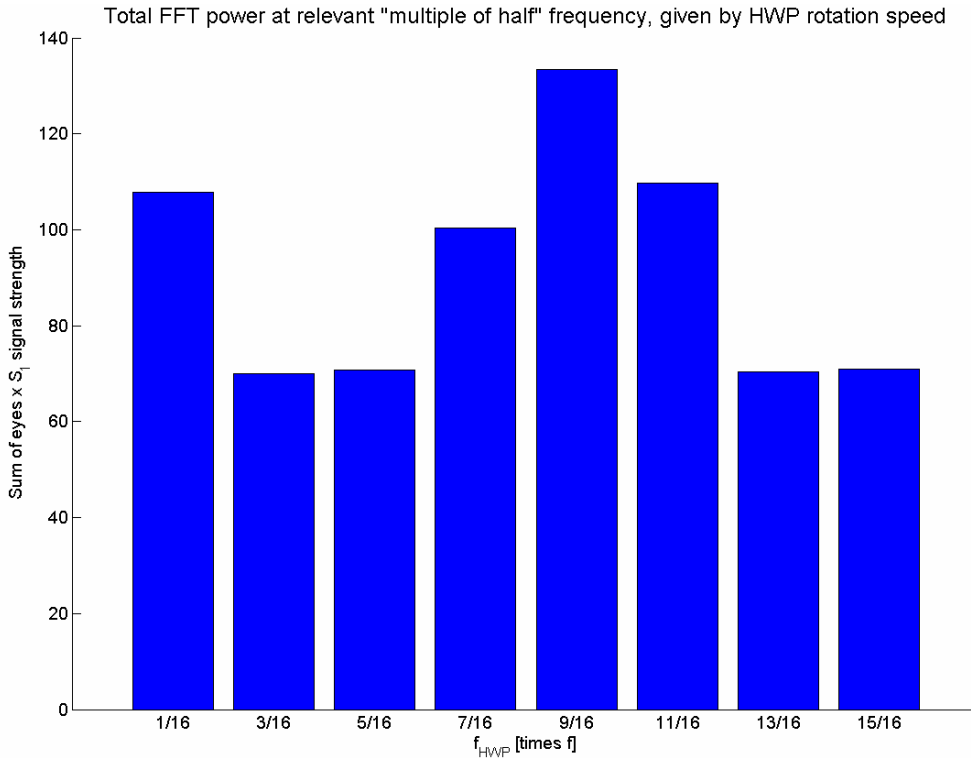


Figure 5.13: Distribution of the total FFT power (sum over all S_1 signal strengths of the eyes in the Knighton/Gramatikov data set) in relative power units at the relevant “multiple of half” frequency, determined by the rotation frequency of the HWP that is an odd multiple of $1/16$ of the scan frequency.

As can be seen, RBS signal strength is maximized by spinning the half wave plate at a fractional frequency that is $9/16$ as fast as the scanning frequency. At this particular rotation speed, the modulation produced by the half wave plate causes the polarization-related changes arising from the Henle fibers to occur predominantly at $2.5f$.

The differential polarization signal can then be calculated by shifting the recorded RBS signal by one period, and subtracting it from the original signal, which is necessary to subtract out the unwanted effects of facial-reflected depolarized light. At the same time, by performing this 360° -phase-shift subtraction, the $2.5f$ RBS signal will double in magnitude and even quadruple in FFT power, as mentioned earlier.

However, the full advantage of the spinning HWP design cannot be appreciated when the subject's corneal retardance (CR) is low or close to zero. The Figures 5.14 and 5.15 show that the RBS signal falls off with low values of CR, and goes to zero when corneal retardance is zero. The contour plot (Figure 5.15) reveals that 164 (55%) of the human eyes in the Knighton/Gramatikov data set fall below the "0.4" contour, only with low CR.

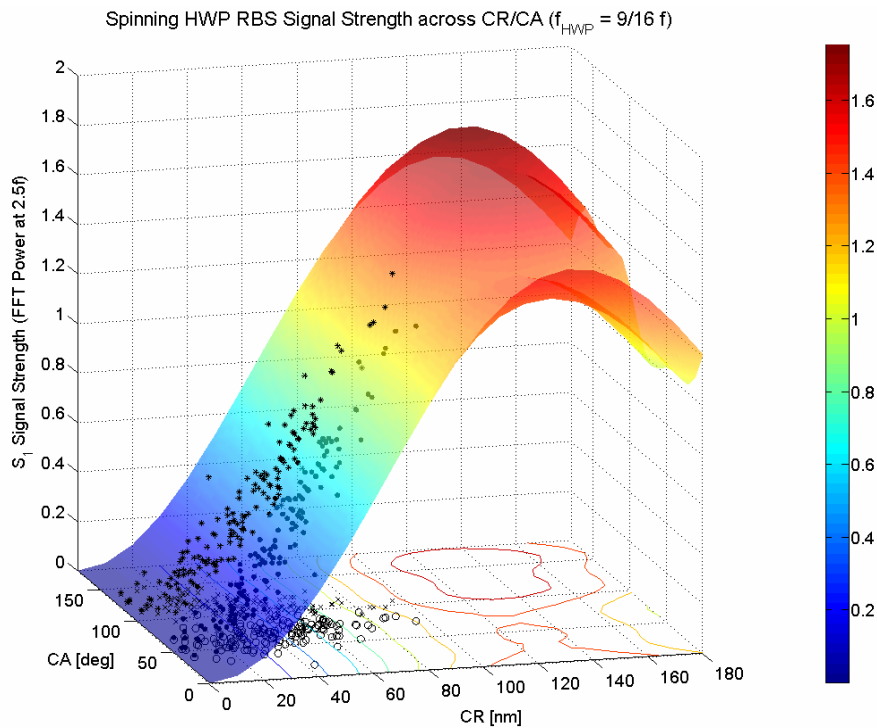


Figure 5.14: RBS signal strength at $2.5f$ (in relative power units) as a function of corneal retardance (CR) and corneal azimuth (CA) with the HWP spun $9/16$ as fast as the scan.

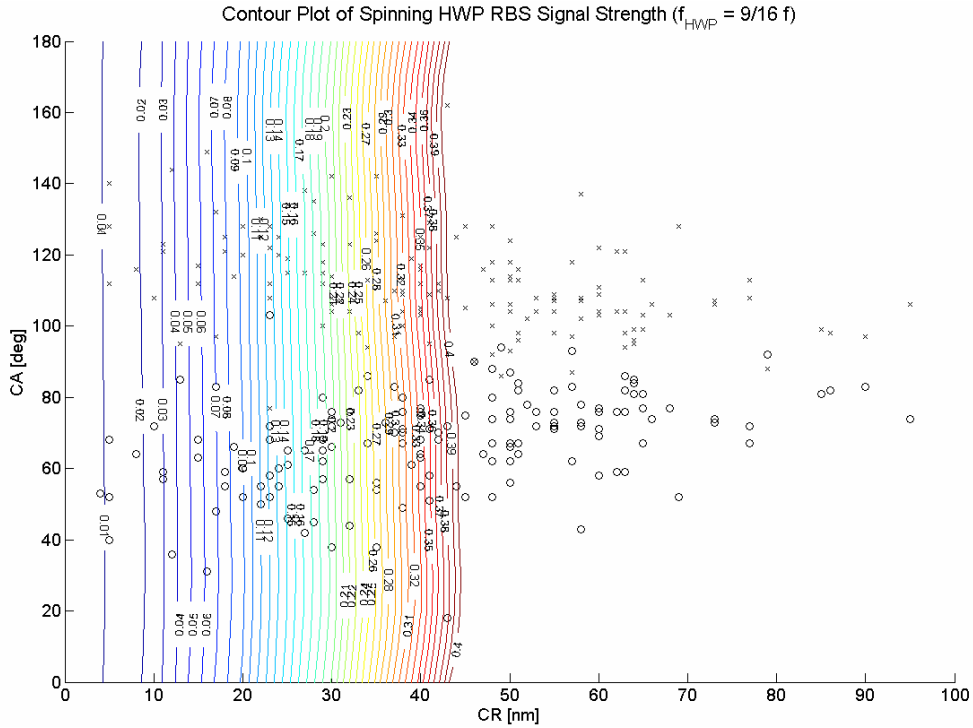


Figure 5.15: Contour plot of RBS signal strength at $2.5f$ (in relative power units) as a function of corneal retardance (CR) and corneal azimuth (CA) with the HWP spun $9/16$ as fast as the scan.

The key to understanding this poor performance with low CR is that when corneal retardance is close to zero, there is too little fixed double-pass retardance to rotate the spinning polarization states away from the equatorial plane of the Poincaré sphere, where they remain spinning as linear polarization states upon first passage through the rotating half wave plate. As a result the half wave plate basically undoes its own effect on the return path, and the retina has only little effect on the generated path of polarization states. In other words, though the $9/16 f$ rotation speed of the half wave plate causes the retina-derived changes to occur at a “multiple of half” frequency of the scan frequency, with no fixed amount of retardance present to shift the path of polarization states from the equatorial plane before striking the retina, there is no gain in the size of the retina-derived path of polarization changes. Depending on the spinning frequency of the HWP, only a fraction of the ‘small’ known figure-of-eight path caused by retinal birefringence remains.

This becomes readily visible by means of Poincaré analysis when considering an eye whose corneal retardance is zero. The changes of initially vertical linear polarized light during the double pass through the half wave plate, spinning $9/16$ as fast as the scan, and during the double pass through the retinal birefringence, are illustrated in Figure 5.16.

During one revolution of the scan, the blue eigenvector of the HWP, situated in the equatorial plane, rotates from 0° to 202.5° around the sphere's origin, causing the initial polarization axis (red dot at the back of the equator) to rotate twice as fast, from 90° through 360° to 135° . With the HWP spinning at $9/16 f$, the axis of polarization incident on the nerve fibers is slightly ahead of the fiber's fast axis, so that the eigenvector of the foveal birefringence spinning twice around the sphere's origin during one cycle basically causes a helical (downward) movement of the polarization states. With reflection from the ocular fundus, each polarization state and each eigenvector effectively rotates 180° about the S1 axis, causing the $2^{1/4}$ -traced path of polarization states to subsequently spiral up. The second pass through the Henle fibers increases the distance of the $2^{1/4}$ -traced helical path from the equator. The HWP, whose eigenvector is now spinning in the opposite direction compared with the initial passage, basically undoes its own effect on the return passage. (If there were no retinal birefringence, the second passage through the HWP would exactly undo its own effect due to the direction of rotation of its eigenvector that is reversed upon reflection from the fundus, yielding the same as the initial vertical polarization state.) What remains is a quarter-traced figure-of-eight path. Thus, when corneal retardance is close to zero, the only significant frequency component in the RBS signal measured along the S1 axis is $0.5f$.

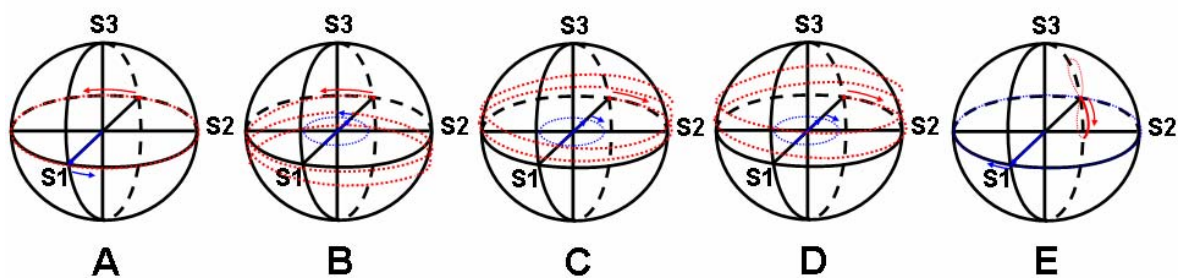


Figure 5.16: Changes in the state of polarization (red) during the double pass of LVP light through a spinning HWP ($9/16 f$) and an eye with zero CR, represented with Poincaré analysis. **A.** First pass through HWP. **B.** First pass through retina. **C.** Reflection from fundus. **D.** Second pass through retina. **E.** Second pass through HWP.

In other words, as a consequence of the axis of incident linear polarization being slightly ahead of the fast axis of Henle fiber birefringence due to the $9/16 f$ rotation speed of the HWP, there is only one location at which the azimuth of linear polarization is 45° to the nerve fiber orientation, and that is at the final position of the first scanning cycle (360°). Referring to the simplified considerations from Figures 5.7 and 5.12, where

corneal birefringence was neglected to explain the origin of the frequency components in the RBS signals, one can see that this leads to a dominating frequency component in the RBS signal of exactly 0.5 times the scanning frequency ($0.5f$).

Thus, we have to add a fixed amount of artificial “corneal” birefringence, in other words, a fixed double-pass wave plate that has the potential to shift the polarization state of the light incident on the retina to the position on the Poincaré sphere where the retinal retardance will have the greatest effect on the size of the generated path of polarization states, and then shift the polarization states of the generated path of polarization states back to the position on the Poincaré sphere where the path of polarization states will project maximally onto the S1 axis – yielding the largest retina-derived signal.

5.2.4 Finding the Optimum Fixed Double-Pass Wave Plate

We need to find a double-pass wave plate, that in combination with the double-pass half wave plate spinning at $9/16 f$ yields high RBS signals preferably uniform over the population range of corneal birefringence. With the objective of maximizing RBS signal strength while minimizing the variability of the scan between eyes and among subjects, an algorithm was developed for optimizing both retardance and azimuth (fast axis orientation) of the fixed double-pass wave plate. In the RBS computer model, the wave plate with unknown retardance, δ_{WP} , and azimuth, θ_{WP} , was inserted in between the HWP and cornea:

$$\begin{aligned} \vec{S}_{out} = & \mathbf{M}_{HWP(out)}(\delta_{HWP}, -\theta_{HWP}) \cdot \mathbf{M}_{WP(in)}(\delta_{WP}, -\theta_{WP}) \cdot \mathbf{M}_{cornea(out)}(CR, -CA) \cdot \dots \\ & \cdot \mathbf{M}_{retina(out)}(\delta_r, -\theta_r) \cdot \mathbf{M}_{fundus} \cdot \mathbf{M}_{retina(in)}(\delta_r, \theta_r) \cdot \mathbf{M}_{cornea(in)}(CR, CA) \cdot \dots \\ & \cdot \mathbf{M}_{WP(in)}(\delta_{WP}, \theta_{WP}) \cdot \mathbf{M}_{HWP(in)}(\delta_{HWP}, \theta_{HWP}) \cdot \vec{S}_{in} \end{aligned} \quad (5.16)$$

The double-pass wave plate was computed that, for the 300 right and left eyes in the Knighton/Gramatikov data set, would statistically maximize RBS signal strength (FFT power), while having the greatest independence from the various amounts and orientations of corneal birefringence. Optimization was achieved by varying the properties of the wave plate on a grid covering 0° to 180° retardance, and 0° to 180° azimuth. To minimize processing time, both variables were stepped through in increments of 10 degrees, sufficient to get a first impression and localize the appropriate range of retardance and azimuth. For each incremental step, the mean and standard deviation of the RBS signal strengths (FFT power at $2.5f$) of the 300 representative eyes was calculated. The normalized standard deviation, in other words, the standard deviation divided by the mean

for each retardance/azimuth combination was then determined, and the minimum of these 19 normalized standard deviations was computed according to the requirement of finding a retardance that yields maximal signal strength with the least variability across CR and CA.

The algorithm measured the minimum normalized standard deviation with the fixed retarder having a retardance of 50° and fast axis at 110° , however, remember this is with an incremental resolution of 10 degrees. The algorithm suggested the overall minimum, in other words the best choice of retardance/azimuth combination for the fixed double-pass wave plate, to be located within the range of 40° to 60° retardance and 85° to 115° fast axis orientation (see Figure 5.17).

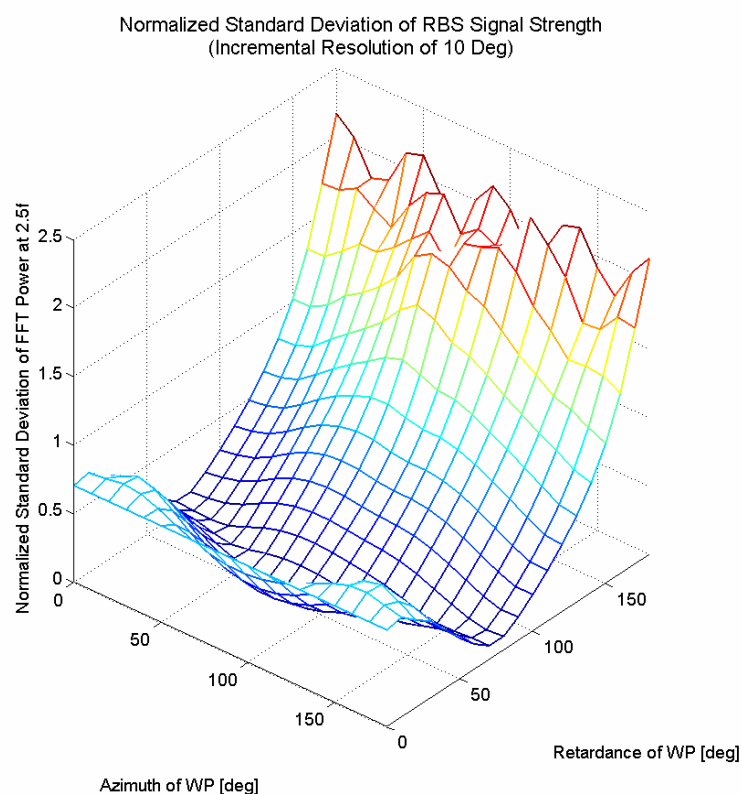


Figure 5.17: Normalized standard deviation of RBS signal strengths of the eyes in the Knighton/Gramatikov data set as a function of retardance and azimuth (fast axis orientation) of the double-pass wave plate. The retarder properties were varied with an incremental resolution of 10° .

Thus, the same optimization algorithm was applied with a higher incremental resolution, while varying the retarder properties within the suggested range in 1° steps.

The results are presented in Figures 5.18 and 5.19. The lowest normalized standard deviation was calculated for a wave plate having a retardance of 45° and fast axis orientation of 88° .

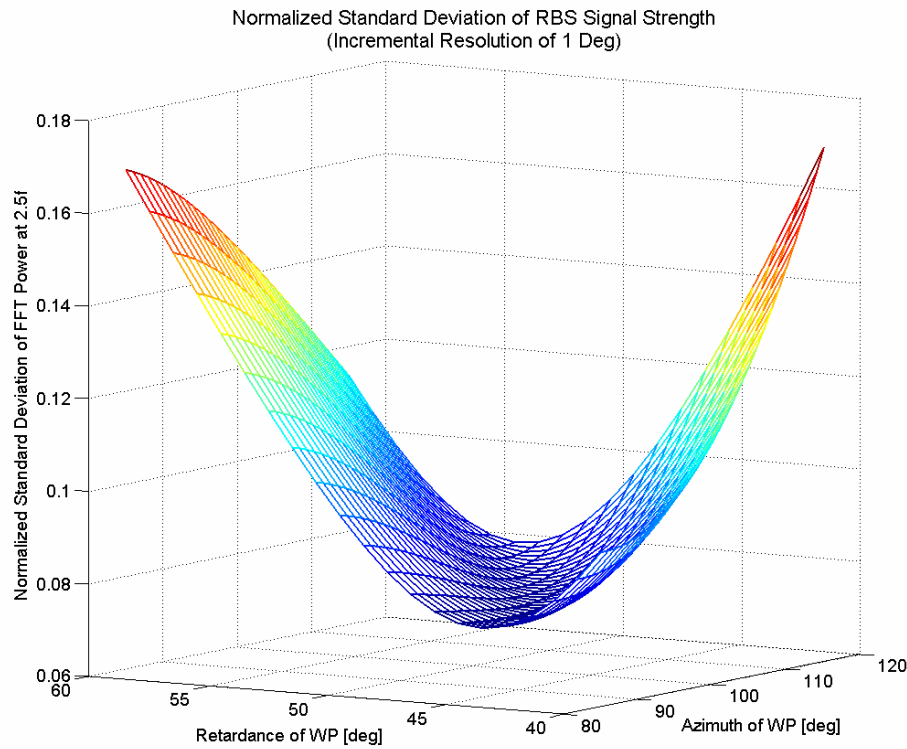


Figure 5.18: Normalized standard deviation of RBS signal strengths of the eyes in the Knighton/Gramatikov data set as a function of retardance and azimuth (fast axis orientation) of the double-pass wave plate. The retarder properties were varied with an incremental resolution of 1° .

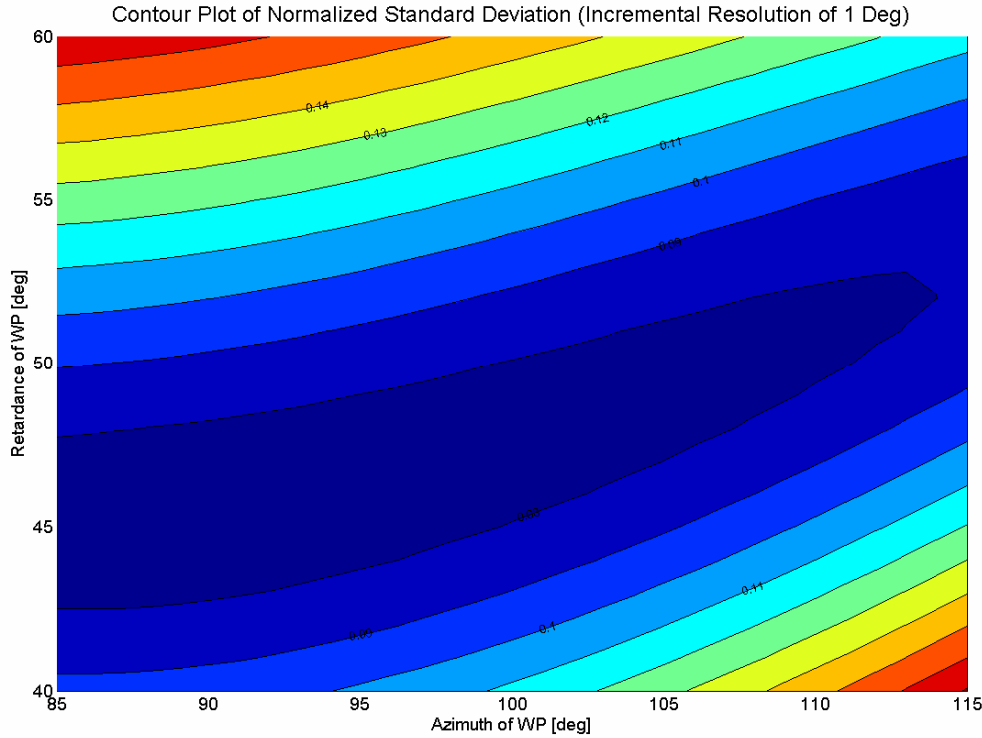


Figure 5.19: Contour plot of normalized standard deviation of RBS signal strengths of the eyes in the Knighton/Gramatikov data set as a function of retardance and fast axis orientation of the double-pass wave plate.

However, according to the requirements of minimizing the variability of RBS between eyes, an azimuth of 90° was favored as fast axis orientation of the double-pass 45° wave plate. Minimizing intra-subject variability basically means to make the surface of distributed S_1 signal strengths in the 3D-plot as symmetric as possible about 90° CA. Recall that with reflection from the ocular fundus, the eigenvector rotates 180° about the S_1 axis. Thus, if the added fixed retarder is oriented at 90° , this location of the eigenvector – aligned with S_1 – remains unaffected upon reflection, retaining the symmetry between the eyes, whose corneal azimuths can basically be considered as being mirror images about the S_1 axis.

The difference in normalized standard deviation between an azimuth of 90° and 88° is negligible, as can be seen in Figure 5.19 above. For both axes, the predicted normalized standard deviation is below the smallest contour of 0.08, with the first difference occurring in the fourth digit (0.074563 at 88° , compared with 0.074648 at 90°), so that choosing 90° as best fast axis orientation of the 45° wave plate to meet the requirement of greatest intra-subject symmetry appears reasonable.

Nevertheless, we wanted to confirm that at the given, favored azimuth of 90° , our optimization algorithm would still calculate 45° as being the best amount of retardance for the double-pass retarder. Thus, instead of varying both retardance and azimuth, the algorithm was applied at the given 90° azimuth by varying the retardance from 0° to 180° . With the low incremental resolution of 10 degrees, the algorithm measured a minimum normalized standard deviation with the fixed retarder having a retardance of 50° , and suggested the overall minimum to be within 40° and 50° (see Figure 5.20 A). Repeating the calculations with an increased incremental resolution of 1° covering the suggested range, the algorithm confirmed a retardance of 45° to be the best amount for the fixed double-pass wave plate, shown in Figure 5.20 B.

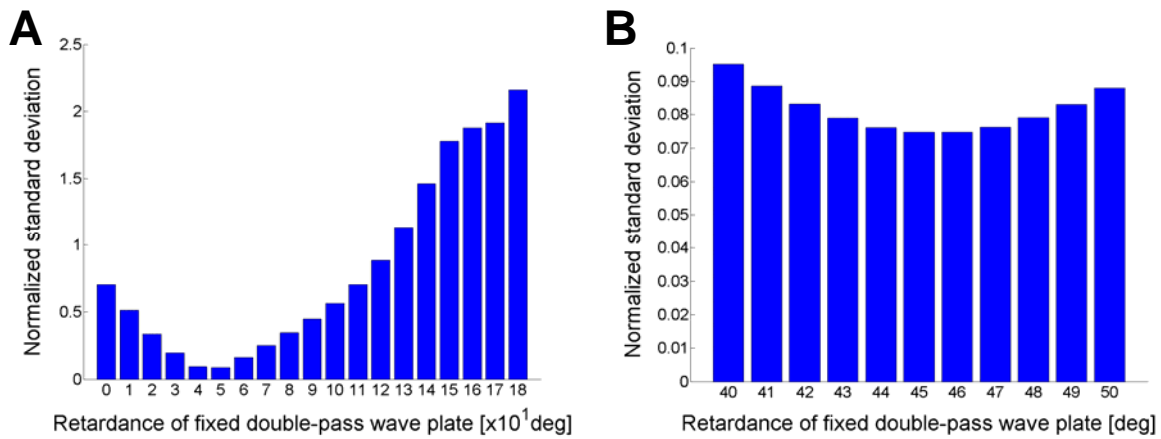


Figure 5.20: Distribution of normalized standard deviation of RBS signal strengths of the eyes in the Knighton/Gramatikov data set as a function of retardance. The retardance of the fixed double-pass wave plate was varied: **A.** from 0° to 180° in incremental steps of 10 degrees, **B.** from 40° to 50° in 1° steps, and the normalized standard deviation of FFT power was calculated considering all eyes from the Knighton/Gramatikov data set.

By adding a 45° wave plate or “ $1/8$ ” wave plate, with fixed azimuth of 90° , to the spinning HWP RBS design, with HWP rotation frequency optimized to $9/16$ of the scan frequency ($f_{HWP} = 9/16 f$), the $2.5f$ frequency component dominates in the S_1 foveal fixation signal even with low and zero corneal retardance. How exactly adding a fixed amount of 45° retardance at 90° to the double-pass system causes the retina-derived signal to repeat at $2.5f$ with zero corneal retardance is explored in more detail below.

Figure 5.21 shows that with the added $1/8$ wave plate (WP), the RBS signal strength becomes very large and practically uniform over the population range of corneal retardances and azimuths. The power at $2.5f$ drops below the previously set threshold of

0.4 only at margins where there are no eyes present, as shown in the contour plot of RBS signal strength across CR/CA (Figure 5.22). In the Knighton/Gramatikov data, there are neither eyes with corneal retardances higher than 100 nm, nor eyes with corneal azimuths lower and higher than 15° and 165° respectively. RBS signal strength decreases slightly for right eyes with very low and left eyes with very high corneal azimuths respectively, and for eyes with higher corneal retardances, but never falls below a signal level of 0.8. The contour plot reveals that all 300 eyes in the Knighton/Gramatikov data set are well above the “0.4” contour, so that with this threshold setting no eye will fail the measurement with the optimized spinning HWP design.

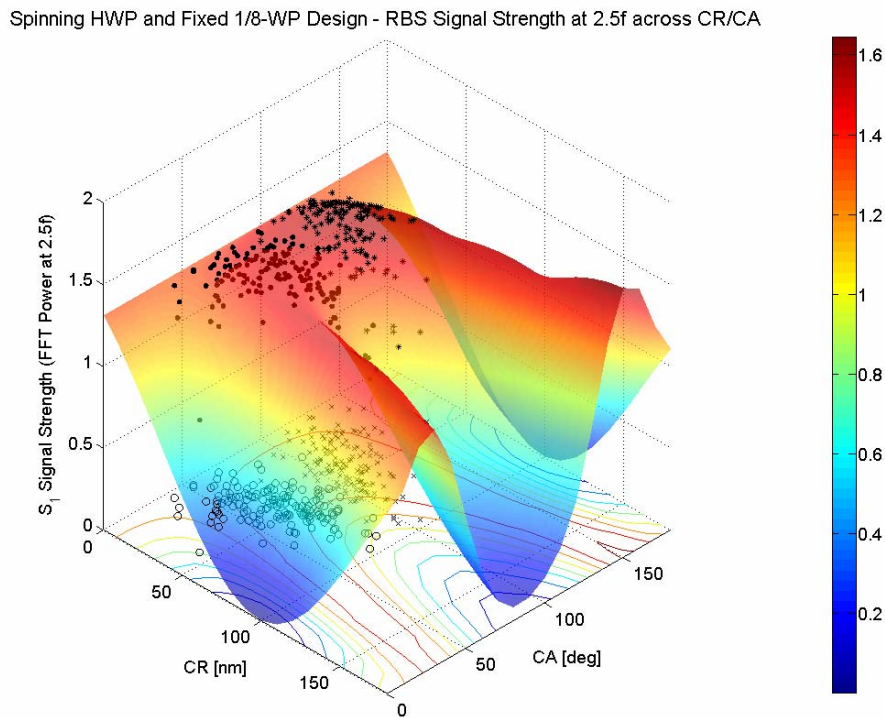


Figure 5.21: RBS signal strength at $2.5f$ (in relative power units) as a function of corneal retardance (CR) and corneal azimuth (CA) with optimized RBS design comprising a spinning HWP ($9/16f$), and a 1/8 wave plate (WP) with fixed azimuth of 90° .

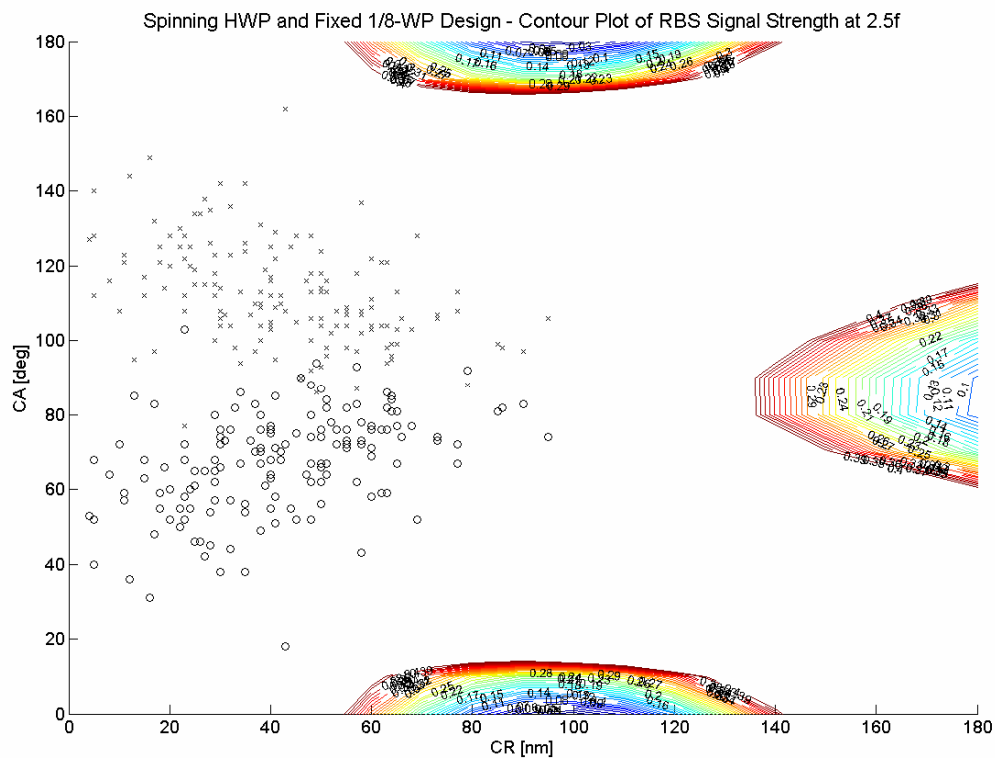


Figure 5.22: Contour plot of RBS signal strength at $2.5f$ (in relative power units) as a function of corneal retardance (CR) and corneal azimuth (CA) with the optimized spinning HWP and fixed 1/8 WP design.

Fourier analysis of the S_1 foveal fixation signal, “measured” with the optimized spinning HWP and fixed 1/8 wave plate RBS design, revealed that another frequency occurs with simulated central fixation ($6.5f$), that increases with high CR (see Figure 5.23). Including this frequency component in the analysis will greatly enhance foveal fixation detection for eyes with high corneal retardances. For demonstration purposes, the S_1 signal strengths for the two centered frequencies are simply added in Figures 5.24 and 5.25 to show the excellent coverage of various corneal retardances and azimuth that occur in the population with both centered frequencies being considered in the analysis.

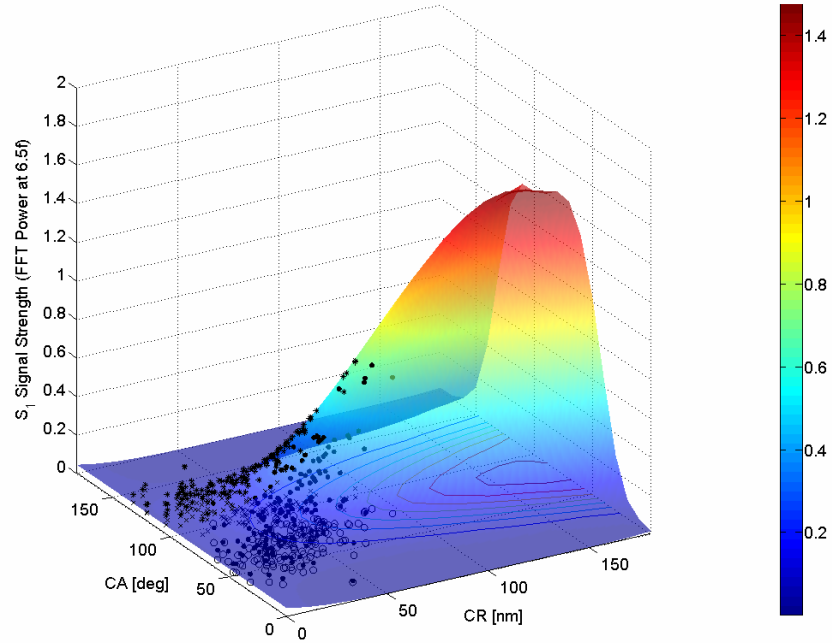
Spinning HWP and Fixed 1/8-WP Design - RBS Signal Strength at $6.5f$ across CR/CA

Figure 5.23: RBS signal strength at $6.5f$ (in relative power units) as a function of corneal retardance (CR) and corneal azimuth (CA) with optimized RBS design comprising a spinning HWP ($9/16f$), and a $1/8$ wave plate (WP) with fixed azimuth of 90° .

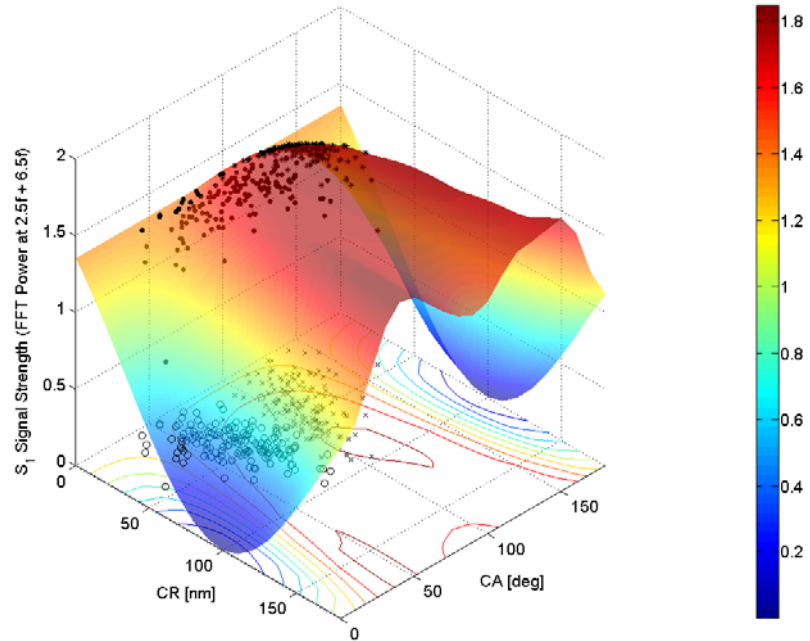
Spinning HWP and Fixed 1/8-WP Design - RBS Signal Strength at $2.5f$ & $6.5f$ across CR/CA

Figure 5.24: Sum of RBS signal strength at $2.5f$ and $6.5f$ (in relative power units) as a function of corneal retardance (CR) and corneal azimuth (CA) with optimized RBS

design comprising a spinning HWP ($9/16 f$), and a $1/8$ wave plate (WP) with fixed azimuth of 90° .

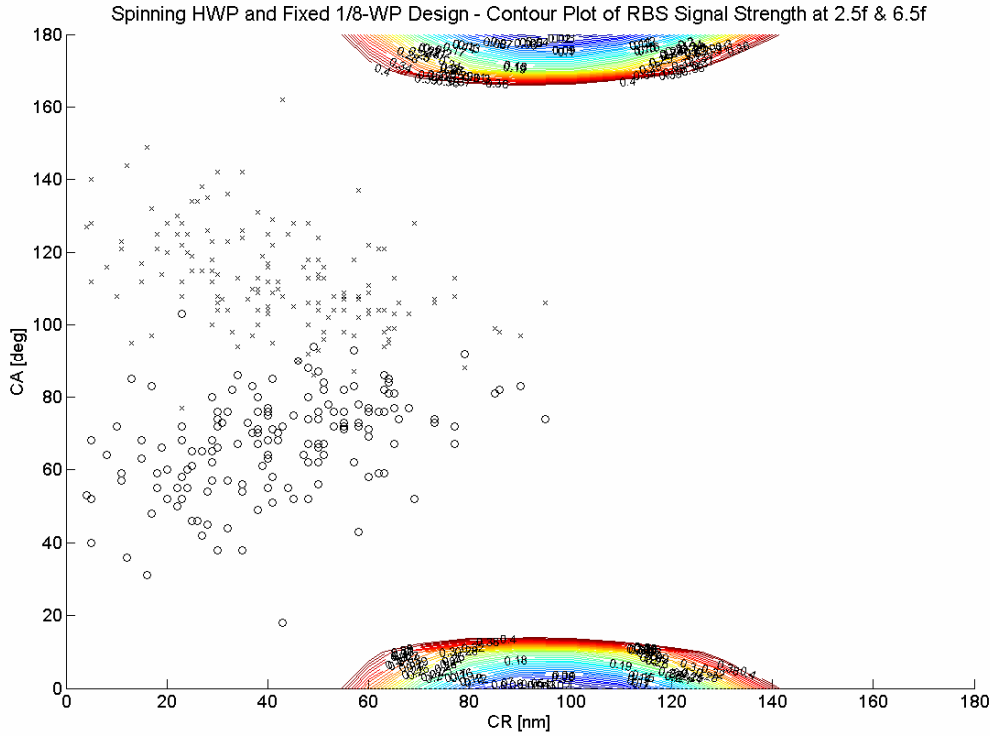


Figure 5.25: Contour plot of sum of RBS signal strength at $2.5f$ and $6.5f$ (in relative power units) as a function of corneal retardance (CR) and corneal azimuth (CA) with the optimized spinning HWP and fixed $1/8$ WP design.

The following shall provide a detailed explanation of the generation of the $2.5f$ frequency component in the S_1 foveal fixation signal for eyes with zero corneal retardance by adding the $1/8$ wave plate with fixed fast axis orientation of 90° to the double-pass $9/16 f$ spinning-HWP RBS system. It is essential to understand the effect of the $1/8$ wave plate on the generated path of polarization states through the non-ocular polarization-changing media first, that is the passage through the spinning HWP before and after reflection off the polarization preserving fundus, before including retinal birefringence in the consideration, as shown in Figure 5.26 with the help of Poincaré analysis. Recall that the HWP with $9/16 f$ rotation speed causes the initial polarization axis located at the back of the equator (LVP) to spin $2^{1/4}$ times about the S_3 axis with each scan cycle, generating a $2^{1/4}$ -traced path of linear polarization states situated in the equatorial plane. First passage through the $1/8$ wave plate, whose eigenvector is aligned with the S_1 axis, rotates this plane path of polarization states 45 degrees about the S_1 axis, away from the equator. Upon reflection

from the ocular fundus, the polarization states still rotate in the same oblique plane but in the opposite direction. As the eigenvector of the $1/8$ wave plate is aligned with the S1 axis, it remains unaffected with reflection from the fundus. Thus, second passage through the $1/8$ wave plate causes each polarization state to rotate an additional 45 degrees about the same axis as with initial passage, projecting the entire $2^{1/4}$ -traced path of polarization states onto the S1-S3 plane. The eigenvector of the HWP, on the other hand, is still spinning in the equatorial plane, just in the reversed direction upon fundus reflection. But the path of spinning polarization states, that was generated in the equatorial plane on initial passage through the spinning half wave plate, is now well away from the equatorial plane, and is no longer “undone” by the return pass through the HWP. A large figure-of-eight path is generated instead.

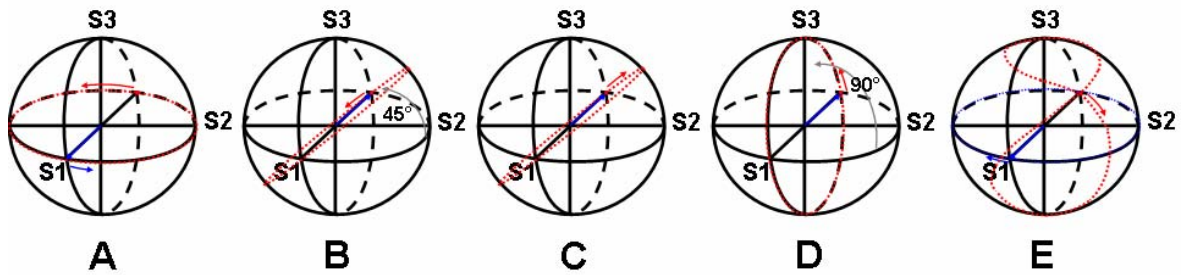


Figure 5.26: Changes in the state of polarization during the double pass of LVP light through a spinning HWP ($9/16 f$), a $1/8$ wave plate with fixed azimuth of 90° , and an eye with zero CR (retinal birefringence neglected), represented with Poincaré analysis. **A.** First pass through HWP. **B.** First pass through $1/8$ wave plate. **C.** Reflection from fundus. **D.** Second pass through $1/8$ wave plate. **E.** Second pass through HWP.

The formation of the final path in form of a figure-of-eight becomes readily visible when considering the maximal positions on the S1 and S3 axes. Since the polarization axis incident on the HWP rotates in the S1-S3 plane, the maxima and minima located on the S3 axis are exchanged, in other words rotated to the respective opposite sites of the sphere's pole upon return passage through the HWP forming the turning points of the figure-of-eight loops, independent of the orientation of the HWP's eigenvector at these positions. The same applies to the maxima on the S1 axis, intersecting with the equatorial plane, so that these polarization states rotate to the back of the equator, forming the nodal points of the final figure-of-eight path.

With the HWP spinning $9/16$ times as fast as the scan, the final figure-of-eight path is traced $2^{1/4}$ times, so that the generated signal measured along S3 therefore is 2.25 times

the frequency of the scan ($2.25f$). As described before, because the polarization state moves both above and below the equator, twice each during each scan, each maximum and minimum measured along S3 becomes a maximum when measured along S1, doubling the frequency of the signal (from $2.25f$ to $4.5f$). It is important to understand that this S₁ signal repeating at $4.5f$ is purely the result of the HWP rotation speed. The $4.5f$ signal is thus referred to as spinning artifact in the further course of this work.

Now that the generation of the figure-of-eight path is understood as the result of the return passage through the spinning HWP after introducing a fixed amount of “artificial” corneal retardance into the optical system, the effect of retinal birefringence on the $2^{1/4}$ -traced path of polarization states can be considered, eventually generating the $2.5f$ component in the RBS signal. An illustrative explanation of the generation of the $2.5f$ RBS signal is provided in Figure 5.27. As shown before, given the $9/16 f$ HWP rotation speed, retinal birefringence causes helical movement of the polarization states away from the plane in which they are spinning, thereby modulating the frequency of the generated signal. Thus, including retinal birefringence in the previous consideration of the double pass of linearly vertical polarized light through the spinning HWP and fixed $1/8$ wave plate RBS design, instead of spinning in the S1-S3 plane upon second passage through the $1/8$ wave plate without foveal birefringence being considered, the polarization states (red dotted path in Figure 5.27 A) basically spiral away from the S1-S3 plane in the minus direction along S2. The progression in the negative direction along S2 is seen best on projection of the helical path of polarization states onto the S1-S2 plane, emphasized by the red arrow in Figure 5.27 B. Numbers 1 to 16 represent the incremental retinal scan positions (22.5° steps) within the first scanning cycle. Recall that during one revolution of the scan, the eigenvector of the HWP (yellow and orange lines), situated in the S1-S2 plane, is spinning $9/16 \times 2 = 1^{1/8}$ times around the sphere’s origin (from 0° to 202.5°), causing the polarization axis to change twice as fast, so that the path of polarization states is traced $2^{1/4}$ times about the S2 axis. As light makes the return pass through the HWP, each polarization state rotates 180 degrees about the respective eigenvector of the HWP, generating the $2^{1/4}$ -traced figure-of-eight path as shown before. However, with retinal birefringence considered, the figure-of-eight varies in size on successive traced paths. This becomes clear when considering the return pass of those polarization states that will form the turning points of the loops of the final figure-of-eight, namely those polarization states that maximally and minimally project onto S3 before passing through the HWP. Incremental positions that project maximally and minimally onto S3 are the polarization states 2, 9, and 16 (encircled orange), and 5 and 12 (encircled yellow), respectively. The latter are located below the equator, so that they rotate about the corresponding yellow eigenvector to a position above the equator, forming the upper loop of the final figure-of-eight path. Due to

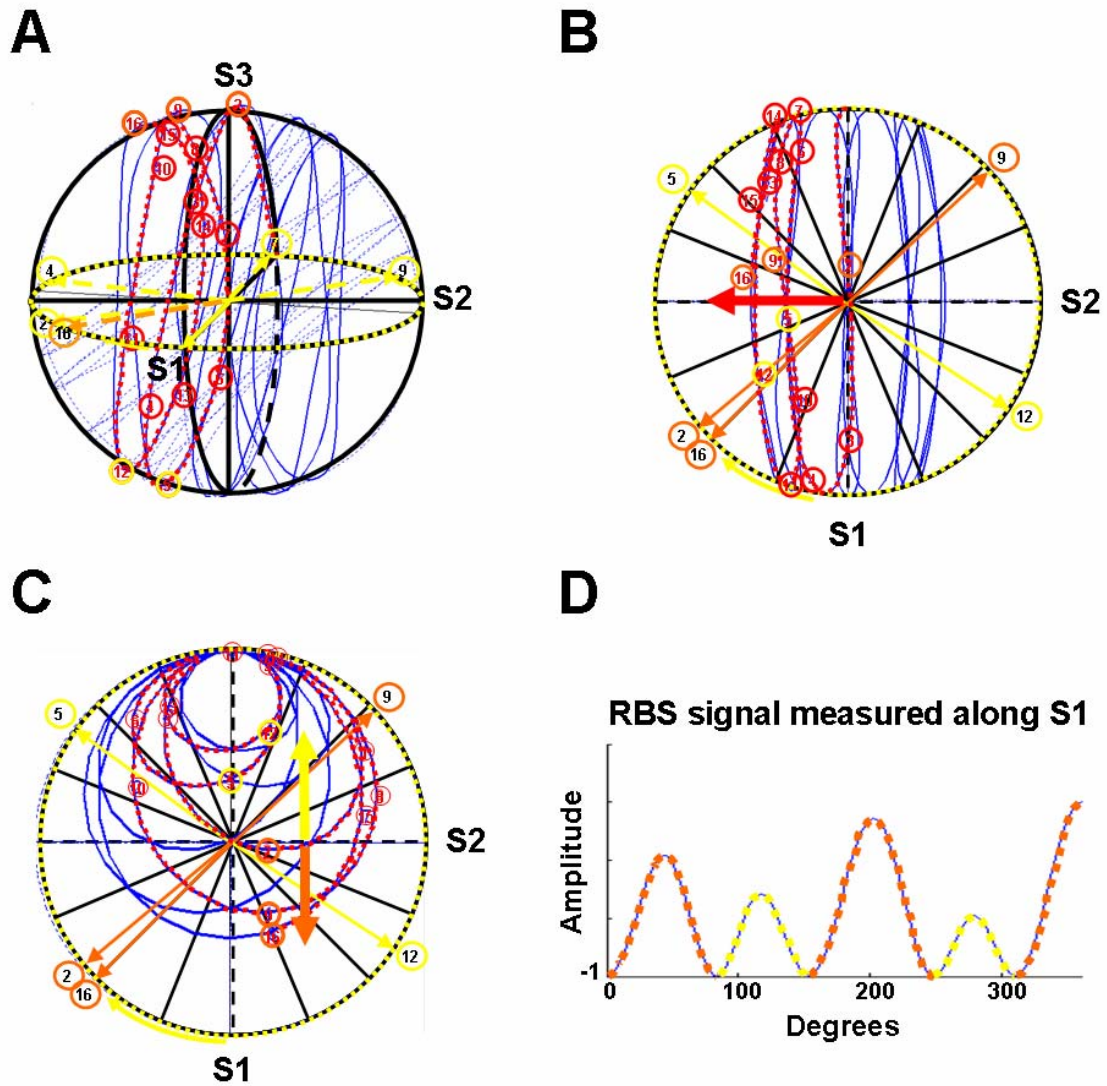


Figure 5.27: Generation of $2.5f$ frequency component in the S_1 foveal fixation signal, represented with Poincaré analysis. **A.** Second pass through $1/8$ wave plate with retinal birefringence considered. **B.** Projection of generated path of polarization states onto the S_1 - S_2 plane. **C.** Return passage through HWP. **D.** Predicted RBS signal for an eye with zero corneal retardance, measured with optimized spinning HWP and fixed $1/8$ wave plate RBS design, during simulated central fixation.

the induced sidewise movement of the polarization states by retinal birefringence, the projection of polarization state 5 onto S2 is larger (less negative) than that of polarization state 12. Consequently, the upper loops of successive traced figure-of-eights decrease in size (emphasized by yellow arrow in Figure 5.27 C). Polarization states 2, 9, and 16, on the other hand, situated above the equator, are rotated about the respective orange eigenvectors, so that the lower loops formed by these polarization states increase in size on successive traced figure-of-eight paths (orange arrow in Figure 5.27 C). From the projection of the final path of polarization states on the S1 axis (Figure 5.27 D), it becomes obvious that the variation in size of successive traced figure-of-eights produces another frequency component in the signal ($2.5f$).

In summary, the sidewise movement of polarization states in the minus direction along S2, caused by retinal birefringence, basically turns into a progression along S1 on return passage through the HWP, with the projections of prior maxima and minima on S3 progressing in positive and negative directions along S1 respectively. As a result, the first loop of successive traced figure-of-eights increases in size, while the second one decreases, modulating the originally $4.5f$ signal (representing a figure-of-eight with equally sized loops), such that a strong frequency component of $2.5f$ is generated in the measured signal along S1 (representing the dominating first loop of successive traced figure-of-eights).

5.2.5 Differential Polarization Subtraction with Optimized Spinning-HWP RBS Design

The differential polarization signal is needed to eliminate repetitive optical noise such as depolarized light previously equally distributed to the paired photodetectors and thus subtracted out with the former method of differential polarization detection. This is calculated by shifting the acquired signal by one cycle, or 360° , and then subtracting the 360° -phase-shifted signal from the original. Fast Fourier Transformation is computed on the resultant signal after 360° -phase-shift subtraction, that is, on the differential polarization signal.

To simulate computation of the differential signal within the RBS computer model, instead of acquiring 16 cycles as before, a total number of 17 scans are acquired, whereupon scans 2 to 17 are subtracted from scans 1 to 16, yielding the desired differential polarization signal. FFT is computed on this resultant 16-cycle signal. As shown in Figure 5.28, the total differential foveal fixation signal (sum of $2.5f$ and $6.5f$) is quadrupled in FFT power compared with the signal before the 360° -phase-shift subtraction (see Figure 5.24).

Spinning HWP and Fixed 1/8-WP Design - RBS Signal Strength at 2.5f & 6.5f across CR/CA
after 360deg-Phase-Shift Subtraction

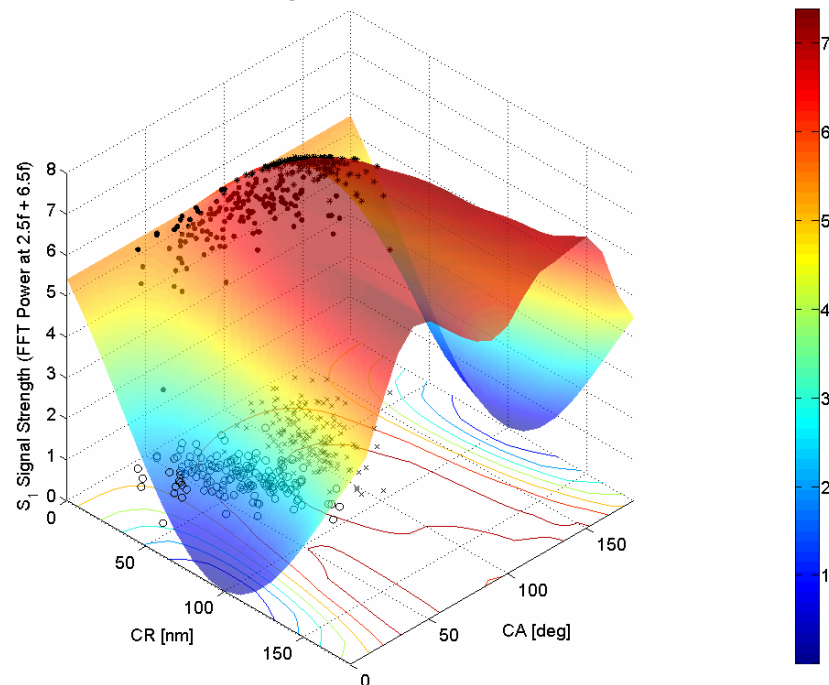


Figure 5.28: Sum of RBS signal strength at 2.5f and 6.5f (in relative power units) after 360°-phase-shift subtraction as a function of corneal retardance (CR) and corneal azimuth (CA) with optimized RBS design comprising a spinning HWP (9/16 f), and a 1/8 wave plate (WP) with fixed azimuth of 90°.

As can be seen, foveal fixation detection is greatly enhanced with the computer-optimized spinning half wave plate and 1/8 wave plate RBS design. High differential polarization signals are obtained over more than the entire known range of corneal birefringence for both eyes. In comparing the sum of RBS signal strengths of the 300 right and left eyes in the Knighton/Gramatikov data between the optimized design and the previous RBS design implemented into the 2002 prototype PVS, a significant statistical improvement of 7.3 times in RBS signal strength is achieved with the computer-optimized design using the spinning half wave plate and fixed 1/8 wave plate.

We have seen that the large figure-of-eight signal purely resulting from the HWP rotation speed, referred to as spinning artifact, is essential to generate the 2.5f component. As with the retina-derived changes, however, this spinning artifact repeats at a “multiple of half” frequency of the scan frequency (4.5f), so that this frequency component in the acquired signal will quadruple in FFT power as well when the signal is digitally shifted by

360° and then subtracted for the purpose of differential polarization detection, yielding an extremely high power at $4.5f$ (see Figure 5.29). The spinning artifact could theoretically be eliminated by an additional 80°-phase-shift subtraction, after the 360°-phase-shift subtraction. However, for a final application geared towards pediatric vision screening, requiring focus detection in addition to eye alignment detection, much power at this frequency may be ideal for detection of focus using the bull's-eye photodetector. The advantage of the spinning artifact is that all eyes yield a very high to extremely high signal level. Moreover, the $4.5f$ signal, as being the pure result of the HWP rotation speed, is relatively independent of fixation (see Appendix), and thus can be used independently from the alignment detection.

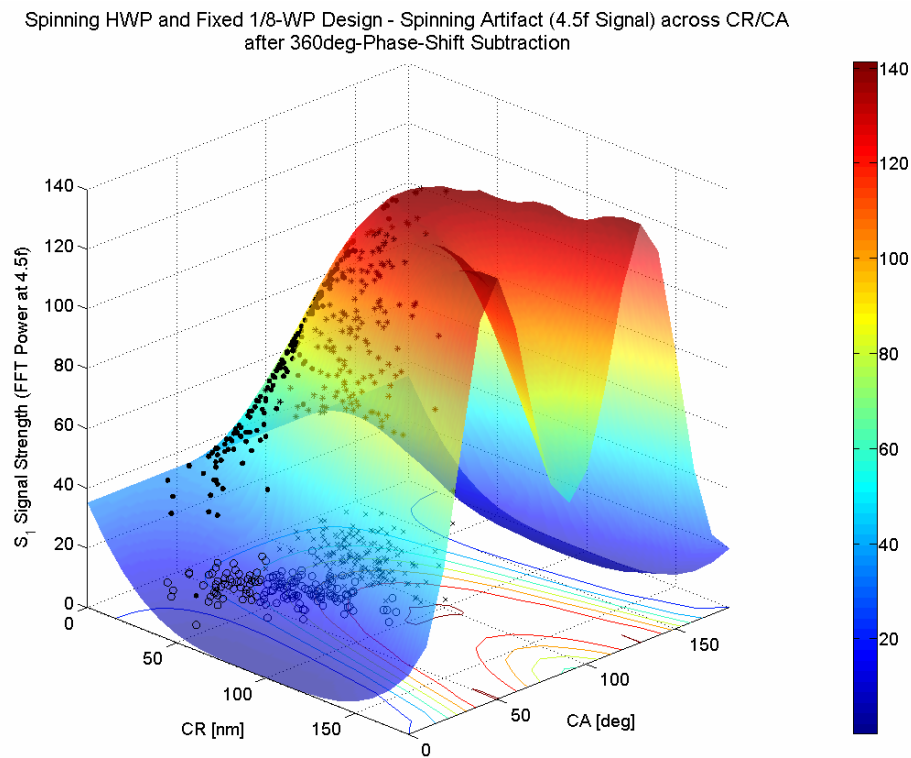


Figure 5.29: Signal strength of spinning artifact ($4.5f$ component) in relative power units after 360°-phase-shift subtraction as a function of corneal retardance (CR) and corneal azimuth (CA) with optimized RBS design comprising a spinning HWP ($9/16 f$), and a 1/8 wave plate (WP) with fixed azimuth of 90°.

Chapter 6

Validation of RBS Computer Model

Before proceeding with the implementation of the optimized spinning HWP and fixed 1/8 wave plate design for the Pediatric Vision Screener, we first sought to validate the RBS computer model with experimental human data using an intermediate RBS system. Our previously developed mathematical model, upon which the current computer model was developed, has been shown to accurately predict the frequency and phase of the RBS signal during central and paracentral fixation [Hun99(2)]. However, the effect of varying corneal birefringence on the strength (FFT power at the predicted frequency) of the RBS signals has not yet been considered, nor verified with actual eyes.

Thus, we wished to verify the ability of our computer model to predict the variation in RBS signals with different amount and orientations of corneal birefringence that occur in the population. We wished especially to test the optimization algorithm from Chapter 5.2.4, that is the model's ability to find the optimum amount of double-pass retardance necessary to yield maximal signal strength with the least variation across the population range of corneal retardances and azimuths.

6.1 Experimental Setup

6.1.1 Intermediate Eye Fixation Monitor

A monocular, “non-spinning” version of the eye fixation monitor was used for this assessment, simplified but sufficient to validate the logic of the model. This apparatus had been constructed using plane mirrors for the scanning system instead of a concave mirror, avoiding optical degradation of the double-pass image. “Non-spinning” refers to an RBS design that still employs two photodetectors to measure the differential polarization signal,

as opposed to the anticipated “spinning” RBS design for the Pediatric Vision Screener using a spinning HWP to realize differential polarization detection with only one detector.

The monocular eye fixation monitor described in detail in [Mue06] was used for the purpose of model validation, modified to allow for incorporation of a double-pass retarder at various azimuths, operating in both the incoming and return paths. Figure 6.1 illustrates the entire device in two views, drafted with AutoCAD. For the sake of clarity, the following consideration is made by dividing the opto-mechanical system into two sub-systems, the target system shown in green and the RBS system emphasized in blue. The latter is of major importance with regard to RBS model validation purposes, as it defines the parameters for the “non-spinning” RBS design.

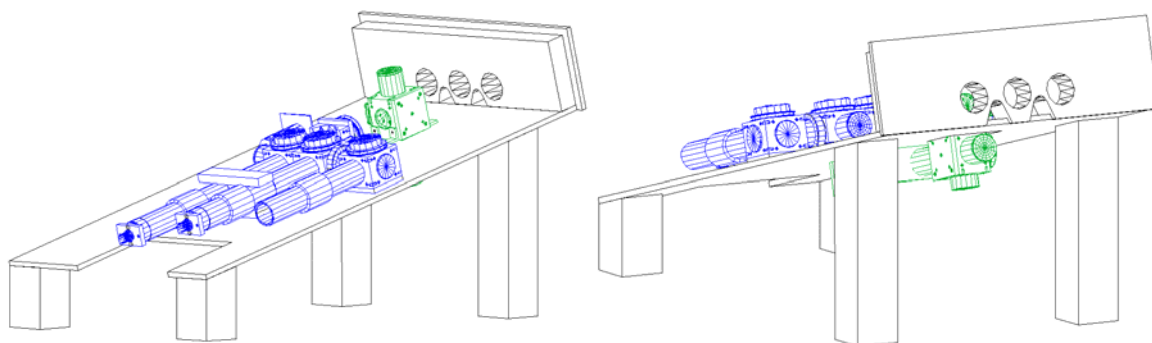


Figure 6.1: Intermediate monocular eye fixation monitor illustrated in two oblique views.

The monocular RBS system is detailed in Figure 6.2. A 785 nm laser diode (LD1) produces linearly vertical polarized light, which is deflected by a gold mirror (GM) through a 100 mm biconvex lens (L1) and a non-polarizing beam splitter (NPBS) with 70% transmission. The light is then reflected by a polarizing beam splitter (PBS) into a scanning unit, which consists of two plane gold mirrors (M1 and M2) in a “parallel” arrangement (as opposed to a folded-back plane mirror setup that was used before in RBS for biometric purposes [Irs07]) retaining the original axis of polarization. As the mirrors are spun ($f = 40$ Hz) by a motor (not shown), the stationary beam is converted into a circular scan, subtending an visual angle of approximately 3° at the subject’s eye (not shown). By the eye’s own optics, the beam is focused on the retina, and follows the same path back out of the eye after being reflected from the ocular fundus. The polarizing beam splitter separates the polarization-altered light into two orthogonal components. The

horizontal polarization component is transmitted, passes through a 100 mm focal length biconvex lens (L2) and a 780 nm bandpass filter (F1), before finally reaching one of the two photodetectors (PD1). The vertical polarization component is reflected by the polarizing beam splitter (PBS), and 30% is directed by the non-polarizing beam splitter (NPBS) towards the second photodetector (PD2) after passing another focusing lens (L3) and bandpass filter (F2) with the same properties. The balanced outputs of the paired photodetectors are subtracted, yielding the differential polarization signal (S_1 signal). The output signal is amplified, filtered, and transmitted to a PC for analog-to-digital (A/D) conversion and further digital analysis.

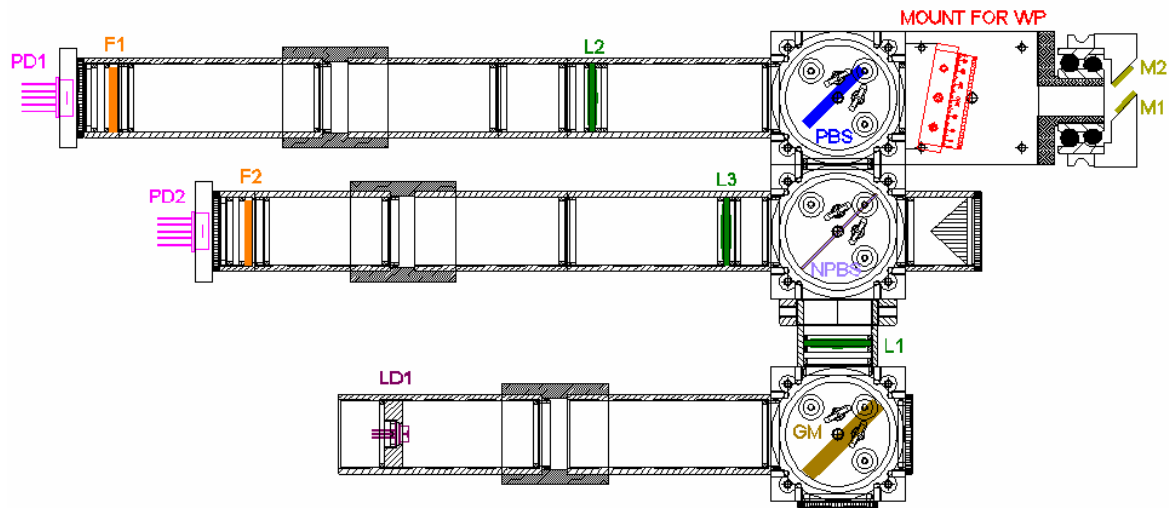


Figure 6.2: Opto-mechanical layout of the “non-spinning” RBS system of the monocular eye fixation monitor (top view).

A custom-made aluminum holder, screwed to the cage cube holding the PBS, allows the addition of a fixed double-pass wave plate to the system. The holder is tilted about 10 degrees to reduce specular reflection of light from the flat double-pass surfaces of the wave plate back into the optical system, which would create much optical noise. The retarder can optionally be attached to the angled holder by means of a rotary mount. The rotary mount is graduated in 2-degree increments, allowing manual rotation of the wave plate’s fast axis to various verifiable orientations.

In terms of laser safety issues, the measured intensity of 785 nm light entering the eye is safe for prolonged exposure. The irradiance measured at the position of the eye does not exceed 0.15 mW/cm^2 , which is well below the maximum permissible exposure limits

according to the established American National Standards Institute Z-136 safety standards [Sli80].

The optical layout of the fixation system is illustrated in Figure 6.3. The fixation target is a flashing light in the center of the scanning circle, produced by a 690 nm laser diode (LD2) optically conjugate to the main 785 nm laser (LD1). As eyes do not accommodate well on monochromatic light, this blinking fixation light appears superimposed on the center of a white-light accommodative background. A computer-generated star field, drawing attention to the blinking light in the center, is chosen as background, which is displayed on a miniature LCD screen. An achromatic pair of lenses (LP), with each lens having a focal length of 100 mm, images the star field 1:1 in a plane that is about 0.75 D closer than the blinking fixation light to account for the longitudinal chromatic aberration of the eye [Fer05], bringing the near-infrared light in focus on the retina. A cold mirror (CM1) transmits the 690 nm central fixation light and reflects the image of the computer-generated background, optically superimposing them. Another cold mirror (CM2), forming the junction between RBS system and target system, transmits the light from the main 785 nm laser while reflecting the star field image and even a sufficient amount ($\sim 51\%$) of the 690 nm central fixation light.

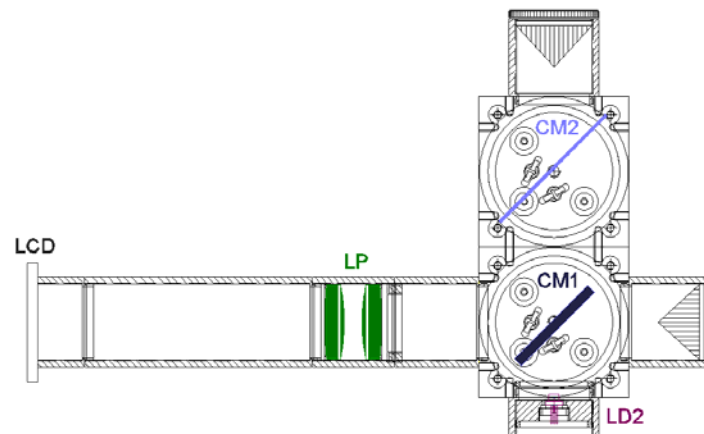


Figure 6.3: Opto-mechanical diagram of the target sub-system of the monocular eye fixation monitor (side view).

For data acquisition, subjects are seated in front of the device and are instructed to look through the center eyepiece with the examined eye while placing the forehead against the faceplate to simplify head positioning (see Figure 6.1). With the head positioned properly, the subject sees the blinking 690 nm fixation light through the eyepiece,

superimposed on the center of the star field, surrounded by the faint 785 nm scanning circle. Room lights are turned off to enhance pupil dilation, and thus to allow more light to enter the eye. A handheld pushbutton allows the subjects to initiate data acquisition themselves. As with the computer model, an epoch of 16 cycles is recorded during each measurement, so that with a motor speed of 40 Hz, a single measurement is obtained in less than half a second. To improve the signal-to-noise ratio with this monocular device, a preliminary measurement is obtained for each subject, with no eye in place. This background is digitally subtracted from subsequent data scans. The data are inspected online and stored to disk for offline analysis with custom software written for this purpose. The FFT power spectrum of the 16-cycle epoch is computed and displayed along with the signal traces, both the whole measurement (16 revolutions) and one revolution corresponding to the averaged waveform (averaging over all 16 cycles).

6.1.2 Method of Determining the Retardance and Fast Axis Orientation of a Wave Plate

Commercial retarders are usually specified for light in the visible spectrum, most commonly for yellow light having a wavelength of 589 nm. When the wave plate is to be used at a wavelength other than the manufacturer's specification, as is the case with our applications where the operating wavelength is 785 nm, the retarder may exhibit a significantly different, generally unknown, retardance. Also, while most purchased retarders are marked to indicate the fast axis' orientation, the axis is mostly uncertain for retarder film, which was preferred for the current assessment (explained later). Thus we wished to have a setup for measuring both fast axis and retardance of a wave plate.

Basically, the principle of the "crossed" polarizer method [Col03] was used for determining the fast axis (slow axis) of a retarder. In this method, as the name implies, the wave plate is inserted between two linear polarizers mounted in the "crossed" position, that is, the transmission axes of the generating polarizer and analyzing polarizer are in the horizontal and vertical directions, respectively. If there were no wave plate, no light would emerge through the pair of crossed polarizers, as should be the case when either the fast or slow axis is in the horizontal direction with the wave plate inserted. The direction of the retarder's axes can thus be determined by rotating the wave plate until a minimum intensity is observed behind the analyzer. Instead of using two polarizers in the crossed position, though, I used the simplified experimental setup from Figure 6.4 to determine axis and amount of birefringence, with only one polarizer, serving as an analyzer. To ensure that the laser is emitting light with the desired horizontal polarization orientation, the polarization

angle of the laser was rotated until the irradiance behind the polarizer (transmission axis in the vertical direction) was minimized.

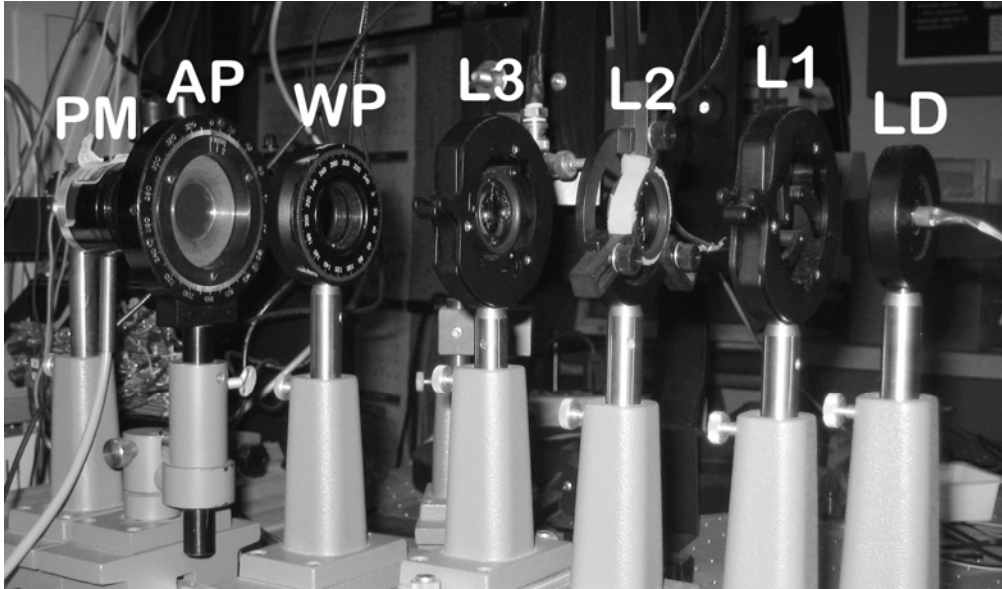


Figure 6.4: Photograph of the setup for determining axes and retardance of a wave plate. The divergent, linearly horizontal polarized light emitted by a 785 nm laser diode (LD) is collimated by a lens (L1). The collimated light passes through an inverted telescope, formed by a 50 mm f.l. lens (L2) and a 25.4 mm f.l. lens (L3), which narrows the beam. Light then travels through a wave plate (WP) and an analyzing polarizer (AP), before finally reaching a power meter (PM).

At this time, it is yet unknown which one of the located retardation axes is the fast axis and which is the slow. However, for the purpose of measuring the retardance of a wave plate, there is no need to differentiate between the two; 45 degrees away from either the slow or the fast axis, where the retarder is to be analyzed, the retardance value theoretically yields the same result. More precisely, the retarder is first rotated counterclockwise (as viewed along the propagation axis of the light, looking back toward the source) by 45 degrees from either axis to obtain maximum intensity. The intensity on the detector (I) of the transmitted light is then measured with the analyzer in each of the 0° and 90° orientations, and the retardance (δ) is calculated by:

$$\delta = \cos^{-1} \left(\frac{I(0^\circ, \delta) - I(90^\circ, \delta)}{I(0^\circ, \delta) + I(90^\circ, \delta)} \right) \quad (6.1)$$

In order to determine which of the previously located retardation axes is fast and which one is slow, another wave plate with known retardance and fast axis orientation was utilized. Based on Müller matrix calculus, the total retardance of a sequence of two wave plates is given by:

$$\delta_T = \cos^{-1}[\cos \delta_2 \cos \delta_1 - \sin \delta_2 \sin \delta_1 \cos 2(\theta_2 - \theta_1)] \quad (6.2)$$

where δ_T denotes the total retardance of a two-retarder combination with respective retardances δ_1 , δ_2 and respective fast axis orientations θ_1 , θ_2 . As can be seen, maximum retardance occurs when $\theta_2 - \theta_1$ is 0° , in other words when the fast axes of the two retarders are completely aligned with each other. In this case, the combined retardance is the sum of the individual retardances, $\delta_T = \delta_1 + \delta_2$. On the other hand, minimal retardance of the combination occurs when $\theta_2 - \theta_1$ is 90° , that is the fast axis of the first is aligned with the slow axis of the second wave plate. Total retardance is then the difference between the two individual retardances, $\delta_T = \delta_1 - \delta_2$.

Thus, a simple measurement of the total retardance with the reference wave plate, whose retardance and fast axis orientation are already known, helps to differentiate between the located but yet “unknown” retardation axes. Therefore, the reference retarder was inserted between the inverted telescope and the “unknown” wave plate, between L3 and WP in Figure 6.4, and their combined retardance was determined by means of the previously described procedure. If the measurement resulted in a combined retardance greater than that of the reference wave plate, the fast axis of the “unknown” wave plate was aligned with the fast axis of the reference retarder for the measurement. In other words, the located retardation axis was the fast axis. If the total retardance measured yielded a value smaller than that of the known reference retarder, however, the axis was the slow axis.

Using the same wave plate with known retardance and fast axis orientation, in fact a custom made 122° wave plate for 785 nm light (recently used in the retinal scanner for biometric purposes [Irs07]), the setup was verified to determine both properties within an accuracy of 2 degrees. This is more than sufficient for our purposes, considering that the rotation mount used in the validation setup is graduated in 2° increments.

6.1.3 Method of Determining Corneal Birefringence

Both the corneal retardance and the corneal azimuth of our subjects’ corneal birefringence had to be known in order to be able to compare the predicted results from the computer model with actual measurements. Individual corneal birefringence was measured with the

help of the GDx-VCC system (Carl Zeiss Meditec AG, Jena, Germany), available in our institution. As mentioned earlier, the GDx is a commercially available scanning laser polarimeter primarily used for glaucoma diagnosis purposes. The variable corneal compensator (VCC) version of the instrument features two identical wave plates in rotary mounts that allow measurement and individual neutralization of corneal birefringence.

Given that the examined eye has a normal macula with no pathology, the “bow-tie” method can be employed to measure individual corneal birefringence. Corneal birefringence is determined with the magnitude of the VCC set to zero as described before, in other words with the retarders in the “crossed” position. Macular polarimetry images obtained in this “crossed” position demonstrate a non-uniform retardation map with a distinct “bow-tie” pattern centered on the fovea, reflecting the retardation of the cornea superimposed onto the uniformly distributed retardation of the radial Henle fiber layer. The eye-specific corneal polarization axis can directly be determined from the orientation of the bow-tie, with the fast axis of corneal birefringence being aligned with the dark arms of the bow-tie, representing macular regions with minimal retardance. In contrast, the slow axis of corneal birefringence corresponds to the orientation where the bow-tie pattern is brightest, representing macular regions with maximal retardance. The magnitude of corneal birefringence is determined by analyzing the retardance profile on a circle around the fovea, with the slow and fast axes of corneal birefringence corresponding to the maximum and minimum values respectively. Corneal retardance can be computed by performing least-squares fit of the equation

$$\cos \delta_T = \cos \delta_R \cos \delta_C - \sin \delta_R \sin \delta_C \cos 2(\theta_R - \theta_C) \quad (6.3)$$

to the measured macular retardation profile. Note that this equation is the same as equation 6.2 from above, with the cornea and retina considered as two retarders in series.

Since the GDx-VCC measures the corneal slow axis (CSA), but our RBS computer model expects the corneal fast axis (CA), the following calculations have to be performed to match the corneal parameters in the model:

$$CA = CSA + 90^\circ \quad (6.4)$$

where for the right eyes, CSA corresponds to the negative value of the measured corneal slow axis.

6.2 Model Predictions with the Intermediate Eye Fixation Monitor

6.2.1 Influence of Varying Corneal Birefringence on the RBS Signal

To get a first impression on the overall performance of the intermediate eye fixation monitor in its present condition (with no fixed amount of double-pass birefringence added to the system), the influence of varying corneal birefringence on the RBS signal strength (FFT power at $2f$) obtained with the implemented “non-spinning” RBS design was assessed on the large Knighton/Gramatikov data set.

For the given design, RBS signal strength was computed for a range of corneal birefringence covering 0 to 180 nm CR, and 0 to 180° CA, as previously done. The results are displayed in Figure 6.5, in form of the familiar 3D-plot with the right and left eyes in the Knighton/Gramatikov data superimposed on its surface.

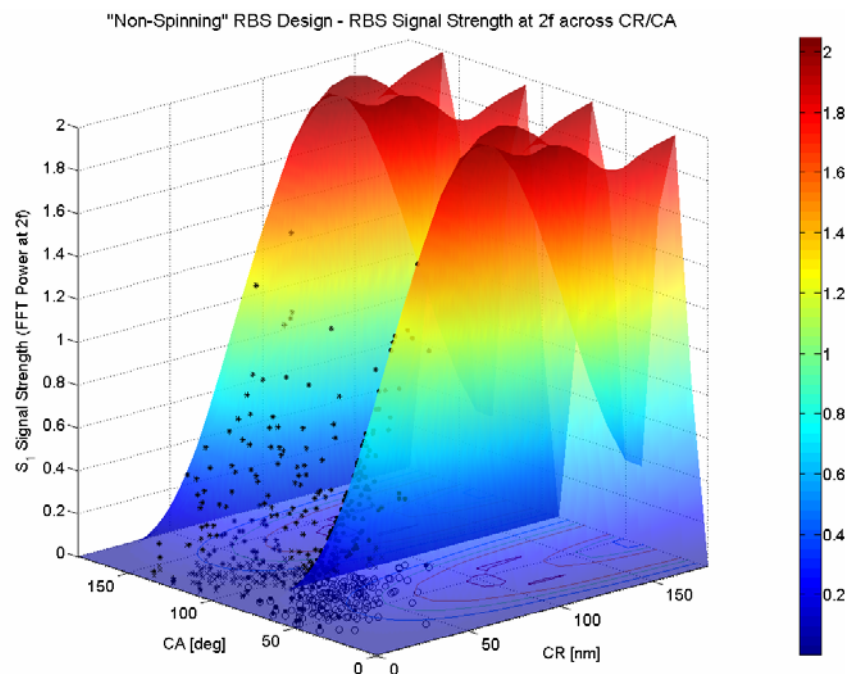


Figure 6.5: RBS signal strength at $2f$ (in relative power units) as a function of corneal retardance (CR) and corneal azimuth (CA) during simulated central fixation with computer modeling of the “non-spinning” RBS design implemented into the intermediate eye fixation monitor.

Similar to the spinning HWP design without any fixed amount of double-pass retardance added, the performance of the non-spinning RBS design is poor for eyes with very low corneal retardance and goes to zero when corneal retardance is zero. Moreover, for either eye, the signal falls off with low or high corneal azimuth. As shown in the contour plot, 204 of the representative eyes (102 of either eye), from the Knighton/Gramatikov data set of 300 eyes fall below the “0.4” contour. Therefore, with this threshold setting, 68% of the eyes in the data set are expected to yield only small signals with the intermediate eye fixation monitor.

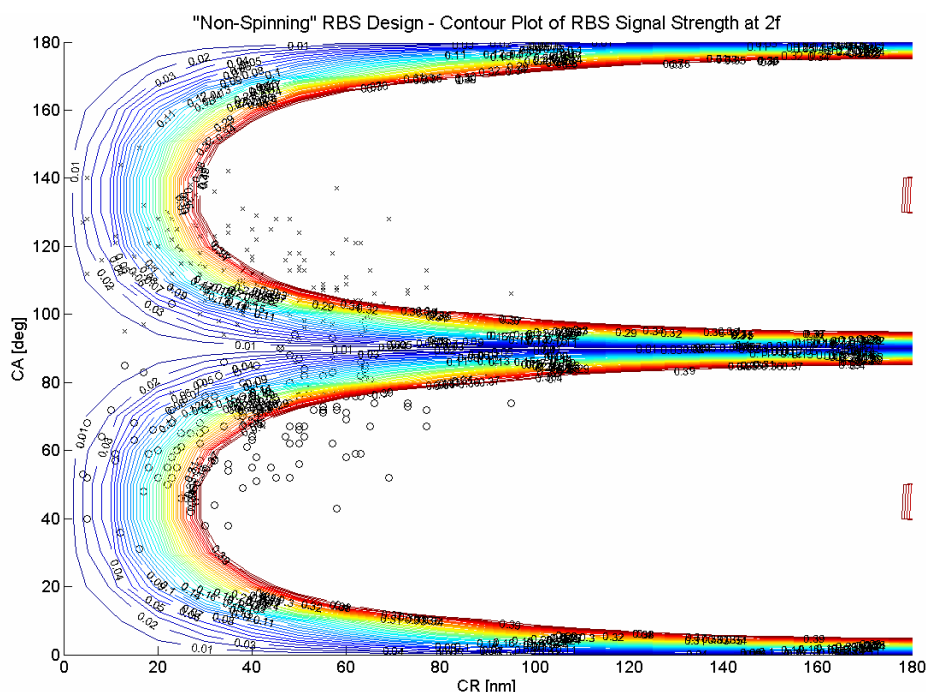


Figure 6.6: Contour plot of RBS signal strength at $2f$ (in relative power units) as a function of corneal retardance (CR) and corneal azimuth (CA) during simulated central fixation with model of the intermediate eye fixation monitor.

6.2.2 Optimizing Foveal Fixation Detection with the Intermediate Eye Fixation Monitor

As with the spinning HWP design, the poor performance for eyes with low corneal retardance begs for adding a fixed double-pass wave plate to the intermediate system. To find the retarder that would statistically optimize foveal fixation detection with the intermediate eye fixation monitor, preferably uniform over the population range of corneal

retardance and azimuth, we used the same optimization algorithm as described in Chapter 5.2.4.

Since the intermediate eye fixation monitor, due to its monocular nature, allows measurement of only one eye at a time, the optimization algorithm was applied to data for only one of the eyes in the Knighton/Gramatikov data set, using in fact the right eye data. The double-pass wave plate (WP) that statistically minimized the normalized standard deviation of RBS signal strength (FFT power at $2f$) for the 150 right eyes in the available data set was chosen to be the best retarder to implement for the monocular eye fixation monitor.

As shown in Figures 6.7 and 6.8 below, there are two local areas of minimal normalized standard deviation. With an incremental resolution of 10 degrees, the optimization algorithm measured an absolute minimum with a wave plate having a retardance of 60° and an azimuth of 140° .

Normalized Standard Deviation of RBS Signal Strength with "Non-Spinning" RBS Design - RE
(Incremental Resolution of 10 Deg)

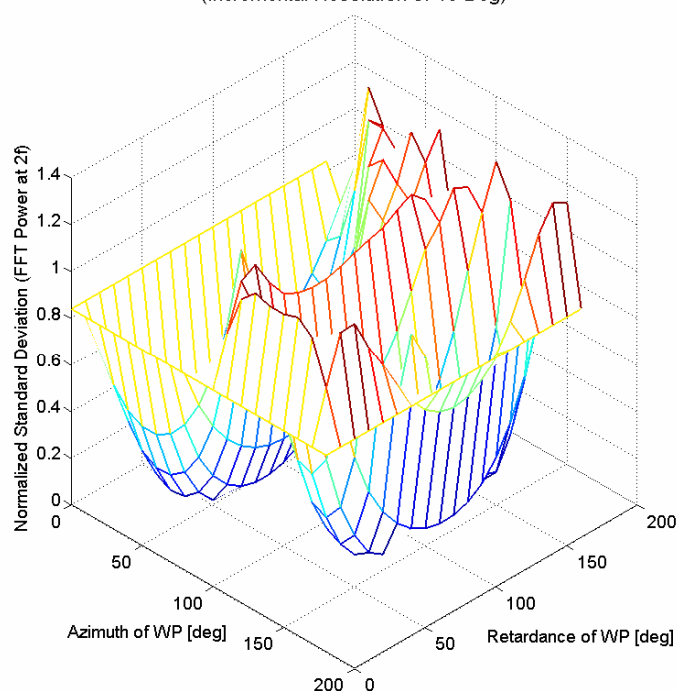


Figure 6.7: Normalized standard deviation of RBS signal strengths of the right eyes in the Knighton/Gramatikov data set as a function of retardance and azimuth (fast axis orientation) of the double-pass wave plate, during simulated central fixation with model

of the intermediate eye fixation monitor. Both retarder properties were varied with an incremental resolution of 10° .

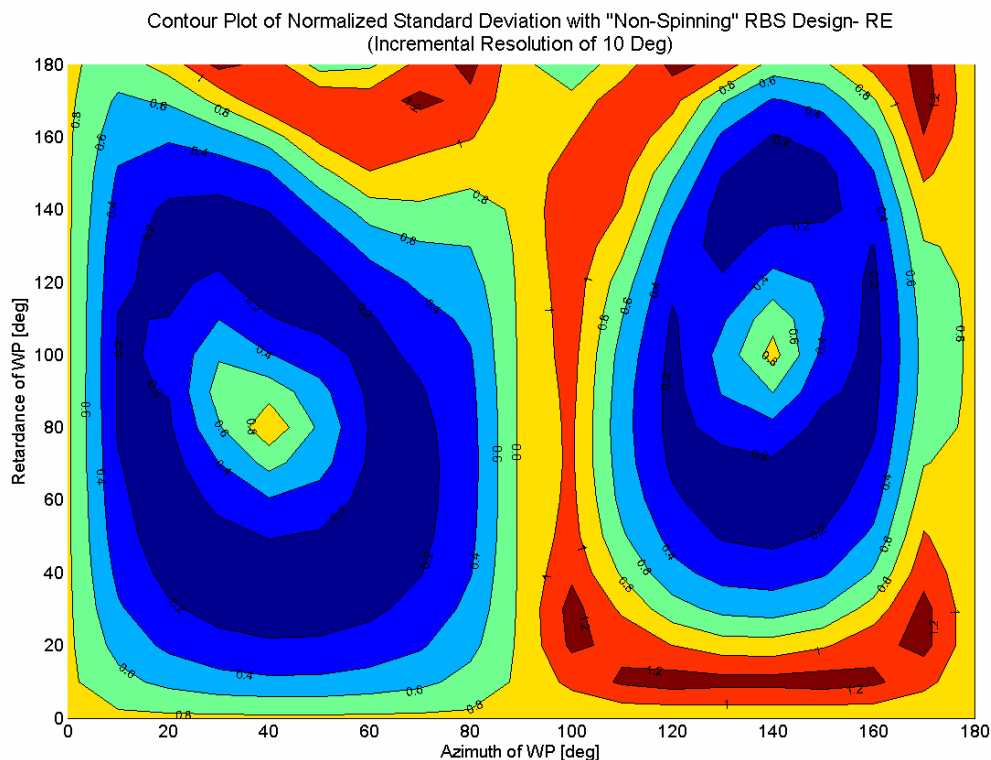


Figure 6.8: Contour plot of normalized standard deviation of RBS signal strengths of the right eyes in the Knighton/Gramatikov data set as a function of retardance and fast axis orientation of the double-pass wave plate, during simulated central fixation with model of the intermediate eye fixation monitor.

The algorithm was re-applied, varying the retarder properties on a finer grid covering the area adjacent to the absolute minimum (120° to 160° WP azimuth and 50° to 70° WP retardance), in increments of 1° and 2° for the retardance and fast axis orientation respectively (see Figures 6.9 and 6.10). An incremental resolution of 2° seemed reasonable for the azimuth of the WP, considering the 2° graduation of the WP rotation mount incorporated in the experimental validation setup. Maximal RBS signal strength with the least variance across the Knighton and Gramatikov's range of right eye corneal retardance and azimuths was achieved with a 61° wave plate with fast axis at 144° .

Normalized Standard Deviation of RBS Signal Strength with "Non-Spinning" RBS Design - RE
(Incremental Resolution of 2 Deg Azimuth and 1 Deg Retardance)

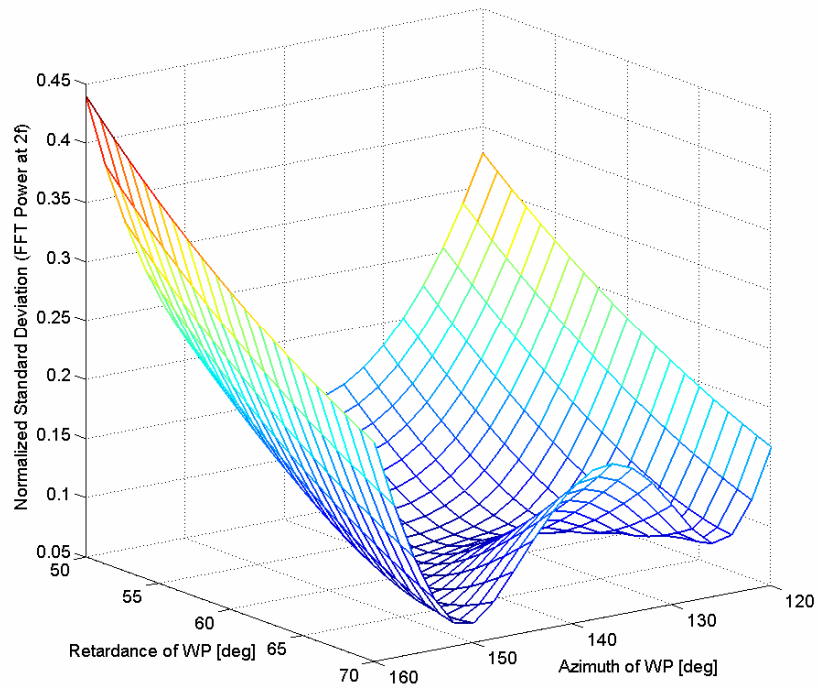


Figure 6.9: Normalized standard deviation of RBS signal strengths of the right eyes in the Knighton/Gramatikov data set as a function of retardance and azimuth (fast axis orientation) of the double-pass wave plate, during simulated central fixation with model of the intermediate eye fixation monitor. Retardance and azimuth of the wave plate were varied with an incremental resolution of 1° and 2° respectively.

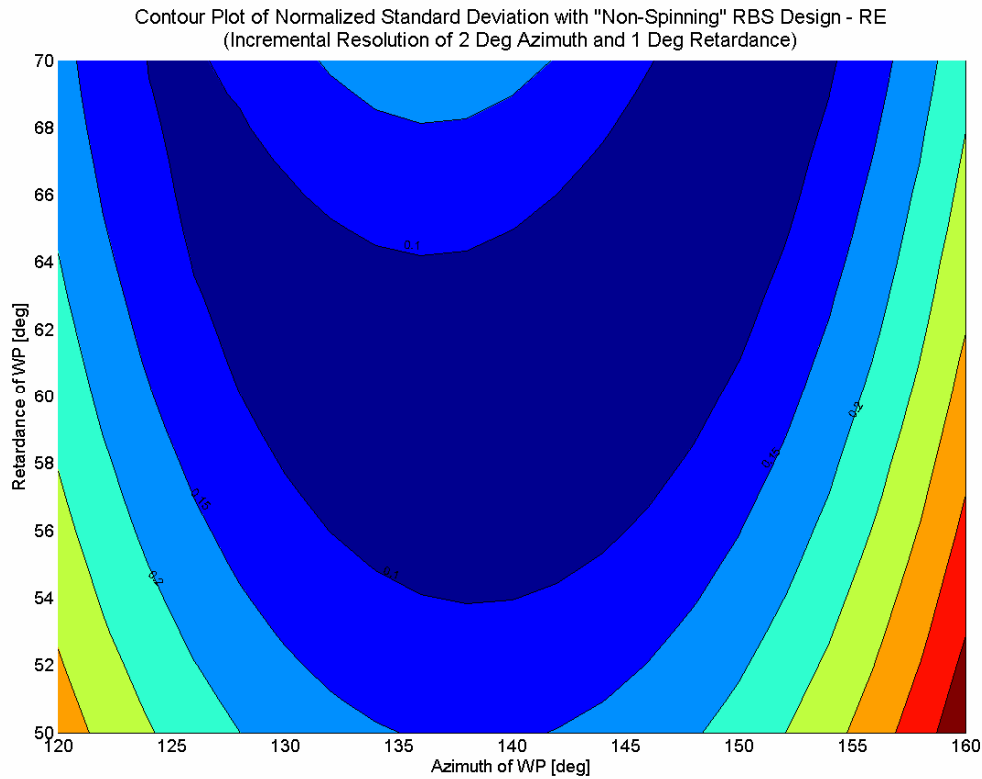


Figure 6.10: Contour plot of normalized standard deviation of RBS signal strengths of the right eyes in the Knighton/Gramatikov data set as a function of retardance and fast axis orientation of the double-pass wave plate, during simulated central fixation with model of the intermediate eye fixation monitor. Retardance and azimuth of the wave plate were varied with an incremental resolution of 1° and 2° respectively.

Adding a 61° wave plate to the non-spinning RBS design, operating on both incoming and returning path through the eye, theoretically improves foveal fixation detection with the intermediate monocular eye fixation monitor. Figure 6.11 shows that with the added wave plate at the fixed orientation of 144° (optimized for the right eyes), the RBS signal becomes very large for right eyes with low corneal retardance. RBS signal strength decreases slightly for right eyes with high corneal retardance, however, compared with the model predictions without the wave plate, the signal is practically uniform across Knighton and Gramatikov's range of right eye corneal retardances and azimuths in the population. The worse performance at higher values of CR makes little difference, because there was no right eye in Knighton and Gramatikov's data with a retardance above 100 nm. The contour plot reveals that none of the representative right eyes falls below the contour of 0.4.

"Non-Spinning" RBS Design with 61Deg-WP at 144 Deg - RBS Signal Strength at $2f$ across CR/CA

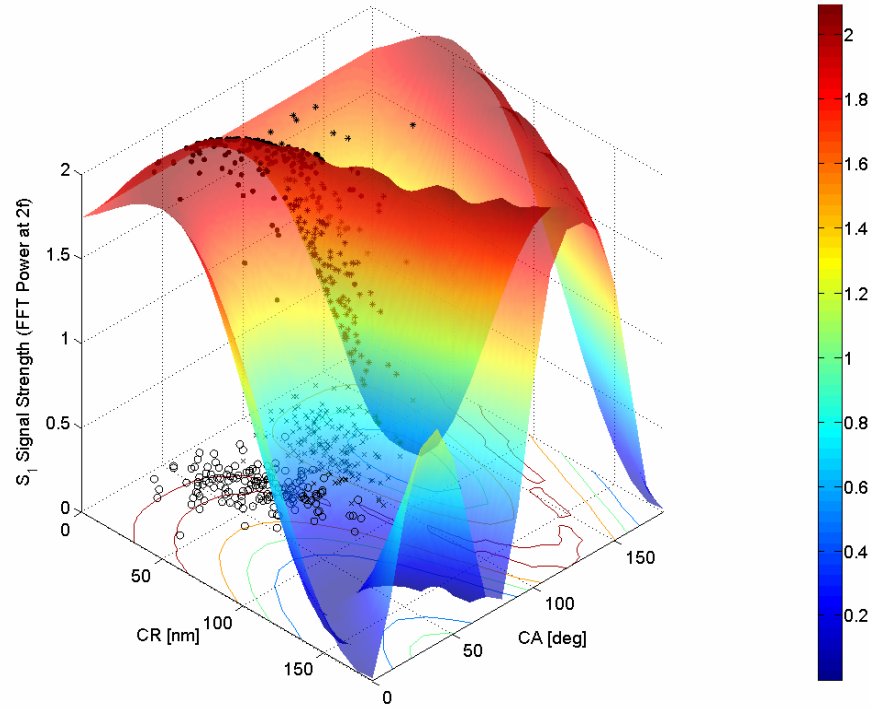


Figure 6.11: RBS signal strength at $2f$ (in relative power units) as a function of corneal retardance (CR) and corneal azimuth (CA) during simulated central fixation with computer model of the “non-spinning” RBS design after adding a double-pass 61° wave plate with fixed azimuth of 144° .

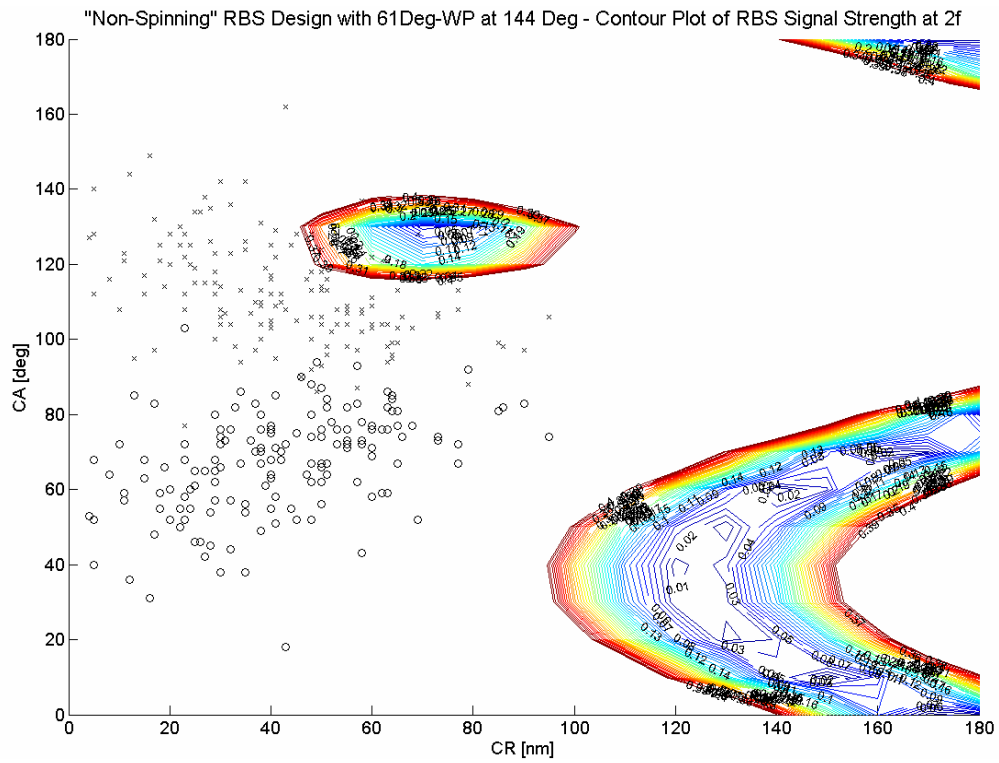


Figure 6.12: Contour plot of RBS signal strength at $2f$ (in relative power units) as a function of corneal retardance (CR) and corneal azimuth (CA) during simulated central fixation with computer model of the intermediate eye fixation monitor after adding a double-pass 61° wave plate with fixed azimuth of 144° .

6.3 Verification with Human Subjects

To compare RBS model predictions with actual measurements, 6 normal subjects (age 26 – 56) were recruited for the investigations, which were approved by The Johns Hopkins University Institutional Review Board and adhered to the tenets of the Declaration of Helsinki. Prior to the experiment, informed consent was obtained from all subjects after the nature and possible consequences of the study were explained.

Four of the six subjects had a refractive error of less than ± 2.00 D of sphere; one subject (2) was measured wearing contact lenses to compensate for 5.00 D of myopia. The intermediate eye fixation monitor was designed to function with up to ± 2.00 D of refractive error. One subject (3) had astigmatism of 1.50 D (right eye).

Knowing the individual corneal birefringence of the 6 test subjects is required for predicting their individual results obtained with the intermediate RBS system, and thus essential for direct comparison purposes between predicted and measured results. Thus, for all volunteers, individual corneal retardance and azimuth were measured with the GDx device as described above. Two macular polarimetry images were acquired for each subject, and the mean corneal retardance and azimuth were used for the analysis, as presented in Table 6.1.

Subject	Right Eye	
	CR [nm]	CA [deg]
1	33.7	77
2	27.3	50
3	22	74
4	29	58
5	37	70
6	27	77

Table 6.1: Measured corneal retardance (CR) and azimuth (CA) for right eyes of the subjects in this study.

6.3.1 Model Predictions for Studied Eyes

With both corneal retardance and corneal azimuth of our subjects known, the performance of the intermediate eye fixation monitor (in terms of strength of the foveal fixation signal) can be predicted for each right eye. To determine the predicted foveal fixation signal strength obtained with the intermediate eye fixation monitor, the measured values of

corneal retardance and azimuth from Table 6.1, for each subject, were inserted into the RBS model, which calculated the S_1 signal strength during simulated central fixation with the model of the intermediate eye fixation monitor, both with and without the added 61° wave plate oriented at 144° . The RBS model predicts that foveal fixation detection is greatly improved for each of the 6 studied right eyes after adding the fixed amount of 61° retardance (see Table 6.2).

Subject	Predicted FFT Power at $2f$	
	No WP	With WP
1	0.11	2.03
2	0.35	2.12
3	0.07	1.98
4	0.33	2.12
5	0.27	2.11
6	0.07	1.98

Table 6.2: Predicted strength of the RBS signal in relative power units during simulated central fixation with computer model of intermediate eye fixation monitor for the specific right eyes in the study, obtained both without (No WP) and with optimized 61° wave plate (With WP).

Finding optimum eye-specific fast axis orientation of the retarder

As another comparison measure, I also calculated the fast axis orientation for the given 61° wave plate that would statistically maximize RBS signal strength for each subject, using their measured combinations of CR and CA. Individual optimization was achieved by varying the azimuth of the wave plate from 0° to 180° in increments of 2 degrees, for the given retardance of 61° . For each azimuth, the FFT power at $2f$ was computed, and the azimuth with the highest number, that is maximal signal strength, was chosen to be the best orientation for the specific right eye. The results are given in Table 6.3.

Subject	Opt. WP Az. [deg]
1	62
2	70
3	64
4	68
5	66
6	64

Table 6.3: Individual optimized fast axis orientation for the given 61° wave plate (Opt. WP Az.) that yields maximal signal strength during simulated foveal fixation for each right eye of the volunteers in the study.

These results show that for our 6 test subjects a fast axis orientation of approximately 66° (average of Opt. WP Az. in Table 6.3) would theoretically be better suited for the right eye measurement with the intermediate monocular eye fixation monitor, which lies within the second suggested local area of minimal normalized standard deviation (see Figure 6.8). Recall that the optimization algorithm calculated two local areas of minimal normalized standard deviation for the given intermediate RBS design, with the absolute minimum occurring at 144° , which has been optimized for Knighton and Gramatikov's population range of right eye corneal birefringence (total of 150 right eyes). The modeling results with the wave plate oriented at 66° are shown in Figure 6.13 in form of the familiar 3D-plot.

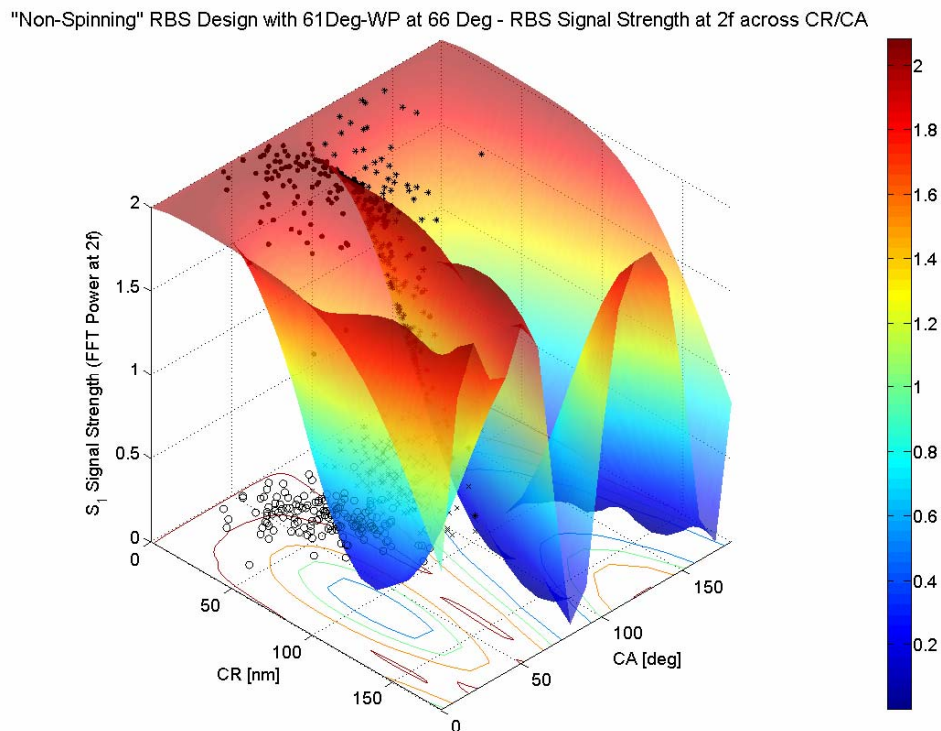


Figure 6.13: RBS signal strength at $2f$ (in relative power units) as a function of corneal retardance (CR) and corneal azimuth (CA) during simulated central fixation with model of the "non-spinning" RBS design after adding a double-pass 61° wave plate with fixed azimuth of 66° .

With the 61° wave plate oriented at 66° , the RBS signal becomes very large and uniform for right eyes with low corneal retardance, but falls off with higher values of CR.

Thus, considering the entire population range of right eye corneal birefringence (with the Knighton/Gramatikov data as reference), RBS signal strength is less uniform with the wave plate oriented at 66° than with 144° (see Figure 6.11). However, a fixed azimuth of 66° greatly enhances foveal fixation detection for the right eyes of our test subjects, whose the highest value of CR was only 37 nm (subject 5).

Figure 6.14 details, for one subject (#1), the predicted RBS signal strength at $2f$ as a function of fast axis orientation of the 61° wave plate. The individually-applied optimization algorithm in the computer model predicted an absolute maximum in FFT power at $2f$ with the fast axis orientated at 62° .

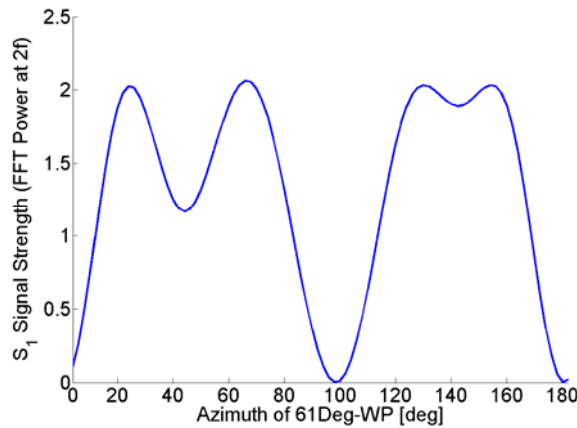


Figure 6.14: RBS signal strength at $2f$ (in relative power units) plotted as a function of fast axis orientation of the added 61° wave plate, for a given pair of right eye corneal retardance and azimuth (CR = 33.7 nm, CA = 77°) during simulated central fixation with computer model of the intermediate monocular eye fixation monitor.

6.3.2 Measured Data from Studied Eyes

To verify the predictions of the model with experimental data, the right eye of the 6 subjects was measured with the intermediate eye fixation monitor as indicated in 6.1.1. Subjects were asked to fixate centrally on the blinking target and press the trigger button to initiate data acquisition, maintaining fixation for about half a second until acquisition was complete. This procedure was performed both without and with a quarter wave film retarder (AX27341, Anchor Optics; Barrington, NJ) added to the double-pass system.

At our operating wavelength of 785 nm, this quarter wave plate, designed for 560 nm light, measured a retardance of 61° with the experimental setup described in 6.1.2. Retarder film was favored as source of a fixed amount of birefringence because it is thin

and thus minimizes beam deviation when switching the mode of operation between with and without wave plate. Another advantage of film retarders over other wave plates is that they are made of birefringent polymer, which compared with quartz is much less sensitive to changes in the angle of incidence. This behavior of polymer is vitally important, because the wave plate has to be tilted about 10 degrees to prevent light from being back-reflected into the optical system from its double-pass surfaces. A tilt of 10 degrees typically results in less than 1% change in retardance with a polymer retarder.

Measurements in the wave plate mode were first obtained with the retarder oriented at the position optimized for Knighton and Gramatikov's population range of corneal birefringence, i.e. at 144° . Next, data was acquired, for each subject, with the wave plate rotated to the individual optimized fast axis orientation from Table 6.3. The foveal fixation signal strength measured in each setting is presented in Table 6.4 (FFT power of the background-corrected fixation reading at twice the scanning frequency).

Subject	Measured FFT Power at $2f$ (<i>relative units</i>)		
	No WP	With WP	With WP at Opt. Az.
1	0.25	0.30	1.15
2	0.24	0.60	0.46
3	0.03	0.04	0.09
4	0.35	0.27	0.98
5	0.14	0.17	0.48
6	0.18	0.35	0.85

Table 6.4: RBS signal strength of right eyes of the subjects (in relative units), measured during central fixation with the intermediate eye fixation monitor, both without and with the 61° wave plate. The retarder was oriented at 144° first (With WP), before it was rotated to the predicted optimal position for each subject (With WP at Opt. Az.).

In addition, for one subject (#1) the 61° wave plate was manually rotated through 180 degrees in incremental steps of 10 degrees, and the strength of the foveal fixation signal at each incremental step was measured to experimentally determine the fast axis orientation that yielded maximal FFT power at $2f$. With an incremental resolution of 10 degrees, maximal signal strength was measured with the 61° wave plate oriented at 60° . Adjacent to 60° , the retarder was then rotated in 2° steps to find the absolute maximum. The maximal FFT power at $2f$ was measured with the wave plate oriented at azimuth 64° .

6.3.3 Comparison of Measured and Predicted Results

It can be seen from the measurement results above that for all subjects, except one (#4), the strength of the RBS signal during central fixation increased after adding the 61° wave plate oriented at 144° to the optical system, as predicted with the RBS computer model. Note that subject #4 already yielded a remarkably high foveal fixation signal without the wave plate, compared with the signal strength measured without the wave plate for the other tested right eyes, even higher than the foveal signal for subjects 1, 3, and 5 measured after the 61° wave plate has been added to the optical system.

In accordance with RBS model predictions, foveal signal strength is even further increased for the test subjects (except subject #2) with the wave plate oriented at the individually optimized azimuth. This confirms the hypothesis that for our small group of tested people, a fast axis orientation of about 66° is better suited for the right eye measurement with the monocular eye fixation monitor, significantly enhancing foveal fixation detection.

For subject #3, RBS signal strength is in general low, which might be explained by the astigmatism present in the subject's right eye, causing less useful light to return to the detector after the double-pass through the ocular system. The eye serves as an efficient retro-reflector only when the retina and the source of light are situated in conjugate planes, in other words with the eye being properly focused on the light source. This assumption is included in the RBS model, but it is certainly not valid for the astigmatic right eye of subject #3.

There are several potential factors contributing to deviations between measurements and model predictions. First, different head positioning during the assessment with the GDx instrument and the monocular eye fixation monitor could cause differences in measured and actually present corneal birefringence (especially corneal azimuth) during data acquisition with the intermediate eye fixation monitor.

Second, even though the retardance value of the 61° wave plate, as being made of birefringent polymer material, is negligibly affected by the 10° tilt minimizing specular back reflections, it still changes the retarder's fast axis azimuth slightly with respect to the beam reference system. In other words, the actual fast axis orientation will differ from the manually adjusted azimuth on the rotary mount, more precisely it will be shifted towards lower angles. This explains the observed deviation of 2 degrees between measured and predicted fast axis azimuth that yields maximal foveal signal strength for subject #1. The theoretically predicted value, 62° , was 2 degrees less than the measured result, 64° .

The major confounding factor, potentially resulting in inconsistent agreement between model predictions and measurement results, is non-uniformity of corneal birefringence across the pupil of real eyes. Such irregularity is certainly present in large pupils, which were induced during the assessment with the intermediate eye fixation monitor by turning off room lights to allow more light to enter the eye.

Because the optimized spinning half wave plate and fixed 1/8 wave plate RBS design theoretically gives strong signals across very wide ranges of corneal retardance and azimuth, wider than the known range of corneal birefringence for both eyes, variability in corneal birefringence across the pupil should not be as much of a confounding factor for the new Mark V PVS instrument.

Chapter 7

Pediatric Vision Screener – Mark V: Spinning PVS Design and Operation

Based on the modeling results, a revised Pediatric Vision Screener (PVS – Mark V) has been designed and is being constructed, implementing the optimized spinning HWP and fixed 1/8 wave plate RBS design binocularly, with the objective of measuring eye alignment essentially independently of corneal birefringence.

In anticipation that the PVS will be used as a vision screening tool for preverbal and preschool children at risk for amblyopia, additional design constraints were identified, as follows. In addition to binocular foveal fixation assessment, the device should simultaneously detect adequate focus of both eyes. Moreover, to allow remote assessment, the PVS must be hand-held and portable enough so that it can be aimed at children seated on a parent's lap without head restraint, and must have the ability to attract the child's attention.

In this chapter, the revised PVS is described in terms of the optical and mechanical design, and the anticipated principle of operation.

7.1 Optical Design

Figure 7.1 details the optical component layout and light paths of the Mark V Pediatric Vision Screener. Linearly polarized light emitted by the main 785 nm laser diode (LD1) passes through a pair of plano-convex lenses (LP1), each having a focal length of 75 mm, and is then transmitted by a plate polarizing beam splitter (PBS) toward a half wave plate (HWP) that is spun by a stepping motor using a pulley ratio to achieve a rotation 9/16 as fast as the scan. After passage through the rotating HWP, the beam of continuously rotating linearly polarized light passes through a 1/8 wave plate (WP) with fixed fast axis

vertical (90° azimuth). The light then enters the scanning unit consisting of two plane gold mirrors (M1 and M2), as implemented into the intermediate eye fixation monitor used for model validation purposes. The scanning unit is driven by the same stepping motor, thus turning the stationary beam of light into a circular scan. Light from the outer scanning mirror (M2) travels toward the eyes through a cold mirror (CM). While each eye is fixating, or focusing, on a blinking red light generated by a 690 nm laser diode (LD2) in the center of the scanning circle, each retina is scanned by the spot of laser light subtending an visual angle of 1.5° radius (3° in subtended diameter). The small portions of light reflected from the ocular fundi are re-imaged by the auto-conjugacy of the optical system back along the same path where they came. The unchanged part of the returning light, in other words the part with the same polarization as the original plane of polarization, is transmitted through the PBS, back toward the light source, thus never making it to the detection unit. The useful part of the returning light, on the other hand, is reflected by the polarizing beam splitter toward the photodetector assembly. A bandpass filter (780 ± 8 nm) (F) with a FWHM of (30 ± 8 nm) assures that only light in the desired wavelength range reaches the detectors. It is positioned between another pair of plano-convex lenses (LP2) to avoid shifting of the filter's peak transmission to shorter wavelengths, which can occur if used in convergent or divergent light. The lens pair images the spatially preserved signals from the right and left eyes, separated by a knife-edge reflecting prism conjugate to the plane of the pupils, toward the photodetectors (PD1 and PD2).

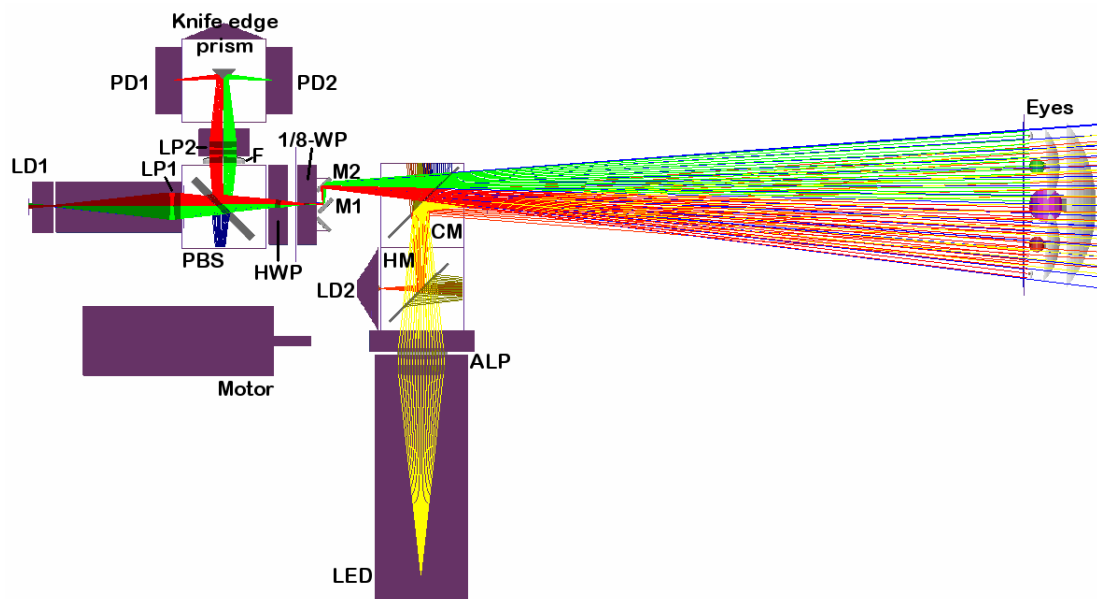


Figure 7.1: Ray tracing diagram and physical layout of the Mark V Pediatric Vision Screener.

As with the intermediate eye fixation monitor, the fixation target is a red light in the center of the scanning circle, which is flashing on and off to attract the child's attention. The fixation light is produced by the 690 nm laser diode (LD2) positioned optically conjugate to the main 785 nm laser (LD1). A black and white grid printed on a transparency serves as an accommodative target, which is illuminated by a white-light LED array. This white-light accommodative background is imaged 1:1 by an achromatic lens pair (APL) into an aerial image plane that is 33 cm away from the subject, a standard near testing distance for children. Greater distances in general cause young subjects to lose interest in the target. To account for the eye's longitudinal chromatic aberration, the image of the RBS spot of 785 nm light is optically conjugate to the 690 nm light source and is located 0.75 D farther away than the 33 cm distance of the accommodative grid target, at 44.4 cm. Thus, with an eye fixating on the blinking 690 nm light, with focus controlled by the black-and-white background grid at 33 cm, the near-infrared light from the scanning 785 nm laser diode will be in proper focus on the retina.

The accommodation control with the improved target system, and the use of the plane-mirror scanning system that avoids optical degradation of the double-pass image, enable the double-pass image of the RBS spot of light to be used simultaneously for alignment assessment and focus detection using the bull's-eye focus detector. This significantly simplifies the combination of both technologies in the Pediatric Vision Screener. Also the incorporation of the spinning HWP, which allows differential polarization detection with only one detector instead of two, significantly reduces the overall number of detectors to just one bull's-eye detector per eye. In contrast, the 2002 prototype instrument required six detectors in total, four for detection of the differential RBS signals, and two bull's-eye detectors for focus detection. The concept of both alignment and focus detection using a single bull's-eye photodetector per eye is detailed in the following section.

7.1.1 Alignment Detection

For each eye, if the scanned circle of 785 nm light is centered on the fovea, the differential polarization signal of the returning light has a frequency of predominately 2.5 times or, for certain eyes with high corneal retardance, 6.5 times the scanning frequency. For the Mark V PVS, the frequency of the scan is 30 Hz, so that a predominantly 75 Hz or 195 Hz signal from an eye indicates central fixation. Thus, frequency analysis of the signals representing the left and right eyes reveals whether a subject is fixating on the target with one eye, both eyes, or neither eye.

7.1.2 Focus Detection

While the state of fixation of each eye is a function of which frequency dominates the overall signal, the state of focus of an eye is dependent on the amount of light hitting the central versus annular areas of the bull's-eye detector. If the eye is in good focus on the accommodative background target at 33 cm, most of the returning 785 nm light will fall on the central detector, but if it is out of focus, light will fall on both the center and annulus detectors.

The “spinning artifact” frequency component in the signal at $4.5f$, i.e. at 135 Hz for the Mark V PVS, is relatively independent of the fixation condition of the eye and is thus nicely suited for independent assessment of the state of focus. Thus, the goodness of focus of each eye can be assessed by first computing the power spectrum of both the center (C) and annulus (A) signals, and then assessing the FFT powers at 135 Hz in the center and annulus signals via their ratio (C/A) or their normalized difference $[(C-A)/(C+A)]$.

7.1.3 Optical Components

Scanning laser

The main laser diode (LD1) is a 0.78 μm band GaAlAs laser diode with a multi-quantum well structure (HL7851G, Hitachi, Ltd; Tokyo, Japan), which has an output power of 50 mW (continuous wave) at the specified wavelength of 785 nm. A near-infrared wavelength was chosen to maximize spectral reflectance compared with visible wavelengths [Els96], [Zag02], and to overcome disadvantages caused by visible light, such as discomfort to the subject and reflex pupillary constriction, which would decrease signal power [Lop97].

Fixation laser

The 690 nm fixation target is a 0.68 μm AlGaInP laser diode with a multi-quantum well structure (HL6738MG, Hitachi, Ltd; Tokyo, Japan), delivering a 35 mW beam. To attract the child's attention, this fixation laser is operated in the blinking mode. The wavelength of 690 nm was selected for being, on the one hand, well outside the bandpass filter's transmission so as not to interfere with the detected signal from the scanning laser, and on the other hand, close enough to the wavelength of the scanning laser to minimize any problems from the eye's longitudinal chromatic aberration.

Scanner

To avoid optical aberration in the double-pass system introduced by a concave mirror, two plane mirrors (NT45-724, Edmund Optics, Inc.; Barrington, NJ) are used for the scanning unit. The mirrors are 10 x 10 mm square and have a protected gold coating, ideal for near-infrared light, with a $\frac{1}{4} \lambda$ flatness according to the manufacturer. Instead of being tilted 45° as is the inner mirror (M1), the outer mirror (M2) is tilted 45.75° , so that light enters the eye at an angle of 1.5° . The mirrors are mounted on a pulley having a large central aperture and are spun at 30 Hz by a drive belt from a stepping motor (CSK264-BT, Oriental Motor U.S.A. Corp.; Torrance, CA), thereby achieving a circular scan of approximately 3° in subtense at the subject's eye.

Bull's-eye photodetector

The photodetector assembly consists of two bull's-eye photodetectors (SSO-KP-6.28-3, Silicon Sensor GmbH; Berlin, Germany), one for each eye. The bull's-eye photodetector has two concentric active surfaces, a central circular area and a surrounding annulus, each with essentially the same total area (central area = 3.142 mm^2 ; annulus area = 3.127 mm^2). The outer diameter of the annular active area is 2.97 mm.

Wave plates

Key components of the new design are the spinning half wave plate (NH-050-0780) and the $1/8$ wave plate (N8-050-0785). Both retarders are true zero-order precision retarders from Meadowlark Optics, Inc. (Frederick, CO). Their polymer retarders are composed of a birefringent polymer material cemented between two precision polished, optically flat BK7 windows. Supported by index matching cement and a broadband antireflection coating, these assemblies promise transmittance of at least 97%. [Mea05].

7.2 Mechanical Realization

An interactive design process between the optical requirements and the mechanical constraints yielded the revised opto-mechanical apparatus. The information on the revised optical arrangement, including the required optical components, optimized using an optical ray tracing program for optical design and analysis (Optics Lab, Science Lab Software; Carlsbad, CA), was transferred to both AutoCAD (Autodesk; San Rafael, CA) and to SolidWorks (Dassault Systèmes S. A.; Suresnes, France), to create accurate 2- and 3-dimensional drawings of the Mark V Pediatric Vision Screener to facilitate construction of

the instrument in Dr. Guyton's home machine shop (Baltimore, MD). An accurate mechanical 3-D model of the PVS – Mark V, drafted with SolidWorks, and the resulting mechanical assembly, are shown in Figure 7.2.

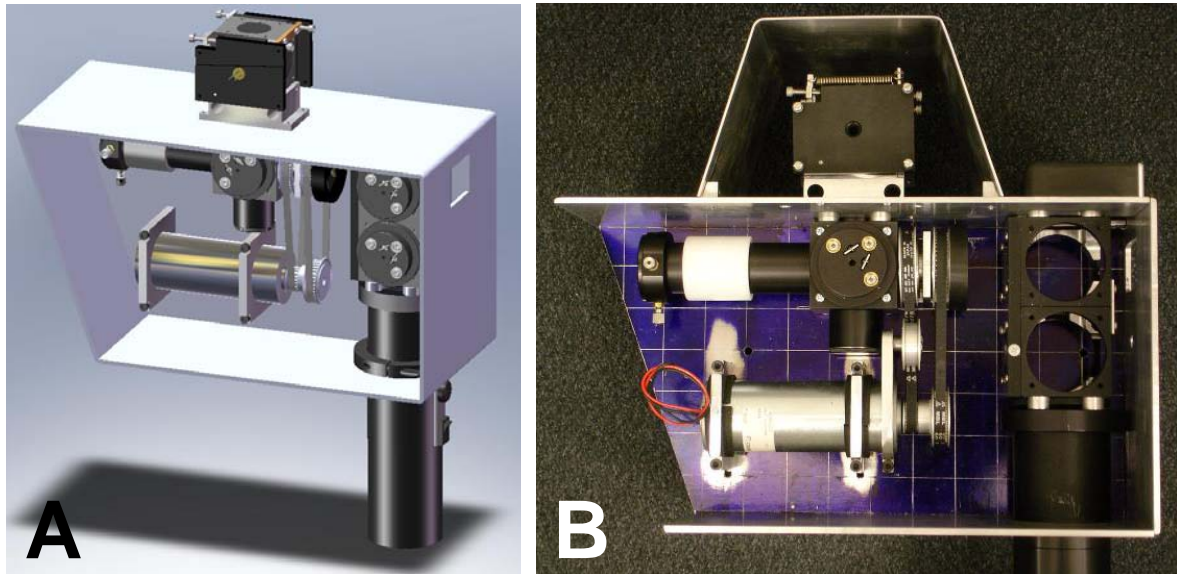


Figure 7.2: **A.** Mechanical model of the Mark V Pediatric Vision Screener. **B.** Photograph of the mechanical assembly for the Pediatric Vision Screener – Mark V.

7.2.1 Mechanical Components

Figure 7.3 illustrates the mechanical component layout of the Mark V Pediatric Vision Screener. Commercially available optical lens tube and cube systems from Thorlabs (Newton, NJ) provide a solid and stable housing for most of the optics. Their stackable precision-machined development kit provides flexibility for complex opto-mechanical assemblies. Black anodization of the components aids rejection of stray light. Several Thorlabs parts have been modified, and additional pieces have been designed and machined, to meet the special requirements of the optimized design.

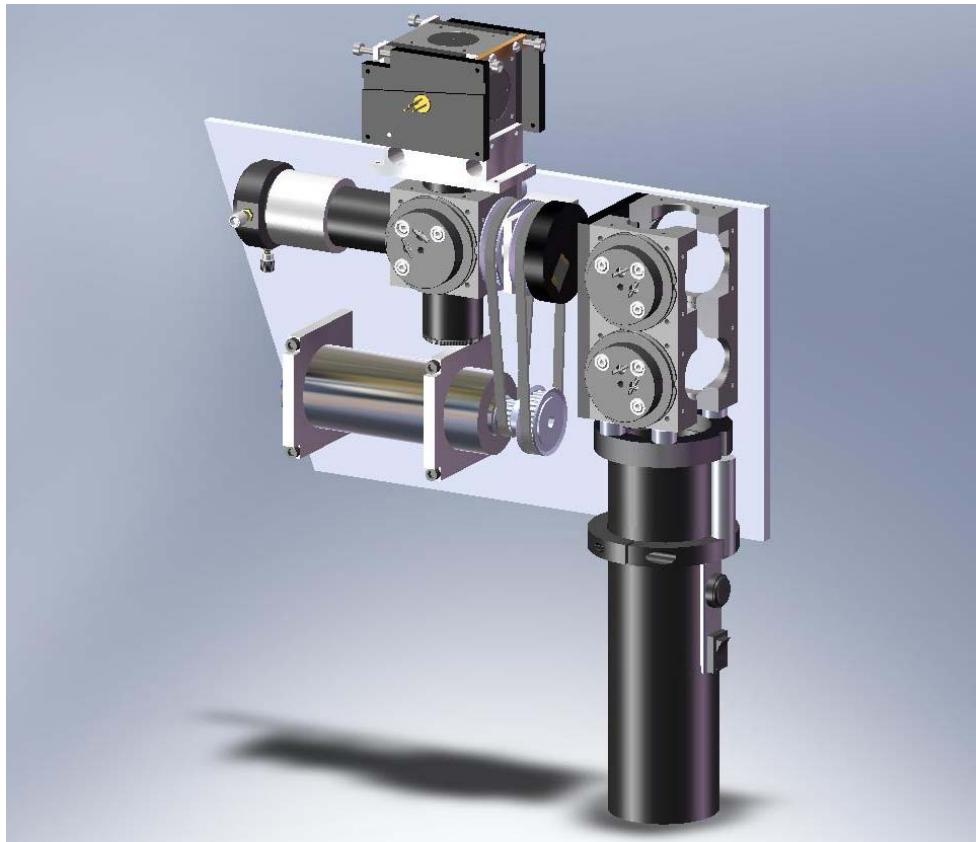


Figure 7.3: Mechanical component layout of the Mark V Pediatric Vision Screener.

X-Y translation photodetector mounting assembly

The bull's-eye photodetectors must be electrically isolated from the instrument's aluminum base and from each other. The detector platform was therefore made from a quarter-inch-sheet of black acetal plastic, in which a hole was lathe-cut to accommodate the can of the bull's-eye photodetector (see Figure 7.4). This holder is attached to another plate of aluminum with equal thickness by a small metal pin (see lower left-hand corner of the plastic mount in Figure 7.4). Independent rotation of the two plates, by means of two screws, about their points of attachment, allows fine x-y adjustment of the detectors, and thus facilitates x-y alignment of each photodetector with the laser source in their respective conjugate planes. A specially-designed spring system along with a twisted nylon cinch provides additional support (see Figure 7.4 C).

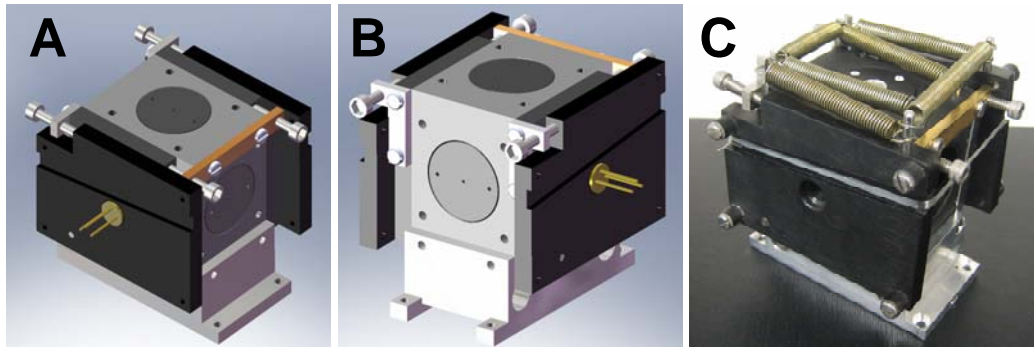


Figure 7.4: Photodetector mounting assembly. Note the two adjusting screws enabling x-y translation of each detector. A screw to the right-hand side, attached to a regular mounting cube from Thorlabs, allows manual rotation of both plates together (**A**), while a second screw attached to the aluminum plate enables counter-rotation of the plastic plate against the aluminum plate (**B**). A twisted nylon cinch and springs provide additional stability (**C**). The photodetector's printed circuit board with associated electronics is affixed to each plastic plate.

Motor

An industrial 24 V (DC) stepping motor (CSK264-BT, Oriental Motor U.S.A. Corp.; Torrance, CA) is employed to spin the scanning unit at 30 Hz (1800 rpm), advancing 1.8° per step (200 steps per revolution). A frequency of 30 Hz was selected because it is proportional to the power line frequency (60 Hz in the US), and thus will allow elimination of 60 Hz noise from the recorded signal by 360° -phase-shift subtraction. To avoid any discrepancy from the power line frequency, it is highly desirable to synchronize the motor speed with the power line frequency. Such synchronization is achieved with custom motor control hardware, by means of a PLL-based frequency multiplier.

Belt drive system

To run the half wave plate at a fractional frequency of the scan (9/16 times as fast), a special belt drive system is needed (see Figure 7.5). The HWP is mounted within a 44-tooth pulley (HTPA44S3M060, MISUMI USA, Inc.; Schaumburg, IL), so that it rotates together with the pulley. The scanning unit, a custom-made black acetal plastic piece holding the mirrors, is tightly fitted onto the edge of the outer ring of another 44-tooth pulley. Both pulleys are held in place by means of a custom holder machined from aluminum. The $1/8$ wave plate with fixed azimuth of 90° is mounted within this holder, so that it remains stable. To realize the 9 to 16 rotation requirements of the HWP and scanning unit respectively in the optimized design, the implemented belt drive system employs a pulley with 18 teeth (HTPA16S3M060) to drive the HWP, and one with 32 teeth

(HTPA32S3M060) to drive the scanning unit. The ratio of 18 to 32 equals 9/16, as required.

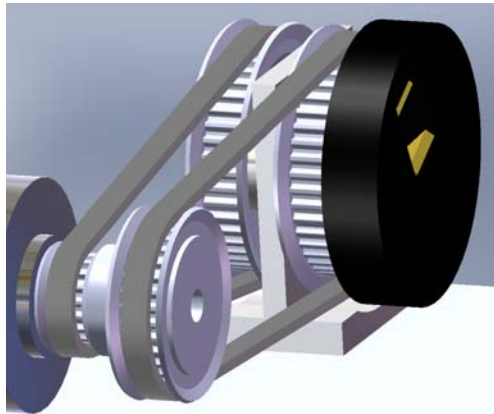


Figure 7.5: Belt drive system. Note special pulley/belt configuration, transmitting different speeds to the HWP, mounted within the back left-hand pulley, and to the scanning unit, the black plastic disk attached to the back right-hand pulley.

7.3 Device Operation – Outlook

A pictorial illustration of the device operation is given in Figures 7.6 and 7.7. The hand-held configuration of the PVS will allow remote examination of a child, without head restraint. The child can be seated on a chair or in the parent's lap, while the operator aims and adjusts the vision screener properly. A laser diode range finder enables quick and easy adjustment of the proper working distance of 33 cm (see Figure 7.6). This desired axial distance is achieved when the two laser spots overlap on the bridge of the child's nose. During the exam, the child is asked to watch the blinking light within the aperture of the apparatus (see Figure 7.7). The flashing fixation target will be presented in combination with a beeping tone to prevent the child from losing interest in the device. Room lights will be dimmed to further enhance interest in the target, as well as aid in pupil dilation to increase the amount of light entering the eyes.

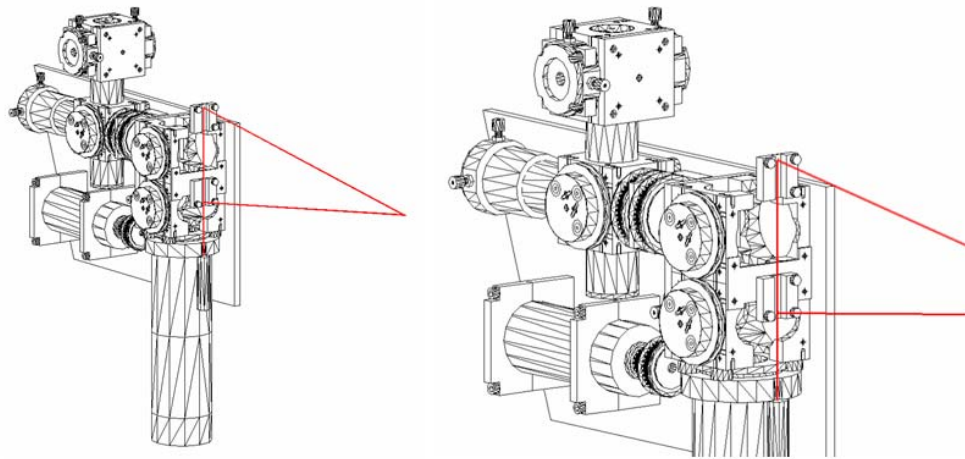


Figure 7.6: Mechanical component draft of the Mark V Pediatric Vision Screener. Note hand-held configuration of the device and triangulation range finder that enable remote examination. The infant can be seated on a parent's lap, for instance, while the operator aims and adjusts the screener properly with the help of the laser diode range finder. Axial distance is correct when the two laser spots overlap on the bridge of the child's nose.

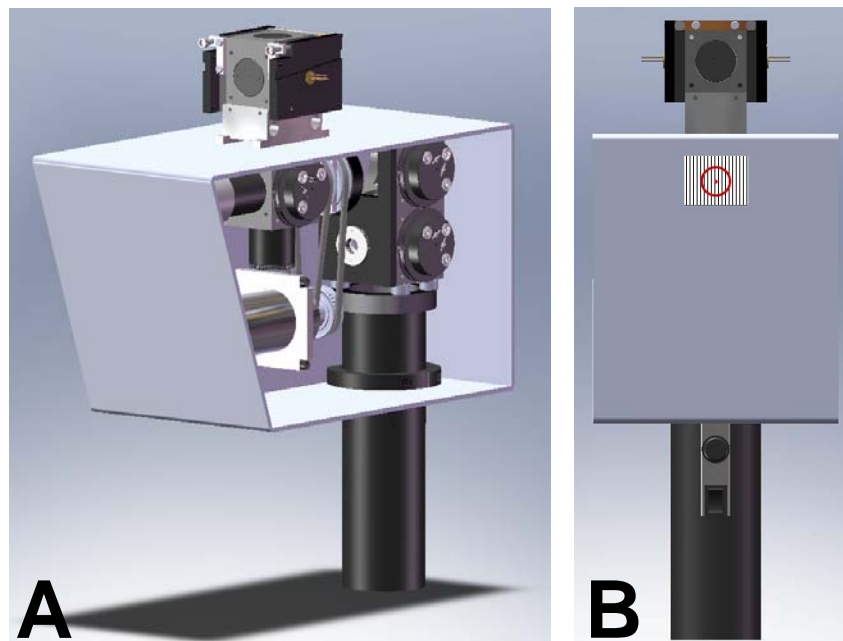


Figure 7.7: The Pediatric Vision Screener – Mark V is illustrated in two views. **A.** Oblique view of entire device from operator's side helping to show mechanical component layout. **B.** Child's view of white-light fixation grid with blinking fixation target (690 nm) in the center, surrounded by scanning circle (785 nm).

The device will be connected to a “lunch box” data acquisition computer for the initial phase of testing. Custom software will be written by us in C language (CVI, National Instruments). Data acquisition can be initiated by the operator by simply pushing the upper trigger button at the front of the handle (see Figure 7.7 B). We intend to obtain a single reading (epoch of 17 cycles) in approximately half a second, as with the intermediate eye fixation monitor. At least 17 cycles must be acquired to obtain the differential polarization signal, which is calculated by digitally shifting and then subtracting the signal by one cycle (360°-phase-shift subtraction). The Fast Fourier Transform (FFT) power spectrum will be computed on the resultant 16-cycle differential signal.

To assess the goodness of eye alignment, the FFT power spectrum will be displayed as separate plots for the right and left eye. For focus assessment, only the powers at 135 Hz (4.5f) is of interest, which will be displayed as a pair of peaks for each eye, representing the center (C) and the annulus (A) signals from the bull’s-eye photodetector. In anticipation that the PVS will be used as a screening tool administered by lay personnel, we intend to add an additional array of four red/green LEDs on the outer case of the device facing the operator, controlled by the software, to additionally display the findings in the form of pass/refer (fail) indicator lights.

Chapter 8

Discussion

The computer-model-optimized RBS design developed in this thesis, incorporating a double-pass half wave plate spinning 9/16 as fast as the circular scan, and a double-pass 1/8 wave plate at a fixed azimuth of 90° , enables differential retinal-birefringence-based detection of foveal fixation with only one detector, essentially independently of corneal birefringence.

Differential foveal fixation detection with only one detector, easing constraints on optical alignment and balancing, is achieved by incorporation of the half wave plate spinning at a particular fraction of the scan frequency. The differential polarization signal is calculated digitally by means of 360° -phase-shift subtraction. By spinning the half wave plate 9/16 as fast as the circular scan, strong “multiple-of-half”-frequency RBS signals are generated that double in amplitude and even quadruple in signal strength, i.e. FFT power, whereas much of the background noise is eliminated with differential subtraction, thus increasing the signal-to-noise ratio in retinal birefringence scanning.

Adding a 1/8 wave plate at a fixed azimuth of 90° to the optical system allows detection of the differential foveal fixation signal essentially independently of various corneal retardances and azimuths, yielding high differential RBS signals across the entire known population range of corneal birefringence.

The main advantage of retinal birefringence-based detection of eye fixation over other methods, such as scleral search coils, EOG, and video-based eye trackers, is that it does not require eye-gaze calibration. By detecting the radial symmetry of foveal architecture, RBS directly assesses true foveal fixation of the eye. The key to the effectiveness of RBS is the characteristic frequency appearing in the differential polarization signal derived from the retina when the circular scan is exactly centered on the fovea, indicating central fixation.

This ability to assess foveal fixation directly without any need for calibration makes it possible to investigate less cooperative subjects, including young children and infants at risk for developing amblyopia, which is the leading medical cause of decreased vision in childhood. Binocular retinal birefringence scanning, employing the new computer-model-optimized optical arrangement, has the potential for automatic and reliable screening of infants and young children for misalignment of the eyes (strabismus), the most common cause of amblyopia. Currently available photoscreeners can only detect strabismus indirectly and inaccurately via assessment of the positions of the corneal light reflexes.

The assumptions used in developing the RBS computer model, as well as some limitations of the RBS computer model, should be discussed. First, the ocular fundus is assumed to act as an ideal retro-reflecting surface, modeled by the Müller matrix of an ideal mirror. However, in real eyes only a small portion of the light incident on the retina is reflected (about 1/10,000 to 1/1000 of the light is reflected) [Guy00], which varies across individuals. The proposed Mark V Pediatric Vision Screener, incorporating the computer-optimized RBS design, will account for such intensity variation caused by different fundus reflectivities, as well as by different pupil sizes, varying light levels, etc. by applying normalization using the “spinning artifact” signal, the $4.5f$ signal that results purely from the HWP rotation, and which is practically independent of the state of eye fixation.

Another potential source of error includes the assumption that the cornea, which should be treated as a biaxial crystal with anisotropy in three directions, can be modeled as linear retarder with a uniform birefringence. This approximation appears reasonable for the central cornea, but with large pupils corneal birefringence certainly becomes non-uniform. Such irregularity across the pupil should not be as much of a confounding factor for the new optimized spinning half wave plate and fixed $1/8$ wave plate RBS design as for the intermediate monocular design used for validation purposes, because the spinning RBS design yields strong signals over more than the entire known range of corneal birefringence for both eyes.

Despite the potential sources of errors, the validation experiments with human subjects using an intermediate monocular RBS-based eye fixation monitor showed that the RBS computer model is capable of assessing the influence of corneal birefringence on the strength of the differential RBS signal during foveal fixation. Assessment of performance of the optimization algorithm applied to the intermediate RBS design confirmed its ability to find the appropriate double-pass birefringence which added to the optical system improves RBS signal strength during central fixation. This technique enhances recognition of foveal fixation by maximizing the signal from retinal birefringence across the available population range of corneal retardance and azimuth.

In conclusion, the presented spinning HWP and fixed 1/8 wave plate design greatly enhances foveal fixation detection while bypassing the deleterious effects of corneal birefringence in retinal birefringence scanning. Combining a binocular eye fixation monitor based on this computer-model-optimized RBS design with bull's-eye focus detection promises to be both robust and sensitive in screening infants automatically and reliably for both of the primary causes of amblyopia: strabismus and defocus.

Future studies will determine the performance of the proposed Mark V Pediatric Vision Screener, incorporating both alignment and focus-detection techniques in a single hand-held device, as an effective and sensitive screening instrument to automatically identify infants at risk for amblyopia, meriting universal application for pediatric vision screening. Such a robust device will allow earlier detection of amblyopia and thus prevent millions of children from life-long disability from this readily treatable cause of decreased vision.

Appendix

Spatial Dependency of the RBS Signal

To assess the spatial dependency of the RBS signal, FFT power at the frequency of interest was calculated for a fixed pair of corneal retardance and azimuth, more precisely for an average right eye ($CR = 30 \text{ nm}$, $CA = 70^\circ$), while changing the center of the circular scan in increments of 0.5 degree of visual angle on a grid covering -3 to $+3$ degrees in both the horizontal and vertical direction (measured from the foveal center). With the scanning circle being decentered from the foveal center, that is, with paracentral fixation, the retina cannot be considered as a rotating 7° wave plate any longer with the same amount of retardance being experienced at each scanning position and the azimuth of foveal birefringence rotating through 360 degrees. Both foveal retardance and fast axis orientation change depending on the momentary scanning position. The retina is still modeled as a linear retarder, mathematically described by the Müller matrix given in equation (3.19), but for each incremental position during the 360° scan, the fast axis orientation and retardance value are calculated according to equations (5.5) and (5.6), respectively.

The spatial representation of RBS signal strength at the two centered frequencies ($2.5f$ and $6.5f$), indicating foveal fixation with the optimized spinning half wave plate and fixed $1/8$ wave plate design, is depicted in Figure A.1. As to be expected, a definite maximum can be seen at the foveal center (0,0). The base of the cone has a diameter of roughly 2 degrees, permitting detection of foveal fixation with an accuracy of at least $\pm 1^\circ$. This is in accordance with studies conducted with our previous instruments. With the optimized spinning-HWP RBS design presented here, better levels of precision can be achieved easily with a higher threshold setting, something not feasible with the prototype PVS design due to the low signal levels obtained with the latter (see Figure A.2).

Spinning HWP and Fixed 1/8-WP Design - XY Plot of RBS Signal Strength at $2.5f$ & $6.5f$ after 360deg-Phase-Shift Subtraction

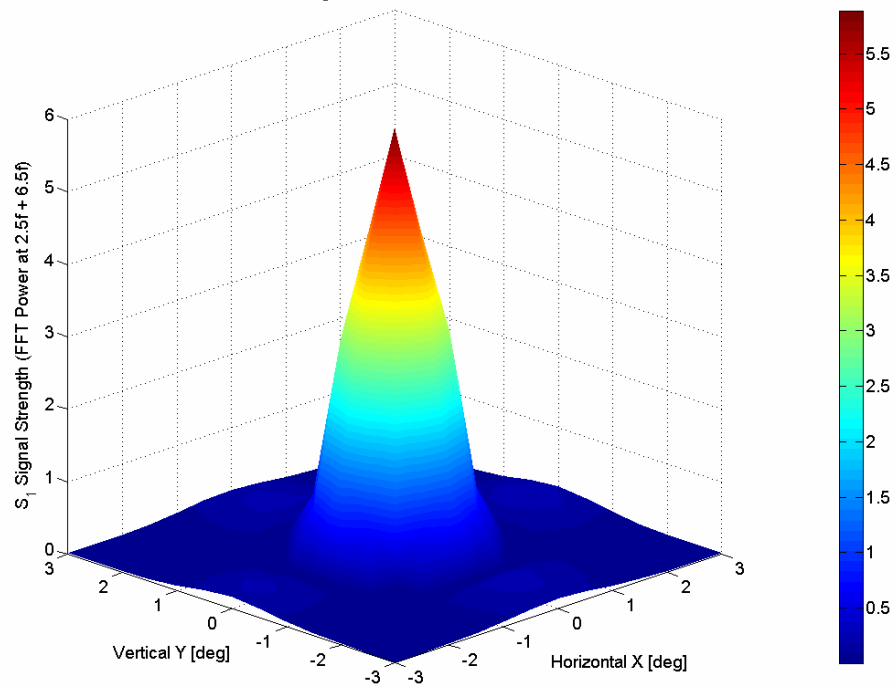


Figure A.1: RBS signal strength at the two frequencies indicating central fixation ($2.5f$ and $6.5f$) in relative power units with computer model of the optimized RBS design after 360°-phase-shift subtraction as a function of the distance from the foveal origin, with the distance being expressed in degrees of visual angle.

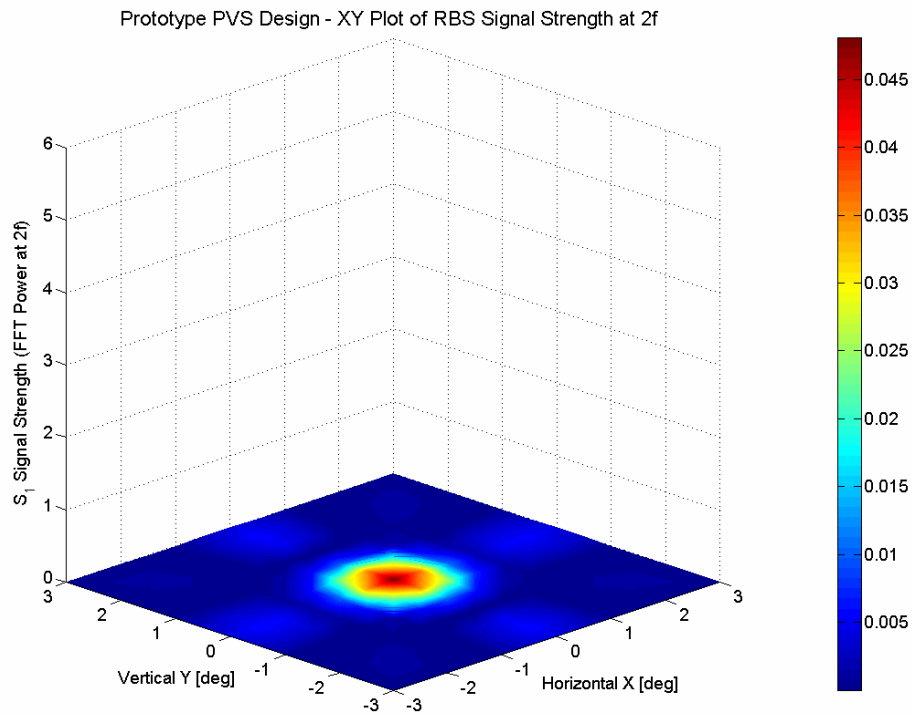


Figure A.2: RBS signal strength at $2f$ in relative power units with computer model of the 2002 prototype PVS design as a function of the distance from the foveal origin, with the distance being expressed in degrees of visual angle.

The RBS signal at $4.5f$, that is, the spinning artifact, on the other hand, is relatively independent of fixation. As shown in Figure A.3, the spatial distribution of RBS signal strength at $4.5f$ is essentially uniform with decentration, yielding a very large signal across the whole considered range of decentration (± 3 degrees in both the horizontal and vertical direction). The $4.5f$ signal can therefore fortuitously be used for focus detection purpose, as well as for normalization purposes. The latter is necessary to compensate for different fundus reflectivities, different pupil sizes, varying light levels or dust on the optics over time.

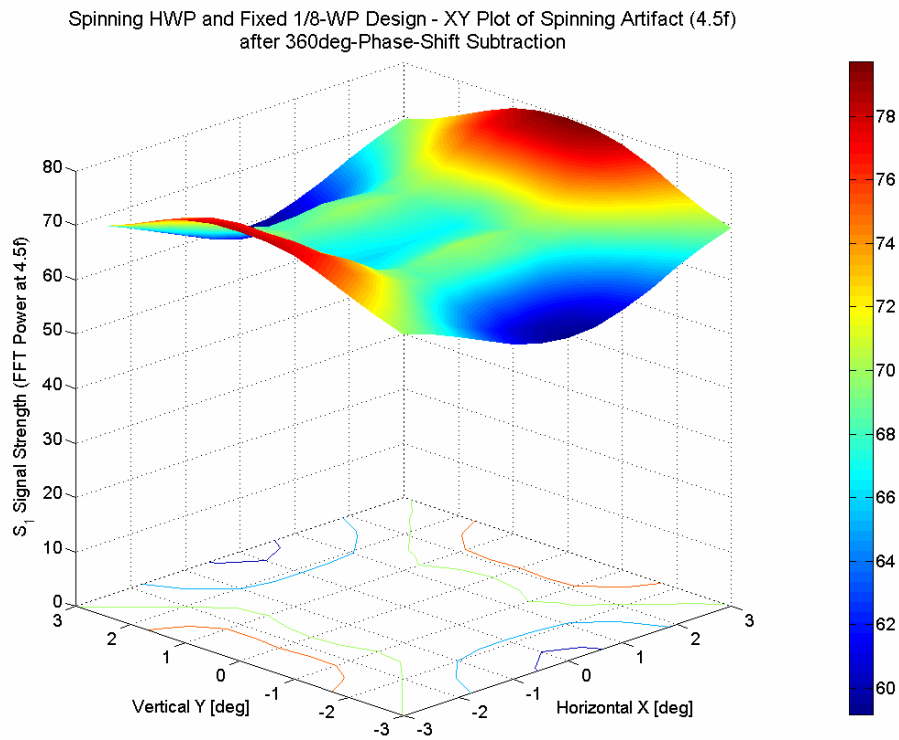


Figure A.3: RBS signal strength at $4.5f$ (spinning artifact) in relative power units with computer model of the optimized RBS design after 360° -phase-shift subtraction as a function of displacement from the foveal center.

References

- [Abr03] M. Abrahamsson, J. Ohlsson, M. Björndahl, and H. Abrahamsson, “Clinical evaluation of an eccentric infrared photorefractor: the PowerRefractor,” *Acta Ophthalmol Scand* **81**, 605–610 (2003).
- [Ach03] B. R. Acharya, C. K. Madsen, K. W. Baldwin, R. A. MacHarrie, J. A. Rogers, L. Möller, C. C. Huang, and R. Pindak, “In-line liquid-crystal microcell polarimeter for high-speed polarization analysis,” *Optics Letters* **28**(13), 1096–1098 (2003).
- [Ago08] M. Agopov, B. I. Gramatikov, Y.-K. Wu, K. Irsch, and D. L. Guyton, “Use of retinal nerve fiber layer birefringence as an addition to absorption in retinal scanning for biometric purposes,” *Appl Opt* **47**(8), 1048–1053 (2008).
- [Bet75] F. Bettelheim, “On optical anisotropy of the lens fiber cells,” *Exp Eye Res* **21**, 231–234 (1975).
- [Blo85] G. J. Blokland, “Ellipsometry of the human retina in vivo: preservation of polarization,” *J Opt Soc Am A* **2**, 72–75 (1985).
- [Bon07] R. A. Bone and G. Draper, “Optical anisotropy of the human cornea determined with a polarizing microscope,” *Appl Opt* **46**(34), 8351–8357 (2007).
- [Bor97] A. J. Born, R. C. Tripathi, and B. J. Tripathi, *Wolff’s Anatomy of the Eye and Orbit*, 8th ed., Chapman & Hall Medical, London (1997).
- [Bor99] M. Born and E. Wolf, *Principles of Optics*, 7th ed., Cambridge University Press, Cambridge (1999).
- [Bou91] L. J. Bour, “Polarized light and the eye,” in *Visual Optics and Instrumentation* (ed W. N. Charman), CRC Press Inc, Macmillan, New York, 310–325 (1991).
- [Bow07] C. Bowd, I. M. Tavares, F. A. Medeiros, L. M. Zangwill, P. A. Sample, and R. N. Weinreb, “Retinal nerve fiber layer thickness and visual sensitivity

- using scanning laser polarimetry with variable and enhanced corneal compensation,” *Ophthalmology* **114**, 1259–1265 (2007).
- [Bro98] C. Brosseau, *Fundamentals of Polarized Light: A Statistical Optics Approach*, Wiley-Interscience, New York (1998).
- [Cav07] L. A. Cuvuto, X.-R. Huang, and R. W. Knighton, “Corneal birefringence mapped by scanning laser polarimetry,” *Invest Ophthalmol Vis Sci* **48**, ARVO E-Abstract 3532 (2007).
- [Cog41] C. D. Gogan, “Some ocular phenomena produced with polarized light,” *Arch Ophthalmol* **25**, 391–400 (1941).
- [Col75] H. Collewyn, F. van der Mark, and T. C. Jansen, “Precise recording of human eye movements,” *Vision* **15**, 447–450 (1975).
- [Col93] E. Collet, *Polarized Light, Fundamentals and Applications*, Marcel Dekker, New York (1993).
- [Cop78] W. Cope, M. Wolbarsht, and B. Yamanashi, “The corneal polarization cross,” *J Opt Soc Am* **68**, 1139–1140 (1978).
- [Dav84] H. Davson, *The Eye. Volume 1a*, 3rd ed., Academic Press, Orlando, 1–64 (1984).
- [Dil77] F. H. Dill and P. S. Hauge, “Rotating-compensator ellipsometer,” U.S. Patent No. 4,053,232 (1977).
- [Don95] D. J. Donohue, B. J. Stoyanov, R. L. McCally, and R. A. Farrell, “Numerical modeling of the cornea’s lamellar structure and birefringence properties,” *J Opt Soc Am A* **12**, 1425–1438 (1995).
- [Don96] D. Donohue, B. Stoyanov, R. McCally, and R. Farrell, “A numerical test of the normal incidence uniaxial model of corneal birefringence,” *Cornea* **15**, 278–285 (1996).
- [Don00] S. P. Donohue, T. M. Johnson, and T. C. Leonard-Martin, “Screening for amblyogenic factors using a volunteer lay network and the MTI photoscreener. Initial results from 15,000 preschool children in a statewide effort,” *Ophthalmology* **107**, 1637–1644 (2000).
- [Don02] S. P. Donohue, T. J. Johnson, W. Ottar, and W. E. Scott, “Sensitivity of photoscreening to detect high-magnitude amblyogenic factors,” *J AAPOS* **6**, 86–92 (2002).

- [Dre92] A. W. Dreher, K. Reiter, and R. N. Weinreb, "Spatially resolved birefringence of the retinal nerve fiber layer assessed with a retinal laser ellipsometer," *Appl Opt* **31**, 3730-3735 (1992).
- [Dre92(2)] A. W. Dreher and K. Reiter, "Scanning laser polarimetry of the retinal nerve fiber layer," *Proc of SPIE* **1746**, 34-41 (1992).
- [Dre94] A.W. Dreher and K. Reiter, "Retinal eye disease diagnostic system," U.S. Patent No. 5,303,709 (1994).
- [Eib00] M. Eibschitz-Tsimhoni, T. Friedman, J. Naor, N. Eibschitz, and Z. Friedman, "Early screening for amblyogenic risk factors lowers the prevalence and severity of amblyopia," *J APPOS* **4**, 194-199 (2000).
- [Els96] A. E. Elsner, S. A. Burns, J. J. Weiter, and F. C. Delori, "Infrared imaging of sub-retinal structures in the human ocular fundus," *Vision* **36**(1), 191-205 (1996).
- [Fer05] E. J. Fernandez, A. Unterhuber, P. M. Pierto, B. Hermann, W. Drexler, and P. Artal, "Ocular aberrations as a function of wavelength in the near infrared measured with a femtosecond laser," *Opt Express* **13**, 400-409 (2005).
- [Gol92] D. H. Goldstein, "Mueller matrix dual-rotating retarder polarimeter," *Appl Opt* **31**(31), 6676-6683 (1992).
- [Gra06] B. I. Gramatikov, O. H. Y. Zalloum, Y. K. Wu, D. G. Hunter, and D. L. Guyton, "Birefringence-based eye fixation monitor with no moving parts," *J Biomed Opt* **11**(3), 034025-1-11 (2006).
- [Guy00] D. L. Guyton, D. G. Hunter, S. N. Patel, J. C. Sandruck, and R. L. Fry, "Eye fixation monitor and tracker," U.S. Patent No. 6,027,216 (2000).
- [Hau75] P. S. Hauge and F. H. Dill, "A rotating-compensator Fourier ellipsometer," *Optics Communications* **14**(4), 431-437 (1975).
- [Hec02] E. Hecht, *Optics*, 4th ed., Addison Wesley, New York (2002).
- [Hic98] Ian Hickson's Description of the Eye,
<http://academia.hixie.ch/bath/eye/home.html>.
- [Hun99] D. H. Hunter, S. N. Patel, and D. L. Guyton, "Automated detection of foveal fixation by use of retinal birefringence scanning," *Appl Opt* **38**(7), 1273-1279 (1999).

- [Hun99(2)] D. G. Hunter, J. C. Sandruck, S. Sau, S. N. Patel, and D. L. Guyton, "Mathematical modeling of retinal birefringence scanning," *J Opt Soc Am A* **16**(9), 2103–2111 (1999).
- [Hun04] D. G. Hunter, K. J. Nusz, N. K. Gandhi, I. H. Quraishi, B. I. Gramatikov, and D. L. Guyton, "Automated detection of ocular focus," *J Biomed Opt* **9**(5), 1103–1109 (2004).
- [Hun04(2)] D. G. Hunter, D. S. Nassif, N. V. Piskun, R. Winsor, B. I. Gramatikov, and D. L. Guyton, "The Pediatric Vision Screener I: Instrument design and operation," *J Biomed Opt* **9**(6), 1363–1368 (2004).
- [Irs07] K. Irsch, "Minimizing Interference from Corneal Birefringence in Retinal Birefringence Scanning for Biometric Purposes," Diploma Thesis, University of Heidelberg (2007).
- [Jer54] H. G. Jerrard, "Transmission of light through birefringent and optically active media: the Poincaré sphere," *J Opt Soc Am* **44**, 634–640 (1954).
- [Kar93] M. Karbassi, P. C. Magnante, J. K. Wolfe, and L. T. Chylack, "Objective line spread function measurements, Snellen acuity, and LOCS II classification in patients with cataract," *Optom Vision Sci* **70**, 965–962 (1993).
- [Ken00] R. A. Kennedy and D. E. Thomas, "Evaluation of the iScreen digital screening system for amblyogenic factors," *Can J Ophthalmol* **35**, 258–262 (2002).
- [kle88] H. B. Klein Brink and G. J. van Blokland, "Birefringence of the human fovea area assessed in vivo with Mueller matrix ellipsometry," *J Opt Soc Am A* **5**, 49–57 (1988).
- [kle91] H. B. Klein Brink, "Birefringence of the human crystalline lens in vivo," *J Opt Soc Am A* **8**, 1788–1793 (1991).
- [Kna94] R. B. Knapp, L. E. Hake, and H. S. Lusted, "Method and apparatus for eye tracking for convergence and strabismus measurement," U.S. Patent No. 5,293,187 (1994).
- [Kni89] W. R. Knighton, S. C. Jacobson, and M. K. Kemp, "The spectral reflectance of the nerve fiber layer of the macaque retina," *Invest Ophthalmol Vis Sci* **30**, 2393–2402 (1989).

- [Kni02] R. W. Knighton and X. R. Huang, "Linear birefringence of the central human cornea," *Invest Ophthalmol Vis Sci* **43**(1), 82–86 (2002).
- [Kni02(2)] R. W. Knighton and X. R. Huang, "Analytical methods for scanning laser polarimetry," *Optics Express* **90**, 1179–1189 (2002).
- [Köh73] L. Köhler and G. Stigmar, "Vision screening of four-year-old children," *Acta Paediatr Scand* **62**(1), 17–27 (1973).
- [Kur07] S. Kurihara, "Noise removal using 180-degree or 360 degree phase shifting circuit," U.S. Patent No. 7,266,062 B2 (2007).
- [Kva01] G. Kvarnstrom, P. Jakobsson, and G. Lennerstrand, "Visual screening of Swedish children: an ophthalmological evaluation," *Acta Ophthalmol Scand* **79**(3), 240–244 (2001).
- [Lop97] N. Lopez-Gil and P. Artal, "Comparison of double-pass estimates of the retinal-image quality obtained with green and near-infrared light," *J Opt Soc Am A* **14**(5), 961–971 (1997).
- [Mau57] D. M. Maurice, "The structure and transparency of the corneal stroma," *J Physiol (London)* **136**, 263–285 (1957).
- [McC82] R. L. McCally and R. A. Farrell, "Structural implications of small-angle light scattering from cornea," *Exp Eye Res* **34**, 99–113 (1982).
- [McC90] R. L. McCally and R. A. Farrell, "Light scattering from cornea and corneal transparency," in *Noninvasive diagnostic techniques in ophthalmology* (ed B. R. Master), Springer-Verlag, New York, 180–210 (1990).
- [Mea05] Meadowlark Optics Catalog, <http://www.meadowlark.com>.
- [Mor04] C. H. Morimoto and M. R. M. Mimica, "Eye gaze tracking techniques for interactive applications," *Computer Vision and Image Understanding* **98**, 4–24 (2005).
- [Mül00] I. Müller-Voigt, "Hochpräzise drei-dimensionale Bestimmung optischer und biomechanischer Eigenschaften der menschlichen Hornhaut," Ph.D Thesis, University of Heidelberg (2000).
- [Nas04] D. S. Nassif, N. V. Piskun, B. I. Gramatikov, D. L. Guyton, and D. G. Hunter, "The Pediatric Vision Screener II: Pilot study in adults," *J Biomed Opt* **9**(6), 1369–1374 (2004).

- [Nas07] D. S. Nassif, N. V. Piskun, D. G. Hunter, "The Pediatric Vision Screener III: Detection of Strabismus in Children," *Arch Ophthalmol* **124**, 509–513 (2006).
- [Ott95] W. L. Ottar, W. E. Scott, and S. I. Hogada, "Photoscreening for amblyogenic factors," *J Pediatr Ophthalmol Strabismus* **32**, 289–295 (1995).
- [Pat95] S. N. Patel, "Analysis of foveal birefringence to monitor eye fixation," Master's Thesis, Johns Hopkins University, Baltimore, MD (1995).
- [Pel96] B. C. E. Pelz, C. Weschenmoser, S. Goelz, J. P. Fischer, R. O. W. Burk, and J. F. Bille, "In vivo measurement of the retinal birefringence with regard on corneal effects using an electro-optical ellipsometer," *Proc of SPIE* **2930**, 92–101 (1996).
- [Pfe06] W. Pfeifer, "Screening methods for the detection of preclinical vision loss in children in the community: Technology at work," *Am Orthop J* **56**, 22–25 (2006).
- [Pos66] D. Post and J. E. Gurland, "Birefringence of the cat cornea," *Exp Eye Res* **5**, 186–295 (1966).
- [Reu06] N. J. Reus, Q. Zhou, and H. G. Lemij, "Enhanced Imaging Algorithm for Scanning Laser Polarimetry with Variable Corneal Compensation," *Invest Ophthalmol Vis Sci* **47**(9), 3870–3877 (2006).
- [Rob63] D. A. Robinson, "A method of measuring eye movement using a scleral search coil in a magnetic field," *IEEE Trans Biomed Electron* **10**(4) 137–145 (1963).
- [Rog08] D. L. Rogers, D. E. Neely, J. B. Chapman, D. A. Plager, D. T. Sprunger, N. S. Sondhi, G. J. Roberts, and S. Ofner, "Comparison of the MTI Photoscreener and the Welch-Allyn SureSightTM autorefractor in a tertiary care center," *J AAPOS* **12**, 77–82 (2008).
- [Sch02] T. Schimitzek and W. Haase, "Efficiency of a video-autorefractometer used as a screening device for amblyogenic factors," *Graefe's Arch Clin Exp Ophthalmol* **240**, 710–716 (2002).
- [Sch04] P. Schmidt, M. Maguire, V. Dobson, G. Quinn, E. Ciner, L. Cyert, M. T. Kulp, B. Moore, D. Orel-Bixler, M. Redford, and G. S. Ying; Vision in Preschoolers Study Group, "Comparison of preschool vision screening tests

- as administered by licensed eye care professionals in the Vision in Preschoolers Study,” *Ophthalmology* **111**, 637–650 (2004).
- [Sch05] Vision in Preschoolers (VIP) Study Group, “Preschool vision screening tests administered by nurse screeners compared with lay screeners in the vision in preschoolers study,” *Invest Ophthalmol Vis Sci* **46**(8), 2639–2648 (2005).
- [Sco04] S. Scott and H. Yuh, “Proper treatment of effect of mirrors,” MSE Memo #20c (2004).
- [Shu62] W.A. Shurcliff, *Polarized Light: Production and Use*, Harvard University Press, Cambridge, MA (1962).
- [Sim96] K. Simons, “Preschool vision screening: rationale, methodology and outcome,” *Surv Ophthalmol* **41**(1), 3–30 (1996).
- [Sjö90] J. Sjöstrand and M. Abrahamsson, “Risk factors in amblyopia,” *Eye* **4**, 787–793 (1990).
- [Sli80] D. Sliney and M. Wolbarsht, *Safety with Lasers and Other Optical Sources*, Plenum Press, New York (1980).
- [Sne89] R. S. Snell and M.A. Lemp, *Clinical Anatomy of the Eye*, Blackwell Scientific Publications, Inc., Boston, 169–175 (1989).
- [Stan50] A. Stanworth and E. J. Naylor, “Polarization optics of the isolated cornea,” *Br J Ophthalmol* **34**, 1413–1421 (1981).
- [Stan53] A. Stanworth and E. J. Naylor, “Polarized light studies of the cornea,” *J Exp Biol* **30**, 160–169 (1953).
- [The04] The Vision in Preschoolers Study Group, “Comparison of Preschool Vision Screening Tests as Administered by Licensed Eye Care Professionals in the Vision in Preschoolers Study,” *Ophthalmology* **111**, 637–650 (2004).
- [Val61] G. Valentin, “Die Untersuchung der Pflanzen- und der Tiergewebe in polarisiertem Lichte,” Engelmann, Leipzig (1861).
- [van87] G. J. van Blokland and S. C. Verhelst, “Corneal polarization in the living human eye explained with a biaxial model,” *J Opt Soc Am A* **4**, 82–90 (1987).
- [Wea79] R. A. Weale, “Sex, age and birefringence of the birefringence of the human crystalline lens,” *Exp Eye Res* **29**, 449–461 (1979).

- [Wei90] R. Weinreb, A. Dreher, A. Coleman, H. Quigley, B. Shaw, and K. Reiter, "Histopatologic validation of Fourier-ellipsometry measurements of retinal nerve fiber layer thickness," *Arch Ophthalmol* **108**, 557-60 (1990).
- [Wei95] R. N. Weinreb, S. Shakiba, and L. Zangwill, "Scanning laser polarimetry to measure the nerve fiber layer of normal and glaucomatous eyes," *Am J Ophthalmol* **119**, 626–636 (1995).
- [Wei02] R. N. Weinreb, C. Bowd, D. S. Greenfield, and L. M. Zangwill, "Measurement of the magnitude and axis of corneal polarization with scanning laser polarimetry," *Arch Ophthalmol* **120**, 901–906 (2002).
- [Wes94] G. Westheimer and J. Liang, "Evaluating diffusion of light in the eye by objective means," *Invest Ophthalmol Visual Sci* **35**, 2652–2657 (1994).
- [Wie12] O. Wiener, "Die Theorie des Mischkorpers für das Feld der Stationären Strömung," *Abh. Sachs. Ges. Akad. Wiss. Math. Phys. Kl. No. 6* **32**, 507-604 (1912).
- [Wil99] P. A. Williams, "Rotating-wave-plate Stokes polarimeter for differential group delay measurements of polarization-model dispersion," *Appl Opt* **38**(31), 6508–6515 (1999).
- [Wil02] C. Williams, K. Northstone, R. A. Harrad, J. M. Sparrow, and I. Harvey, "Amblyopia treatment outcomes after screening before or at age 3 years: follow-up from a randomized trial," *BMJ* **324**, 1549–1551 (2002).
- [You75] L. R. Young and D. Sheena, "Survey of eye movement recording methods," *Behav Res Methods Instrum* **7**(5), 397–429 (1975).
- [Zag02] N. P. Zagers, J. van de Kraats, T. T. Berendschot, and D. van Norren, "Simultaneous measurement of foveal spectral reflectance and cone photoreceptor directionality," *Appl Opt* **41**(22), 4686–4696 (2002).
- [Zho02] Q. Zhou and R. N. Weinreb, "Individualized compensation of anterior segment birefringence during scanning laser polarimetry," *Invest Ophthalmol Sci* **43**, 2221–2228 (2002).
- [Zho02(2)] Q. Zhou, "System and method for determining birefringence of anterior segment of the patient's eye," U.S. Patent No. 6,356,036 (2002).
- [Zho06] Q. Zhou, "Retinal scanning laser polarimetry and methods to compensate for corneal birefringence," *Bull Soc Belge Ophthalmol* **302**, 89–106 (2006).

Publications

Peer-reviewed articles

- M. Agopov, B. I. Gramatikov, Y. -K. Wu, K. Irsch, and D. L. Guyton, “Use of retinal nerve fiber layer birefringence as an addition to absorption in retinal scanning for biometric purposes,” *Appl Opt* **47**(8), 1048–1053 (2008).
- N. A. Ramey, H. S. Ying, K. Irsch, M. C. Müllenbroich, R. Vaswani, and D. L. Guyton, “A Novel Haploscopic Viewing Apparatus with a Three-Axis Eye Tracker,” *J AAPOS* **12**(5), 498–503 (2008).
- K. Irsch, N. A. Ramey, A. Kurz, D. L. Guyton, and H. S. Ying, “Video-Based Head Movement Compensation for Novel Haploscopic Eye Tracking Apparatus,” *Invest Ophthalmol Vis Sci* (in press).

Conference proceedings

- K. Irsch, B. I. Gramatikov, Y. -K. Wu, and D. L. Guyton, “Spinning wave plate design for retinal birefringence scanning,” *Proc of SPIE* (in preparation).

Abstracts

- H. S. Ying, N. A. Ramey, M. C. Müllenbroich, K. Irsch, and D. L. Guyton, “Basic Cyclovertical Deviation and Superior Oblique Palsy Have Similar Head Tilt Behavior,” Annual Meeting of the American Academy of Ophthalmology, Las Vegas, NV, E-Abstract P0624 (2006).
- R. S. Adyanthaya, H. S. Ying, N. A. Ramey, M. C. Müllenbroich, K. Irsch, and D. L. Guyton, “A Novel Haploscopic Viewing Apparatus with a Three-Axis Eye Tracker,” *Invest Ophthalmol Vis Sci* **48**: ARVO E-Abstract 897 (2007).

- H. S. Ying, K. Irsch, R. Vaswani, A. Kurz, N. A. Ramey, R. S. Adyanthaya, D. S. Zee, and D. L. Guyton, "Ocular Counter-Roll Is Decreased After Vertical Vergence Adaptation," XXV Bárány Society Meeting, Kyoto, Japan (2008).
- H. S. Ying, K. Irsch, R. Vaswani, A. Kurz, N. A. Ramey, R. S. Adyanthaya, D. S. Zee, and D. L. Guyton, "Ocular Counter-Roll Is Decreased After Vertical Vergence Adaptation," *Invest Ophthalmol Vis Sci* **49**, ARVO E-Abstract 1802 (2008).
- K. Irsch, H. S. Ying, A. Kurz, N. A. Ramey, R. S. Adyanthaya, and D. L. Guyton, "Head Movement Compensation for Novel Haploscopic Eye Tracking Apparatus," *Invest Ophthalmol Vis Sci* **49**, ARVO E-Abstract 1803 (2008).
- K. Irsch, B. I. Gramatikov, Y.-K. Wu, and D. L. Guyton, "Polarization modulation improves retinal birefringence scanning," OSA Vision Meeting, Rochester, NY, (2008).
- K. Irsch, B. I. Gramatikov, Y. -K. Wu, and D. L. Guyton, "Spinning wave plate design for retinal birefringence scanning," SPIE Conference on Advanced Biomedical and Clinical Diagnostic Systems VII, San Jose, CA, 2009 (accepted).

Book chapters

- K. Irsch and D. L. Guyton, "Eye Features & Anatomy," in *Encyclopedia of Biometrics*, Springer, New York (in press).

Acknowledgements

This dissertation would not have been possible without the invaluable help, support, encouragement, and inspiration of many individuals. My deepest gratitude goes to my teachers, Prof. Dr. Josef Bille and Prof. Dr. David Guyton, to whom this thesis is partly dedicated. I could not have asked for better role models, and I consider myself truly fortunate to have worked with such brilliant and innovative minds.

I would like to thank Prof. Dr. Josef Bille for introducing me to the interesting field of ophthalmic optics. He has had a remarkable influence on my career as a physicist. His teachings have been an inspiration and have helped to broaden my knowledge and to focus my interest. I am particularly thankful to him for giving me the opportunity and freedom to conduct independent research at Johns Hopkins. This cooperation would not have been possible without his help. I am most grateful for his continuous support and the confidence he has shown me.

I would like to express my sincere gratitude to Prof. Dr. David Guyton, who has served as my primary supervisor at the Wilmer Ophthalmological Institute, The Johns Hopkins University School of Medicine. I could not have imagined having a better advisor and mentor, and it is extremely difficult to overstate my appreciation to him. I am especially grateful for his friendly and professional guidance throughout the past years, despite his countless other responsibilities. His example of hard work, dedication and generosity is an inspiration that has helped me focus my interests and accomplish my goals.

I would also like to thank Prof. Dr. Christoph Cremer for his willingness to take on the task of second referee of my dissertation.

Furthermore, I am indebted to Dr. Boris Gramatikov, without whose skills and vast knowledge in the field of electronics as well as signal acquisition and processing this work could not have been realized. I am especially grateful for his critical insights and interesting discussions, both those given in English and in German at different stages, that have helped to improve my research.

I want to thank my former and current lab mates, Nicholas Ramey and Yi-Kai Wu, for providing a fun environment, and for the unforgettable time inside and outside the lab. I also want to thank the masters students who have joined the lab, especially for their numerous questions that sharpened my ability to explain and increase my own understanding.

Several other people at the Wilmer Institute deserve appreciation, because of whom my experience at Johns Hopkins has been one that I will cherish forever. Special thanks are due to Dr. Howard Ying, Dr. Cameron Parsa, Dr. Kurt Simons, Diane Almony and Barbara Hendrix.

I am grateful to all my friends, some of whom I met while I was at Hopkins and others I have known longer, for their understanding, endless patience and support. Special thanks go to Rania Dahabreh, Rohit Adyanthaya, and Kathrin Bauer.

I cannot end without thanking my entire family for providing a loving environment for me, wherever they are. I could never thank my family enough for everything that they have done for me, especially my parents and grandparents. None of this would have been possible without their love, understanding and encouragement throughout the years. I am most indebted to my parents, Ute and Wilhelm Irsch, for their complete unselfishness and tremendous support that they have always given me in everything that I do. It is to them that I dedicate this thesis.

